

**DESIGN AND FABRICATION OF COPPER-FILLED
PHOTONIC CRYSTAL FIBER FOR PASSIVE OPTICAL
DEVICES**

MOHD FAHMI BIN AZMAN

**FACULTY OF ENGINEERING
UNIVERSITY OF MALAYA
KUALA LUMPUR**

2019

**DESIGN AND FABRICATION OF COPPER-FILLED
PHOTONIC CRYSTAL FIBER FOR PASSIVE OPTICAL
DEVICES**

MOHD FAHMI BIN AZMAN

**THESIS SUBMITTED IN FULFILMENT OF THE
REQUIREMENTS FOR THE DEGREE OF DOCTOR OF
PHILOSOPHY**

**FACULTY OF ENGINEERING
UNIVERSITY OF MALAYA
KUALA LUMPUR**

2019

UNIVERSITY OF MALAYA
ORIGINAL LITERARY WORK DECLARATION

Name of Candidate: **Mohd Fahmi Bin Azman** _____

Matric No: **KHA130137**

Name of Degree: **Doctor of Philosophy**

Title of ~~Project Paper/Research Report/Dissertation/Thesis~~ (“this Work”):

Design and Fabrication of Copper-Filled Photonic Crystal Fiber for Passive Optical Devices

Field of Study: **Photonics**

I do solemnly and sincerely declare that:

- (1) I am the sole author/writer of this Work;
- (2) This Work is original;
- (3) any use of any work in which copyright exists was done by way of fair dealing and for permitted purposes and any excerpt or extract from, or reference to or reproduction of any copyright work has been disclosed expressly and sufficiently and the title of the Work and its authorship have been acknowledged in this Work;
- (4) I do not have any actual knowledge nor do I ought reasonably to know that the making of this work constitutes an infringement of any copyright work;
- (5) I hereby assign all and every rights in the copyright to this Work to the University of Malaya (“UM”), who henceforth shall be owner of the copyright in this Work and that any reproduction or use in any form or by any means whatsoever is prohibited without the written consent of UM having been first had and obtained;
- (6) I am fully aware that if in the course of making this Work I have infringed any copyright whether intentionally or otherwise, I may be subject to legal action or any other action as may be determined by UM.

Candidate’s Signature

Date: 10 MAY 2019

Subscribed and solemnly declared before,

Witness’s Signature

Date: 10 MAY 2019

Name:

Designation:

DESIGN AND FABRICATION OF COPPER-FILLED PHOTONIC CRYSTAL FIBER FOR PASSIVE OPTICAL DEVICES

ABSTRACT

Sub-wavelength electromagnetic waves generated and confined along a metal-dielectric interface via polarized light excitation – also referred to as surface plasmon offers a unique possibility of guiding properties. In this thesis, the copper-filled photonic crystal fiber (PCF) as a new type of plasmonic waveguide is introduced. The holey structure of the photonic crystal fiber is exploited by incorporating a copper microwires into one of the air holes of the PCF. Initially, a technique to fabricate copper encapsulated by silica is developed. By adopting the fiber drawing method, we combine the traditional Taylor wire process to fabricate such structure. We chose Taylor wire process because it is one of the most practical ways and the suitability of the facility that we have. This technique provides a desired copper-in-glass structure with excellent controls over the aspect ratio, diameter, and length. We successfully fabricated a copper-core optical fiber that extends for 100's of meters while remaining up to 6 meters long electrically continuous the longest metal in glass-based fiber reported so far. This technique ensures high repeatability and mass-productions of ultra-long metal in glass, and opens the possibility of nano-sized copper wires resulting in plasmon based applications.

Metallic PCF has many applications in the field of optics communications, especially in passive optical device. Thus, by employing the copper-cane format, we could produce a copper-filled PCF. A traditional approach of stack-and-draw method is used to fabricate copper-filled PCF. We designed a single copper wire which was placed next to the PCF core. The light propagated in the fiber core eventually couple to the SPPs mode, generated by the copper at the phase matching wavelength, also known as resonant condition. The results suggested a high loss occurred at the phase matching condition. The coupled mode

theory was numerically analyzed to investigate the dispersion properties and loss of the proposed structured. It was found that the fabricated copper-filled PCF showing the good properties as a polarization filter with high attenuation, a narrow full-half width maximum (FWHM), high crosstalk and significant bandwidth. Taken together, the PCF polarization filter can also work in the communication wavelength of 1.31 μm and 1.55 μm when the diameter of the copper is altered. This study enables the realization of wavelength-dependent polarization filter.

Next, we also proposed a polarization splitter based on copper-filled dual core photonic crystal fiber. The copper wire is placed between the PCFs cores. We numerically analyze the proposed dual-core structure with commercially available software, COMSOL Multiphysics. Copper wire will increase the birefringence of the PCF structure thus would result in shorter coupling length between both cores. Short coupling length is one of the key parameter as a good splitter. The coupling length for the proposed structure is 1196 μm with coupling ratio of 2 which could operate at 1.55 μm , the communication band. Plus, the extinction ratio for the copper-filled dual-core PCF is considerably low at 1.55 μm with -40 dB. The bandwidth achieved with extinction ratio lower than -20 dB is 88 nm – realizing a broadband and single splitting device which operates at 1.55 μm .

Keywords: Fiber design, Photonic crystal fiber, Microstructure fabrication, Passive optical devices.

REKABENTUK DAN FABRIKASI GENTIAN FOTONIK KRISTAL DIISI

KUPRUM UNTUK PERANTI OPTIK PASIF

ABSTRAK

Sub-gelombang pada gelombang elektromagnet dijana dan dibatasi di sepanjang logam-dielektrik antara muka melalui pengujaan cahaya terkutub - juga dirujuk sebagai plasmon permukaan yang menawarkan kemungkinan ciri panduan yang unik. Dalam tesis ini, kami memperkenalkan gentian fotonik kristal (GFK) yang diisi kuprum sebagai sejenis panduan gelombang plasmonik yang baru. Struktur saluran berongga di dalam gentian fotonik kristal dieksploitasi untuk mengintegrasikan wayar kuprum mikro ke dalam salah satu rongga pada klad gentian tersebut. Pada permulaanya, satu teknik untuk memfabrikasi kuprum yang disampulkan oleh silika dibangunkan. Dengan mengadaptasikan kaedah penghasilan gentian, kami menggabungkan proses penghasilan secara tradisional ‘Taylor wire’ untuk memfabrikasikan struktur tersebut. Kami telah memilih proses ‘Taylor wire’ kerana ia adalah salah satu cara yang paling praktikal dan memenuhi kesesuaian kemudahan yang kami miliki. Teknik ini menyediakan struktur kuprum-dalam-kaca yang dikehendaki dengan kawalan yang sangat baik terhadap aspek nisbah, diameter, dan panjang. Kami telah berjaya menghasilkan gentian optik berteraskan kuprum yang mencapai sehingga 100 meter dengan mengekalkan sehingga 6 meter panjang elektrik secara berterusan - logam terpanjang dalam gentian berasaskan kaca yang dilaporkan setakat ini. Teknik ini memastikan kebolehulangan tinggi dan pengeluaran secara besar-besaran logam yang ultra-panjang, dan mampu membuka kemungkinan wayar kuprum berukuran nano yang menyumbang ke arah aplikasi yang berasaskan plasmon. Metalik gentian fotonik kristal mempunyai banyak aplikasi dalam bidang komunikasi optik terutamanya dalam peranti optik pasif. Oleh itu, dengan menggunakan format kuprum ‘cane’, kita mampu menghasilkan gentian fotonik kristal yang diisi logam kuprum. Kaedah pendekatan tradisional ‘stack-and-draw’ digunakan

untuk memfabrikasi PCF yang diisi logam kuprum. Kami merancang wayar kuprum tunggal yang diletakkan bersebelahan dengan teras GFK. Cahaya yang dibawa di dalam teras gentian akhirnya akan dipasangkan ke mod SPP dari logam kuprum pada fasa pasangan panjang gelombang yang sepadan. Hasilnya mendedahkan bahawa pada pasangan panjang gelombang tertentu, atenuasi yang sangat tinggi akan berlaku. Teori mod pasangan dikaji secara numerikal untuk menyiasat sifat penyebaran dan atenuasi ke atas struktur cadangan tersebut. Telah didapati bahawa PCF yang diisi kuprum menunjukkan ciri-ciri yang baik sebagai penapis polarisasi seperti atenuasi yang tinggi, lebar separuh penuh (FWHM) yang kecil, ketinggian 'crosstalk' dan jalur lebar yang signifikan. Digabungkan bersama, penapis polarisasi PCF juga boleh berfungsi pada panjang gelombang komunikasi pada 1.31 μm dan 1.55 μm apabila diameter kuprum diubah. Kajian ini boleh merealisasikan penapis polarisasi bergantung kepada panjang gelombang. Seterusnya, kami juga mencadangkan pembahagi polarisasi berdasarkan gentian fotonik kristal yang diisi kuprum. Wayar kuprum diletakkan di antara teras GFK. Kami menganalisis secara numerik cadangan yang direkabentuk oleh perisian yang tersedia secara komersial, COMSOL Multiphysics. Wayar kuprum akan meningkatkan 'birefringence' struktur GFK dengan itu akan memendekkan panjang gandingan antara dwi-teras. Panjang gandingan yang pendek adalah salah satu parameter utama sebagai pembahagi yang baik. Panjang gandingan untuk struktur yang dicadangkan ialah 1196 μm dengan nisbah gandingan 2 yang boleh beroperasi pada 1.55 μm , jalur komunikasi. Tambahan pula, nisbah kepunahan untuk GFK dwi-teras yang dipenuhi kuprum agak rendah pada 1.55 μm dengan -40 dB. Jalur lebar dicapai dengan nisbah kepunahan yang lebih rendah daripada -20 dB ialah 88 nm - merealisasikan peranti pemisah yang luas dan tunggal yang beroperasi pada 1.55 μm .

Kata kunci: Rekabentuk gentian, Gentian fotonik kristal, Fabrikasi Mikrostruktur, Alatan optik pasif

ACKNOWLEDGEMENTS

I would like to express my deepest gratitude particularly to my supervisor, Prof. Dr. Faisal Rafiq Mahamd Adikan and Dr. Ghafour Amouzad Mahdiraji for his continuous guidance, advice, understanding, and support during my PhD. Working at the Integrated Research Group has been tremendous and I have learned a lot.

I am extremely grateful to Dr. Wong Wei Ru for her support, and knowledge. Also to my members of the group – past and present – Dr. Ng Wee Lit, Poh Soo Yong, Zahra, Dr. Katrina and Rifat, who have taught me so much, and for their assistance.

Big thanks to my mother, Umi Kalthum Binti Ibrahim, for her part in shaping me to be the person I am today, and for her perpetual prayer. Also to my siblings, and family who consistently supporting me.

Finally, my gratitude goes to my sponsors, Ministry of Higher Education, Government of Malaysia, and the University of Malaya (UM), particularly to Madam Meena who has been helpful in ensuring that everything is in order.

TABLE OF CONTENTS

Design and Fabrication Of Copper-Filled Photonic Crystal Fiber For Passive Optical Devices.....	iii
Rekabentuk dan Fabrikasi Gentian Fotonik Kristal Diisi Kuprum Untuk Peranti Optik Pasif.....	v
Acknowledgements.....	vii
Table of Contents.....	viii
List of Figures.....	xi
List of Tables.....	xv
List of Symbols and Abbreviations.....	xvi
CHAPTER 1: INTRODUCTION.....	1
1.1 Introduction.....	1
1.2 Problem Statements.....	4
1.3 Research Objectives.....	5
1.4 Scope of study.....	5
CHAPTER 2: LITERATURE REVIEW.....	8
2.1 Photonic Crystal Fiber.....	8
2.2 Plasmonic in Photonic Crystal Fiber.....	11
2.3 Optical Properties of Metals.....	13
2.4 Maxwell's and Wave's Equations.....	17
2.5 Recent Advances Plasmonic Photonic Crystal Fiber.....	18
2.5.1 Metal-filled PCF Fabrication.....	18
2.5.2 Design and Applications.....	24
2.6 Summary.....	32

CHAPTER 3: COPPER-IN-GLASS FABRICATION METHODS	33
3.1 Introduction.....	33
3.2 Fabrication Facilities	33
3.3 General Fabrication Process	36
3.4 Fabrication of Copper-Core Optical Fiber.....	42
3.5 Result and Discussions	47
3.6 Summary.....	50
CHAPTER 4: COPPER-FILLED PHOTONIC CRYSTAL FIBER FOR POLARIZATION FILTER	52
4.1 Coupling theory of metal-filled PCF.....	52
4.2 Design and Fabrication Process.....	54
4.2.1 Capillaries Fabrication	56
4.2.2 Stacking Copper-Filled PCF's preform.....	57
4.2.3 Drawing Copper-Filled PCF's preform.....	59
4.3 Numerical analysis and characterization of Copper-filled PCF (CFPCF).....	62
4.4 Experimental Setup.....	65
4.5 Results and Discussion	66
4.5.1 Impact of copper-wire diameter, d_c on characteristics of polarization filter.	73
4.6 Summary.....	77
CHAPTER 5: COPPER-FILLED PHOTONIC CRYSTAL FIBER FOR POLARIZATION SPLITTER.....	79
5.1 Polarization Splitter	79
5.2 Numerical Simulation.....	80
5.2.1 Numerical Methods	80

5.2.2	Modelling	82
5.2.2.1	Geometrical Definition.....	82
5.2.2.2	Subdomain Setting	83
5.2.2.3	Boundary Setting.....	85
5.2.2.4	Meshing.....	86
5.2.2.5	Solving	86
5.2.3	Accuracy.....	86
5.3	Structural Design of Copper-Filled Dual Core PCF for a Use of Polarization Splitter.....	89
5.4	Result and Discussion of Copper-Filled Dual Core PCF	92
5.6	Summary.....	101
CHAPTER 6: CONCLUSION AND FUTURE WORKS		102
6.1	Conclusion	102
6.2	Future works	104
	References.....	106
	List of Publications and Papers Presented	117
	List of Appendices: Copyright and permission from journals.....	118
A.1	Figure 1.1	118
A.2	Figure 2.3.....	121
A.3	Figure 2.7.....	122

LIST OF FIGURES

Figure 1.1: Dielectric-metal plasmonic structure extracted from (a) waveguide (Holmgaard et al., 2009), (b) coupler (Z. Chen et al., 2009), (c) plasmonic biosensor (Wong, Krupin, Adikan, & Berini, 2015), (d) plasmonic photovoltaic cell (Atwater & Polman, 2010).....	3
Figure 2.1: The diameter of the core, ρ , the pitch – centre-to-centre separation of the cladding (pitch), Λ and the diameter of the cladding, d	8
Figure 2.2: An illustration of (a) solid core PCF with SEM images, (b) hollow core PCF with their respective cross-sectional SEM images. Both PCF were successfully fabricated by our research group.....	9
Figure 2.3: geometry configurations: (a) Kretschmann geometry, (b) two-layer Kretschmann geometry, (c) Otto geometry, (d) excitation with a SNOM probe, (e) diffraction on a grating, and (f) diffraction on surface features. Image is extracted from (Zayats, Smolyaninov, & Maradudin, 2005)	11
Figure 2.4: Schematic of metal-filled PCF where the light is launched to the core for the excitation of SPP on the metal wire.	12
Figure 2.5: Typical electric response (a) Lorentz model for dielectric (b) Drude model for metals (Equation 2.8,2.9)	15
Figure 2.6: Real and imaginary parts of dielectric constant of copper, silver, and gold corresponding the experimental value from Johnson and Christy (P. B. Johnson & Christy, 1972).....	16
Figure 2.7: (a) Schematic of the rudimentary furnace used by Taylor in the first.....	20
Figure 2.8: Single core PCF with metal-filled located next to PCF's core for polarization filter.....	25
Figure 2.9: Dual-core PCF with metal-filled located between the PCF's cores for polarization splitter.....	29
Figure 3.1: Schematic of Fiber Draw Tower in University of Malaya	34
Figure 3.2: (a) Top-floor elements (b) Ground floor elements	35
Figure 3.3: (a) Preform's drop passing through the bottom iris. (b) Round heat illumination appears from the bottom iris. (c) Cutting at the neck-down of the preform.	36

Figure 3.4: (a) Attaching a small weight to pull the fibers at a constant rate (b) Applying speed after the fiber reached the clamp (c) the clamp (cane pullers) which controls speed (d) laser diameter gauge (e) coating cup.	38
Figure 3.5: (a) Cane pullers (b) Capstan wheel and tension meter (c) Tensioner/Dancers (d) Drum winder.....	39
Figure 3.6: Flow diagrams of the general fabrication process.....	42
Figure 3.7: Copper-core optical fiber fabrication hierarchy, (a) bulk size tube glass with short-length copper-filled and melted inside, (b) copper-core cane fabricated from the preform in (a), and (c) output copper-core optical fiber.	44
Figure 3.8: The longitudinal view of copper-cane showing (a) discontinuity of copper formed in the glass capillary without applying pressure with a copper rod. (b) The perfect continuous copper formed in the glass capillary.....	45
Figure 3.9: Images of cane size, copper-in-glass capillary.....	46
Figure 3.10: (a) Oxygen-butane flame to fuse handle and load (b) an extension of the copper cane.....	46
Figure 3.11: (a) SEM images for copper core optical fiber. The dimension of the fiber with 170 μ m cladding and 22.9 μ m copper core (b) Fabricated copper-core optical fiber with more than 6 m continuous copper-in-glass, the longest reported so far.	47
Figure 3.12: Conductivity and continuity test for copper-core optical fiber.....	47
Figure 3.13: Resistance of each length of copper fiber.....	49
Figure 3.14: The I-V linear graphs for 30 cm, 80 cm, and 110 cm to evaluate the resistance of the sample. Inset is the circuit diagram of conductivity tests.	50
Figure 4.1: 3D-sketch and the cross-section of the design copper-filled PCF.....	55
Figure 4.2: (a) Schematic diagram of cross-section of copper-filled PCF with packing rods. (b) Stacking the capillaries, solid rod and copper-cane. (c) Completed stacking in the hexagonal jig. (d) The complete stacking is transferred into silica tube with packing rods to fill the empty space.	58
Figure 4.3: Fabricated copper-filled PCF cane measuring 1.7 mm diameter.....	59
Figure 4.4: (a) SEM images for fabricated copper-filled PCF fiber. (b) Magnified view of the core area of the PCF indicating the presence of copper and a solid core.....	60
Figure 4.5: An illustration of copper-filled PCF (CFPCF) fabrication process.....	61

Figure 4.6: The extracted SEM image from COMSOL with meshing structure for PML, core, and cladding region.	64
Figure 4.7: (a) Experimental setup to measure transmission spectrum and CCD imaging. (b) Connecting both end facets by metal-soldering for continuity tests.	65
Figure 4.8: (a) SEM image of the fabricated CFPCF, and (b) mode profile image taken from the CCD for x- and y- polarized modes	66
Figure 4.9: Simulated results for (a) dispersion relation of the CFPCF polarization filter. (b) Loss spectrum for CFPCF for x- and y- polarizations. Electric field distribution of the fundamental mode of (c) x-polarization at 1790 nm and (d) y-polarization at 1890 nm.	67
Figure 4.10: Contour line of transverse electric field vector distribution of the (a) x-polarization, (b) y-polarization, representing the coupling strength of the phase matching phenomena.	68
Figure 4.11: Transmission spectra of measurement and FEM simulation: (a) x-polarization, (b) y-polarization.....	69
Figure 4.12: Calculated crosstalk for five different lengths of CFPCF polarization filter	71
Figure 4.13: IL with varying fiber length for (a) x-polarization, (b) y-polarization.....	72
Figure 4.14: Resonance loss for four different sizes of the copper wire (a) x-polarization (b) y-polarization.....	74
Figure 4.15: Resonance wavelength for different diameter of copper wire.....	75
Figure 4.16: Crosstalk for 0.8 mm long CFPCF as a function of wavelength, considering different diameters of copper wire, d_c	76
Figure 5.1: Flow diagram of simulation process.....	82
Figure 5.2: FEM simulation on copper-filled dual-cores PCF: (a) structural design; (b) subdomain definition; (c) setting of the boundary conditions; (d) mesh generation; (e) solution.....	83
Figure 5.3: Effective index dependence on a_{max} for the fundamental mode of the fiber studied in (White et al., 2002), calculated with the FEM (blue); the MM result is shown in red for comparison.	87
Figure 5.4: Effective index dependence on the mesh size for the fundamental mode of the fiber studied in (White et al., 2002) , calculated with FEM (blue); the MM result is shown in red for comparison.	88

Figure 5.5: Structural design for Copper-Filled Dual Core PCF	89
Figure 5.6: SEM images for copper-filled PCF	90
Figure 5.7: The schematic diagrams of design copper-filled PCF with PML	90
Figure 5.8: Electric field distribution for (a) x-even mode, (b) y-even mode, (c), x-odd mode, (d) y-odd mode	91
Figure 5.9: (a) The coupling length of PCF with copper-filled, (b) without copper-filled	94
Figure 5.10: Coupling length comparison of the diameter of copper wire, d_c with respect to lattice-spacing ratio, d/Λ (a) coupling length of x-polarization (b) coupling length of y-polarization at 1.55 μm wavelength.....	95
Figure 5.11: Different lattice-spacing ratio. (a) Larger ratio with larger diameter of air holes, d . (b) Smaller ratio with smaller diameter of air holes, d	96
Figure 5.12: Coupling ratio comparison the diameter of copper wire, d_c with respect to lattice-spacing ratio, d/Λ at 1.55 μm wavelength	97
Figure 5.13: Normalized power transfer in (a) Core A , (b) Core B for the proposed dual-core copper-filled PCF at wavelength 1.55 μm	98
Figure 5.14: Extinction ratio of copper-filled dual-core PCF	99
Figure 6.1: Fabricated D-shaped SMF	104
Figure 6.2: Wire array metamaterial based on copper cane (a), (b) stack copper-cane, (c) Neck-down region for stack copper-array in silica (d) SEM image for copper array cane.	105

LIST OF TABLES

Table 2.1: Different metal wire fabrication techniques	23
Table 2.2: Different PCF design for the polarization filter wavelength-dependent based on metal-filled PCF	27
Table 2.3: Polarization splitters using different types of metal wires.....	31
Table 4.1: Fit parameters for the D2CP model of permittivity for copper	63
Table 4.2: Polarization Characteristics with respect to the Diameter of Copper Wire (d_c)	77
Table 5.1: PML parameters.....	85
Table 5.2: Comparison with existing literature for polarization splitter.....	100

LIST OF SYMBOLS AND ABBREVIATIONS

n_1	:	Higher refractive index
n_2	:	Lower refractive index
θ_i	:	Angle of incidence
θ_r	:	Angle of reflection
θ_t	:	Angle of transmission
$E_{ }$:	Electric field vector parallel to the plane of incidence
E_{\perp}	:	Electric field vector perpendicular to the plane of incidence
P	:	Phase factor of the transmitted wave
k_t	:	Wave vector associated with the transmitted wave
λ_0	:	Wavelength of radiation in vacuum
$F(y)$:	Decay with distance in the second medium
L_0	:	Stretching length
Z	:	Elongation distance
χ	:	Distance from the beginning of the PML
d	:	Air hole diameter/Outer diameter of capillary in DRF preform
Λ	:	Pitch size
d/Λ	:	Lattice spacing ratio
$\text{Im}[n_{eff}]$:	Imaginary part of the effective refractive index
λ	:	Operating wavelength
d_{core}	:	Air hole diameter at the middle of the silica core
\vec{E}	:	Electric field
\vec{H}	:	Magnetic field
\vec{D}	:	Electric flux density

\bar{B}	:	Magnetic flux density
\bar{J}	:	Current density of free charges
ρ	:	Free charge density
ϵ_0	:	Free space's permittivity
μ_0	:	Free space's permeability
c	:	Speed of light in free space
$\epsilon(r)$:	Relative permittivity
$\mu(r)$:	Relative permeability
n	:	Refractive index
ω	:	Angular frequency
β	:	Propagation constant along the z -direction
ω_j	:	Resonant frequencies
ω_p	:	Plasma frequency
τ	:	Average time between successive collisions
γ	:	Damping constant
m	:	Effective mass
e	:	Electron charge
B_j	:	Strength of the resonances
s_x	:	PML parameters
s_y	:	PML parameters
d_i	:	PML width in the horizontal or vertical direction
b	:	PML free-parameter
a_{max}	:	PML free-parameter
α	:	PML free-parameter/Confinement loss

n_{eff}	:	Effective refractive index
$\text{Re}[n_{eff}]$:	Real part of the effective refractive index
A_f	:	Cross-sectional area of preform
A_d	:	Cross-sectional area of capillary
v_f	:	Feeding speed
v_d	:	Drawing speed
L	:	Furnace's hot zone length
n_{silica}	:	Refractive index of silica
ϵ_{Au}	:	Permittivity of the gold material
ϵ_{∞}	:	Permittivity at high frequency
ω_D	:	Plasma frequency
γ_D	:	Damping frequency
$\Delta\epsilon$:	Weighting factor
n_a	:	Refractive index of analyte
CCD	:	Coupled-Charge Device
PCF	:	Photonic Crystal Fiber
SNOM	:	Scanning Near-field Optical Microscopy
SPR	:	Surface Plasmon Resonance
SPP	:	Surface Plasmon Polariton
PBGF	:	Photonic Bandgap Fiber
SMF	:	Single Mode Fiber
MM	:	Multipole Method
PWEM	:	Plane Wave Expansion Method
EME	:	Eigenmode Expansion Method

D2CP	:	Drude Plus Two Critical Point
I-V	:	Current vs. Voltage
kPa	:	Kilo pascal
FEM	:	Finite Element Method
PDE	:	Partial Differential Equation
PML	:	Perfectly Matched Layer
Pb	:	Plumbum
Bi	:	Bismuth
Au	:	Gold/Aurum
Ag	:	Silver/Argentum
Sn	:	Stannum
Fe	:	Ferum
Cu	:	Copper
Ti	:	Titanium
Cd	:	Cadmium
Co	:	Cobalt
Sb	:	Antimony
Ga	:	Gallium
In	:	Indium
HF	:	Hydrofluoric acid
BC	:	Boundary Condition
MUMPS	:	Multifrontal Massively Parallel Sparse Direct Solver
PMMA	:	Polymethylmethacrylate
UM	:	University of Malaya

UV	:	Ultraviolet
PID	:	Proportional Integral Deferential
ID/OD	:	Inner wall over outer wall diameter ratio
SEM	:	Scanning Electron Microscope
CCD	:	Charge Coupled Device
RI	:	Refractive Index
Rh	:	Relative humidity
ER	:	Extinction Ratio

University of Malaya

CHAPTER 1: INTRODUCTION

1.1 Introduction

The study concerning light and matter interactions plays an essential role in many aspects of life. Several optical effects such as scattering, emission, absorption, refraction, and fluorescence may evolve from the interaction of electromagnetic wave (light) with atoms or molecules (material). The novel optical devices and instruments for telecommunication purposes, light source, sensor, and optical interconnection can be created if the interaction between light and matter are precisely controlled.

Optical fiber is an excellent example showing its capability to guide and manipulate light. The fundamental physics principle of total internal reflection for propagating light in a higher refractive index medium in the core which was first presented by the winner of the Nobel Prize for Physics, Charles Kuen Kao in 1966 and further published in July with his former colleague, George Hockham. With very low attenuation loss, the optical fiber could provide high bandwidth optical signal transmission for a long distance communication. The revolution of optical fiber became rapid with the creation of Photonic crystal fiber (PCF) - a modified version of the optical fiber, which provides unique potentials in the investigation of light manipulation in wavelength-scale systems (P. Russell, 2003, 2007; P. S. J. Russell, 2006; Wadsworth, Knight, & Birks, 2012). PCF is a type of optical fiber with two-dimensional periodic structures of hollow channels. Light can be guided through a solid core PCF by a modified total internal reflection and in a hollow core PCF by photonic bandgap effect. Since the born of the first PCF in 1995, its versatility establishes itself through cross-disciplinary applications, owing to its interesting structure with adjustable parameters such as the diameter of the air holes, size of pitch and the materials that can be embedded inside the hollow channels. For example, the supercontinuum generation (J.M. Dudley et al., 2006; T.A. Birks et al., 1996), optical sensing (M.C.P. Huy et al., 2007; D.K.C. Wu et al., 2009), particles guidance (O.A.

Schmidt et al., 2012; M.K. Garbos et al., 2011), (J. Bland-Hawthorn et al., 2011), gas-based nonlinear optics studies (J. Travers et al., 2011; P. Hoelzer et al., 2011), optoacoustic interactions (M.S. Kang et al., 2009), and so on.

The main function of dielectric waveguide is to send light. However, its performance has been mainly limited by diffraction. For instance, the diffraction limit which is defined by $d = \lambda/2n$ for a dielectric medium with the refractive index of n . This implies that light could not be focused into a spot smaller than dimension d and cannot be guided in the optical fiber or waveguide core with the dimension smaller than d . The diffraction limit actively limits the development of photonic devices and impedes the ability to precisely control and manipulate the light-matter interaction in subwavelength scale. Various efforts have been cleared to attain optical waveguide with sub-wavelength scale, and one promising approach arises from the concept of surface plasmon polaritons. The electromagnetic wave can be guided by a metal-dielectric structure below the diffraction limit while providing the high optical bandwidth. The progress in micro and nanofabrication techniques has attracted researcher to fabricate nanoscale metal-insulator construction. Owing to its nature as a surface electromagnetic waves, SPP modes can guide along the interface between metal and dielectric medium with a subwavelength scale confinement far below the diffraction limit of light less than 50 nm (Barnes, Dereux, & Ebbesen, 2003). Hence, the necessities to acquire a smaller proportion of the metal-dielectric optical waveguide is vital to overcoming these restrictions. Plasmonics devices with sub-wavelength confinement and high optical bandwidth can be the solution for future communication systems as it encompasses photonics and electronics.

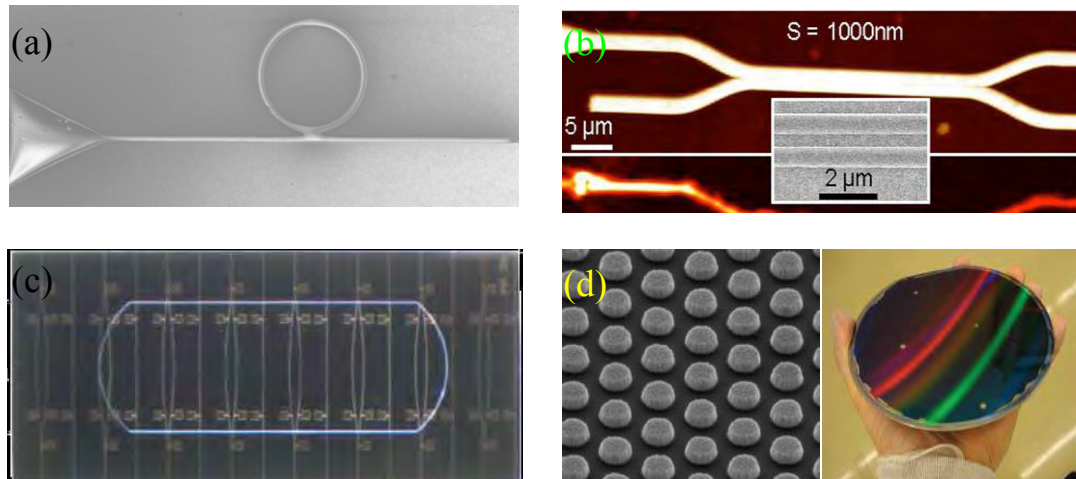


Figure 1.1: Dielectric-metal plasmonic structure extracted from (a) waveguide (Holmgaard et al., 2009), (b) coupler (Z. Chen et al., 2009), (c) plasmonic biosensor (Wong, Krupin, Adikan, & Berini, 2015), (d) plasmonic photovoltaic cell (Atwater & Polman, 2010)

A wide variety of plasmonic structures and devices has been realized such as plasmonic wedge or nanowire waveguide (Bozhevolnyi, Volkov, Devaux, & Ebbesen, 2005; Bozhevolnyi, Volkov, Devaux, Laluet, & Ebbesen, 2006; Charbonneau, Berini, Berolo, & Lisicka-Shrzek, 2000; Ditlbacher et al., 2005) splitters (Figure 1(a)), and couplers (Figure 1(b)), (Delacour et al., 2010; Drezet et al., 2007; Guo et al., 2009; Yan, Pausauskie, Huang, & Yang, 2009), plasmonic biosensors (Figure 1(c)), (Rifat et al., 2015; Wong et al., 2015) (Figure 1(c)), near-field optics and microscopy (N. Liu, Hentschel, Weiss, Alivisatos, & Giessen, 2011; Novotny & van Hulst, 2011) and plasmonic photovoltaic devices (Figure 1(d)), (Atwater & Polman, 2010; Polman & Atwater, 2012)(Figure 1(d)).

1.2 Problem Statements

Sub-wavelength electromagnetic waves generated at a metal-dielectric interface via polarized light excitation – also referred to as surface plasmon – continues to be a subject of intense research, mainly due to their capabilities in high sensitivity sensing applications (Wong, Krupin, Sekaran, Mahamd Adikan, & Berini, 2014; Wong, Sekaran, Adikan, & Berini, 2016). Fabrication of high purity, precise dimensions, and ultra-clean interaction surfaces remains non-trivial, particularly in ensuring high repeatability, low cost and accurate sensing performance. The ability to launch light into a surface plasmon structure without the use of prisms is an added advantage. Also, eliminating the use of free space optics in collecting plasmon chip outputs would lead to miniaturized modules, reducing the barrier to technological adoption. To this end, performing the plasmon process within a fiber structure is attractive as the approach lends to all the above-mentioned advantages. This places the need to fabricate micron, or nano-sized metal wires – only referred to here as nanowires – within an optical fiber structure.

So far, no extensive work has been done on the subject of metal-dielectric fabrication. There are a number of approaches in producing metal-dielectric waveguides involving nanowires, including photolithography or electron-beam lithography (Menke, Thompson, Xiang, Yang, & Penner, 2006), solution based synthesis (Wiley et al., 2006), template-based electrodeposition (Menke et al., 2006), and physical vapor deposition (Huang et al., 2001). Solution-based synthesis, in particular, lends to the fabrication of large quantities of single crystalline smooth surface nanowires. However, the technique, like most others, could not produce long lengths of continuously conductive wires and require multiple processing stages. An approach that adopts processes not too dissimilar from conventional optical fiber fabrication is called Taylor's method (G. Taylor, 1924). The technique involves sealing a metal wire in a glass capillary and pulling the structure into smaller dimensions by applying heat. 260 nm Au (gold) wires were successfully

fabricated via this process as reported in (Tyagi et al., 2010). However, the wires produced are only 20 μm long, and the 'fiber' contained a number of micron-sized gaps between the lengths of nanowires. In (X. Zhang, Wang, Cox, Kuhlmeiy, & Large, 2007), work in pumping molten metal into the hollow channels of a photonic crystal fiber at very high pressure is reported. Metal-core sizes of 120 nm were successfully produced, but are limited to only a few centimeters in length. Fiber drawing is an interesting alternative approach to overcome these problems, since one standard preform can generate kilometers' of fibers. Furthermore, the fiber drawing technique also offers better control on the scaling down to intended fiber size with good structure.

1.3 Research Objectives

This study aims to produce and characterize a metal-dielectric structure based optical fiber by using fiber fabrication based on top-down approach. The fundamental studies of surface plasmon resonance in the fabricated structure will also be investigated. The objectives of our studies are:

- To develop a method for fabricating metal-in-glass based optical fiber.
- To fabricate metal-in-glass structure based optical fiber and photonic crystal fiber (PCFs).
- To investigate the surface plasmon resonance (SPR) characteristics of fabricated metal-filled PCF and its potential applications.

1.4 Scope of study

This work covers fabrication, simulation, and experimental work. Design and development of the proposed structure are numerically simulated with a commercial software called COMSOL. The fabrication work begins by developing the technique to fabricate copper-in-glass. This technique is crucial as to produce copper-core optical fiber and copper-filled photonic crystal fibers (PCF). Investigation of the interaction between the copper-wire in PCF will be thoroughly studied to discuss its properties.

This thesis report is organized into six chapters. A summary of the next six chapters is given in this section.

Chapter 2 gives an overview of relevant fundamental properties and theoretical description of the electromagnetic wave with metal on sub-wavelength scale. The photonic crystal fiber and its unique properties are briefly. The brief introduction of surface plasmon polaritons is then provided. The optical properties of metals are then introduced by discussing the Drude model, Maxwell's and wave equations. The coupled mode theory is introduced to study the interaction between the SPP mode and the core guided mode in a metal-filled PCF. The recent advancement of metal-filled is reviewed.

Chapter 3 outlines the technique to fabricate metal-in-glass capillary. Copper has been used since the optical properties of it is almost similar to a noble metal such as gold. We present the novel method to fabricate consistent and continuous length of metal-in-glass capillary. The comparison between existing techniques and the drawbacks of the current fabrication technique are reviewed. Following this, by successfully fabricating the metal in a glass capillary, copper-filled PCF can be fabricated.

Chapter 4 investigates plasmon excitations and SPP coupling in copper-filled PCF. A copper-microwire is placed parallel and next to the solid core PCF. Surface plasmon resonance was observed at the phase matching wavelength between the core guided mode and SPP mode by measuring the optical transmission. The transmission characteristics including transmission spectrum, the polarization dependence, and the near-field images are presented and compared to the simulation results. One potential application suits this best is polarization wavelength-dependence filtering.

Chapter 5 presents the copper-filled dual-core PCF. The copper wire is placed in between the dual cores. The interaction between both cores with the copper microwire is investigated. The proposed structure will potentially work as a polarization splitter, which

can split incoming two orthogonally polarized light into x- and y- polarized. To date, various structures based on PCF have been developed and introduced to produce the polarization splitter. However, most of the work presented was purely based on numerical study without the attempt to fabricate the structure. The design of polarization splitter based on photonic crystal fiber with a copper nanowire as a core will be introduced. The fabricated polarization splitter is then simulated with COMSOL Multiphysics.

Finally, Chapter 6 concludes the thesis. Several suggestions for future works on the development of the novel devices are given.

University of Malaya

CHAPTER 2: LITERATURE REVIEW

In this chapter, we will discuss the interaction of light or electromagnetic wave with metal on the sub-wavelength scale. In section 2.1, we introduce the photonic crystal fiber and its unique properties. We then provide a brief introduction of surface plasmon polaritons. The optical properties of metal are then introduced in section 2.3 by discussing the Drude model. Section 2.4 discusses the Maxwell's and wave equations. In section 2.5, we briefly explain the recent advancement of metal-filled PCF.

2.1 Photonic Crystal Fiber

In 1997, Philip Russell published the idea of PCFs (Birks, Knight, & Russell, 1997). He suggested the theory of photonic bandgap fiber to allow certain wavelength to trap in a hollow-channel core fiber, by arranging a constant periodic lattice with wavelength-sized of tiny air-holes as cladding. Later in 2003, he and his co-workers created the solid core photonic crystal fiber by modifying the center hole with solid silica as a core (this is called a defect) (P. Russell, 2003). The findings generated a lot of attention in PCFs due to several potential applications in fundamental optics. PCFs are principally specified by three main parameters as shown in Figure 2.1.

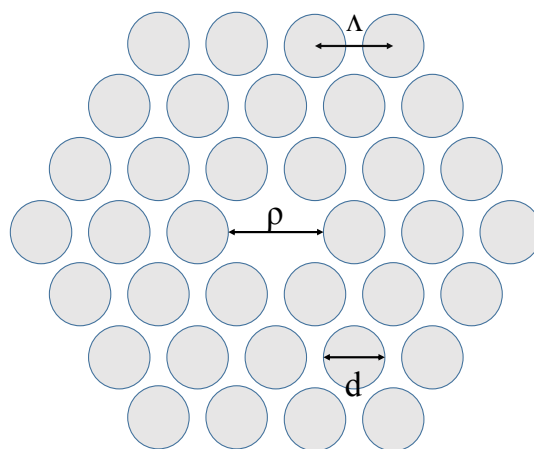


Figure 2.1: The diameter of the core, ρ , the pitch – centre-to-centre separation of the cladding (pitch), Λ and the diameter of the cladding, d .

There are two main types of PCF, index guiding PCF (solid core PCF) and photonic bandgap guiding PCF (hollow core PCF) as depicted in Figure 2.2. As shown in Figure 2.2 (a), in index-guiding PCF, the defect core material is a silica which has a higher refractive index than the microstructure cladding which consists of an array of air. The array of air holes in the cladding provides the guiding mechanism of PCFs significantly dissimilar propagation characteristics from the conventional total internal reflection (TIR) guiding fibers. The core will have a higher refractive index and it will allow light to propagate only in the fiber core. Whereas, the photonic bandgap guiding as shown in Figure 2.2 (b), PCF traps a particular frequency of light in the hollow core by the effect of the photonic bandgap. For this guiding principle, it is not necessarily that the core must have a higher refractive index than the cladding to propagate the light. The periodic structure in the cladding can be made up of air (Knight, Birks, Russell, & Atkin, 1996), and other material with high refractive index (Luan et al., 2004). The microstructure of high-index cladding would cause a photonic bandgap effect which allows a specific wavelength to propagate in the lower-index core region.

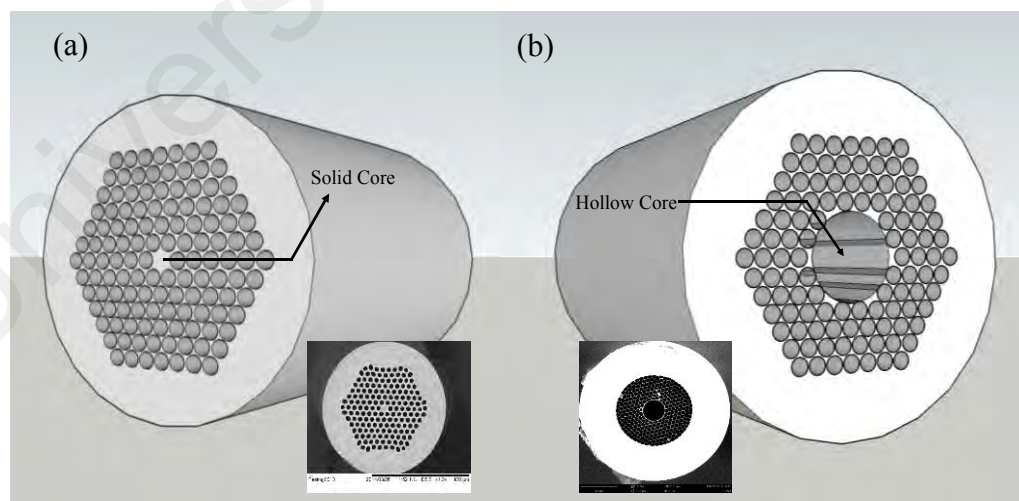


Figure 2.2: An illustration of (a) solid core PCF with SEM images, (b) hollow core PCF with their respective cross-sectional SEM images. Both PCF were successfully fabricated by our research group.

The unique structure of both PCF with the interesting guiding mechanism, make the optical properties more versatile. The manipulation of the PCF structure by incorporating the air-holes cladding with metal (Lee, Schmidt, Tyagi, Sempere, & Russell, 2008), semiconductor (Yablonovitch, 2001), liquid crystal (Du, Lu, & Wu, 2004), is non-trivial but possible. Some interesting properties of PCF include the endlessly single mode fibers (Birks et al., 1997), high birefringence by designing the different symmetry of holes next to the core (Ortigosa-Blanch et al., 2000), hollow-core guiding (Y. Y. Wang, Wheeler, Couny, Roberts, & Benabid, 2011), good nonlinearity effects (Dudley, Genty, & Coen, 2006), and dispersion engineered (Reeves et al., 2003). In this thesis, the solid core PCFs (index-guiding) is mainly used and selectively incorporating copper into the air-holes for surface plasmon excitation.

2.2 Plasmonic in Photonic Crystal Fiber

SPPs are the surface electromagnetic waves guiding along the metal-dielectric interface. The electromagnetic field of the light wave would excite the free electrons in the surface of the metal, and they oscillate (A.D.W.L. Barnes and T.W. Ebbesen 2003). The electromagnetic wave can propagate along a metal-dielectric interface with small dimension structure right under the diffraction limit while still keeping the high optical bandwidth.

Generally, the SPP mode cannot be excited by directly shooting the light on the metal surface due to its momentum mismatch with the light in free space. Thus, the incident light cannot be coupled to the SPPs mode. Figure 2.3 depicts the various coupling techniques are proposed to match the momentum of the incident light and SPPs to excite the SPPs mode such as by using prism couplers (Kretschmann & Raether, 1968; Otto, 1968), excitation with scanning near-field optical microscopy (Hecht, Bielefeldt, Novotny, Inouye, & Pohl, 1996), diffraction grating (Salomon et al., 2002) and so on.

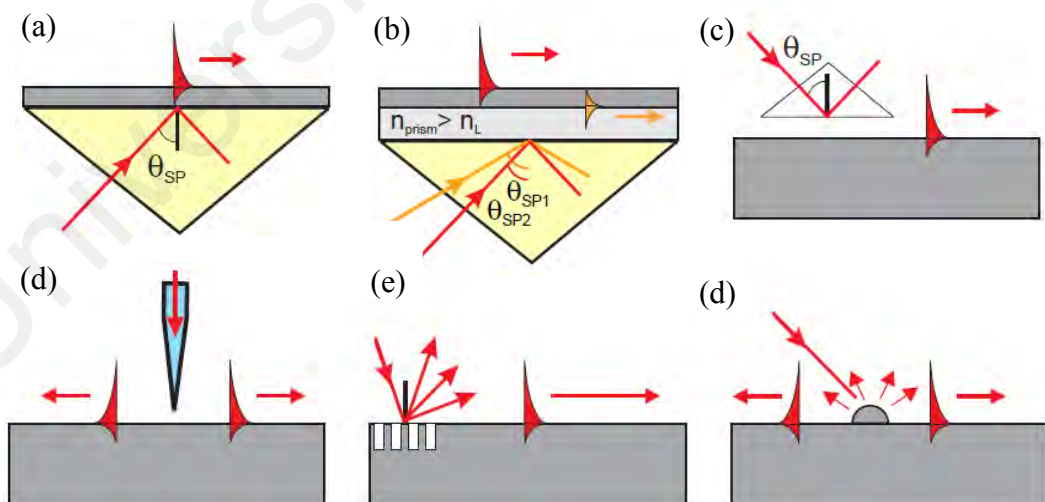


Figure 2.3: geometry configurations: (a) Kretschmann geometry, (b) two-layer Kretschmann geometry, (c) Otto geometry, (d) excitation with a SNOM probe, (e) diffraction on a grating, and (f) diffraction on surface features. Image is extracted from (Zayats, Smolyaninov, & Maradudin, 2005)

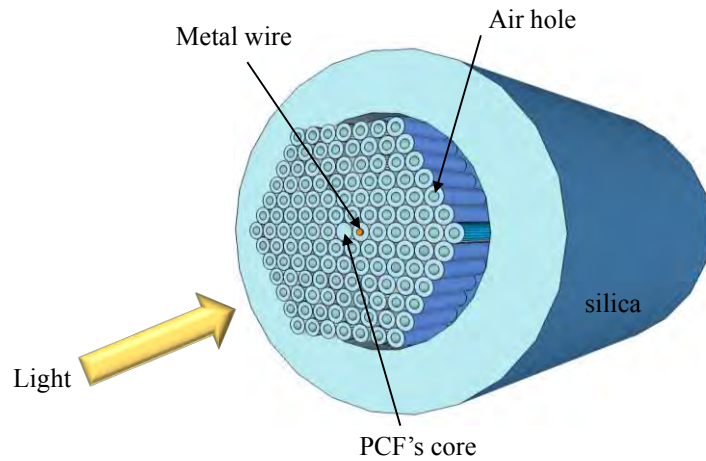


Figure 2.4: Schematic of a metal-filled PCF where the light is launched to the core for the excitation of SPP on the metal wire.

In this study, the SPP mode is excited by an alternative configuration using metal-filled PCF as illustrated in Figure 2.4. As mentioned earlier, by incorporating metal in the hollow channel of PCFs, the transmission characteristics including the dispersion and absorption of the metal-filled PCF can be controlled. The SPP mode will be excited when the light is launched into the fiber core. The SPP resonances are observed when the wave vectors of the core-guided mode and the SPP mode are phase-matched (Lee et al., 2008; M. A. Schmidt, Prill Sempere, Tyagi, Poulton, & Russell, 2008).

The metal-filled PCF provides a novel configuration and approach to excite the SPP mode on a cylindrical metal-dielectric structure. These plasmonic PCFs represent a new type of plasmonic waveguiding which enables the realization of novel in-fiber plasmonic devices such as polarizers or filters, splitters, optical sensors, near-field optics for sub-wavelength scale imaging, and nanoelectrodes.

2.3 Optical Properties of Metals

The optical properties of metal depend on the response of the electron in the conduction band since metal has high electron density on the metal surface¹. The concentrations of free electrons of metal are very high with the order of 10^{28} m^{-3} . The dielectric function and the absorption of light due to the electron transition to higher energy states concerning the conduction band can be described as the free electron theory of metals. The Drude model often describes the electron transport in metals. The response of metal to electromagnetic radiation can be defined as

$$\vec{D} = \epsilon_0 \vec{E} + \vec{P} = \epsilon_0 \epsilon(\omega) \vec{E} \quad (2.1)$$

where \vec{D} is the electric displacement, \vec{E} is the electric field, \vec{P} is the electric polarization, and ϵ_0 and ϵ are vacuum permittivity and the dielectric constant for material, respectively. The electrons oscillate with the applied electromagnetic field in the free electron model. The electrons are damped when it collided with one another, which is characterized by a damping constant $\gamma = 1/\tau$, where τ is the average time between successive collisions.

¹ Most of the material in this section were referenced from the following sources [Mark Fox, 2001]. As such, for a more in-depth treatment of the subject, readers are directed to the said references.

By assuming an oscillating electromagnetic field of

$$\vec{E}(t) = \vec{E}_0 e^{-i\omega t} \quad (2.2)$$

The motion of the electrons can be defined as an oscillation equation of

$$m \frac{\partial^2 \vec{x}}{\partial t^2} + m\gamma \frac{\partial \vec{x}}{\partial t} = -e\vec{E}_0 e^{-i\omega t} \quad (2.3)$$

where m is the effective mass and e is electron charge. By solving the partial differential equation of Equation (2.3), the solution of the following form is:

$$\vec{x}(t) = \frac{e}{m(\omega^2 + i\gamma\omega)} \vec{E}_0 e^{-i\omega t} \quad (2.4)$$

and the polarization \vec{P} is written as:

$$\vec{P} = -Ne\vec{x} = \frac{e^2 N}{m(\omega^2 + i\gamma\omega)} \vec{E}_0 e^{-i\omega t} \quad (2.5)$$

and the electric displacement can be described as:

$$\vec{D} = \varepsilon_0 \left(1 - \frac{e^2 N}{m\varepsilon_0(\omega^2 + i\gamma\omega)} \right) \vec{E}_0 e^{-i\omega t} \quad (2.6)$$

where $\omega_p^2 = \frac{e^2 N}{\varepsilon_0 m}$ is the plasma frequency of the free electron in the gas state. It is the

typical electrostatic oscillation frequency for the electrons to restore their equilibrium

positions. By using equation 2.15 and equation 2.6, the dielectric function can be expressed by:

$$\varepsilon(\omega) = 1 - \frac{\omega_p^2}{\omega^2 + i\gamma\omega} \quad (2.7)$$

with the real and imaginary parts:

$$\varepsilon'(\omega) = 1 - \frac{\omega_p^2 \tau^2}{1 + \omega^2 \tau^2} \quad (2.8)$$

$$\varepsilon''(\omega) = \frac{\omega_p^2 \tau}{\omega(1 + \omega^2 \tau^2)} \quad (2.9)$$

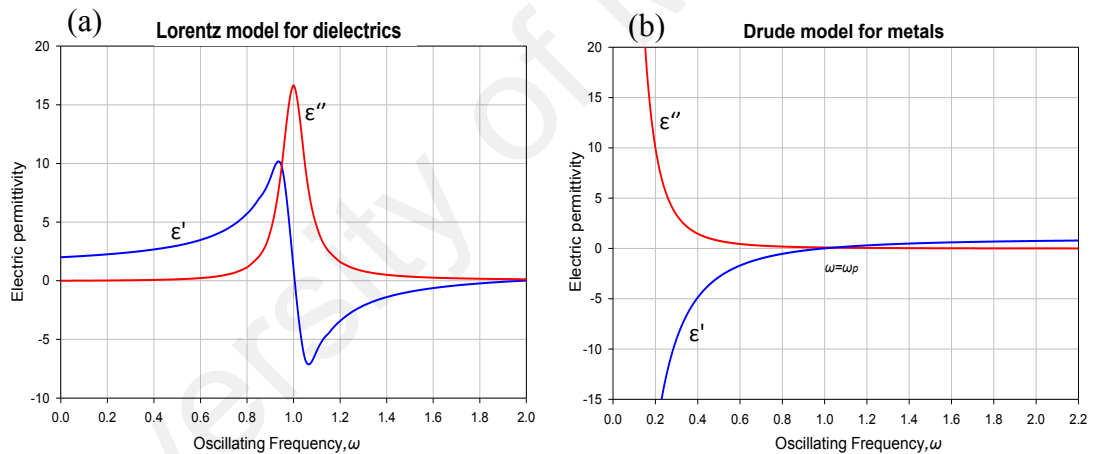


Figure 2.5: Typical electric response (a) Lorentz model for dielectric (b) Drude model for metals (Equation 2.8,2.9)

The weak damping is ($\omega \gg \gamma$), then can be simplified ε to:

$$\varepsilon(\omega) = 1 - \left(\frac{\omega_p}{\omega} \right)^2 \quad (2.10)$$

The dielectric function in Equation 2.10 shows that the real value dominated and imply that the absorption of the wavelength can be neglected. For frequencies below the plasma frequency of $\omega \ll \omega_p$, the dielectric permittivity becomes negative, and the metal is

reflecting. On the other hand, for high frequencies $\omega \gg \omega_p$ the metal will behave with dielectric-like properties and light can be propagated. The undamped case in Equation 2.10 is only valid for near-infrared frequencies. For most real metals, interband transitions (600 nm-800 nm) also contribute to the absorption.

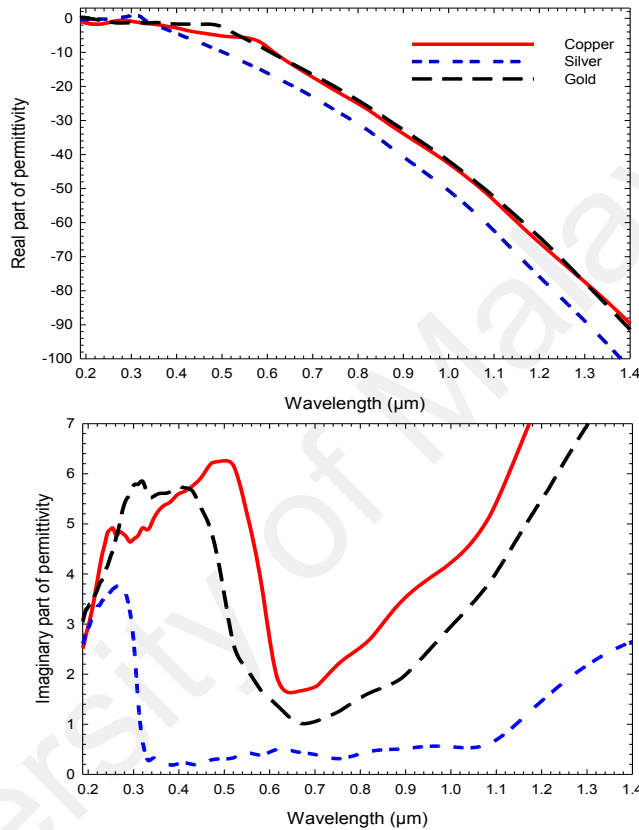


Figure 2.6: Real and imaginary parts of dielectric constant of copper, silver, and gold corresponding the experimental value from Johnson and Christy (P. B. Johnson & Christy, 1972)

Figure 2.6 shows the real and imaginary permittivity for three pure metal: gold, copper, and silver, commonly used experimental data from Johnson and Christy (P. B. Johnson & Christy, 1972). In this thesis, even though gold is the best metal; the copper because is used not only inexpensive but its dispersion relation almost identical to gold as shown in Figure 2.6.

2.4 Maxwell's and Wave's Equations

Maxwell's equations is presented which provide the fundamentals equations about the electromagnetic response:

$$\nabla \times \vec{E} = -\frac{\partial \vec{B}}{\partial t} \quad (\text{Faraday's Law}) \quad (2.11)$$

$$\nabla \times \vec{H} = \vec{J} + \frac{\partial \vec{D}}{\partial t} \quad (\text{Ampere's Law}) \quad (2.12)$$

$$\nabla \cdot \vec{D} = \rho \quad (\text{Gauss' Law}) \quad (2.13)$$

$$\nabla \cdot \vec{B} = 0 \quad (2.14)$$

where is \vec{E} the electric field (V/m), \vec{H} is the magnetic field (A/m), \vec{D} is the dielectric flux (C/m), \vec{B} is the magnetic flux density (T), \vec{J} is the current density of free charges, and ρ is the free charge density.

The material properties relate the fields with following equations:

$$\vec{D} = \epsilon_0 \vec{E} + \vec{P} \quad (2.15)$$

$$\vec{B} = \mu_0 \vec{H} + \vec{M} \quad (2.16)$$

where is ϵ_0 the free-space dielectric permittivity, which is equal to 8.85×10^{-12} F/m and μ_0 is the free-space magnetic permeability, which is equivalent to $4\pi \times 10^{-7}$ H/m. \vec{P} is the polarization density field for the medium, which presented as the dipole moment per unit volume, and \vec{M} is the magnetization, which is the magnetic moment per unit volume.

In a dielectric medium, the magnetization term is negligible. Also, we consider in a dielectric medium which contains no free charge ($\rho = 0$) and no free currents $\vec{J} = 0$. Taking the curl operator of Equation (2.11) and (2.12) and using Equation 2.15 and 2.16, the wave equation can be described as:

$$\nabla \times \nabla \times \vec{E} = -\mu_0 \frac{\partial^2 \vec{D}}{\partial t^2} \quad (2.17)$$

By using the identity from vector calculus

$$\nabla \times \nabla \times \vec{E} = \nabla(\nabla \cdot \vec{E}) - \nabla^2 \vec{E} \quad (2.18)$$

For isotropic media, note that $\nabla \cdot \vec{E} = 0$ the wave equation can be written in a form of

$$\nabla^2 \vec{E} - \frac{\epsilon}{c^2} \frac{\partial^2 \vec{E}}{\partial t^2} = 0 \quad (2.19)$$

where ϵ is permittivity of the material and $c = \frac{1}{\sqrt{\epsilon_0 \mu_0}}$ is the speed of light in vacuum.

Assuming a harmonic time dependence $\vec{E}(\vec{r}, t) = E(\vec{r})e^{-i\omega t}$, equation 2.19 will reduce to:

$$\nabla^2 \vec{E} - k_0^2 \epsilon \vec{E} = 0 \quad (2.20)$$

where $k_0 = \frac{\omega}{c}$ is vacuum wave-vector. Equation 2.20 is the Helmholtz equation for the electric field.

2.5 Recent Advances Plasmonic Photonic Crystal Fiber

2.5.1 Metal-filled PCF Fabrication

The flexibility to engineer the holey structures of PCF provides the ability to control its wave-guiding properties such as endlessly-single mode. Consequently, PCF has

enabled a variety of structures – including a metal-filled PCF with plasmonic properties and a lot of potential applications. Metal-filled PCF (microwire and nanowires) are embedded within PCF holey channel for achieving surface plasmon resonance (Li, 2017; Gong, 2017; Ando, 2017; Li, 2016; Wong, 2015; Zhen-Kai, 2014; Zhang, 2014; Zhang, 2012; Zhang, 2007).

Generally, there are two methods of producing metal-in-glass: bottom-up and top-down approach. A small amount of literature on metal-in-glass fabrication has been published. The well-known bottom-up approach to produce wires in glass waveguide are photolithography or electron-beam lithography, solution based synthesis (Baik, Lee, & Moskovits, 2009; Z. Xu, Shen, Sun, & Gao, 2009), template-based electrodeposition (Martin, 1994; Skinner, Dwyer, & Washburn, 2006), and physical vapor deposition (Durkan, Schneider, & Welland, 1999). Solution-based synthesis, in particular, lends to the fabrication of large quantities of single crystalline and smooth surface nanowires. However, the technique, like most others, could not produce long lengths more than 1 cm of continuously conductive wires and require multiple processing stages.

Top-down processes could solve the above challenges, although the method has not been widely investigated. The advantages of this method include a simple production method, reduce metal's wastage, well-suited for mass production and the output of the single microwire can be easily isolated and thus characterized.

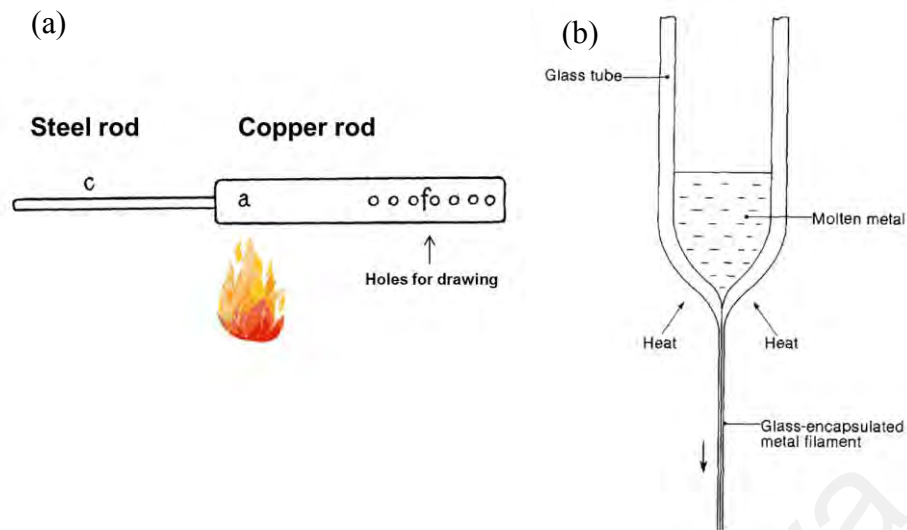


Figure 2.7: (a) Schematic of the rudimentary furnace used by Taylor in the first glass/metal drawing reported in 1924, extracted and adapted from (G. F. Taylor, 1924) (b)

Schematic illustration of the Taylor wire technique, extracted from (Donald, 1987)

Taylor (G. F. Taylor, 1924) reported a process for producing fine metal wires encapsulated in glass in 1924. This method subsequently patented in 1931. In the original method which became known as ‘Taylor-wire process’, he presented four main steps. Firstly, the metal was inserted into 2 mm internal diameter of the glass which sealed at one end. This end of the glass was heated in a gas flame until the metal melts, and the glass softened. Then, the end of the tube was pulled by hand to produce metal filled rod of 0.5 to 1.0 mm diameter with 300 mm long. Subsequently, these rods were redrawn to the diameter by passing through a furnace held at an appropriate and uniform temperature to produce a continuous wire encapsulated in the silica. A cooling device, consisting of a water-cooled metal cylinder is placed right below the heating furnace as an aid for producing a quality wire. He emphasized that the glass’ softening point, metal’s melting point and viscosity of both materials used must be compatible with one another. The Taylor-wire process approach is one of the more practical ways of producing metal-in-glass, owing to its feasibility, inexpensive, simple and non-trivial process. It is worth mentioning that Taylor developed this method not specifically for optics and plasmon applications. The main purposed was to manufacture the metallic filaments with micro

dimension for resistance (Logvinenko, Mikhina, & Mende, 1984), thermocouples, and bolometers (Conn, 1945). This method was successfully used to produce metallic filaments with high tensile strength of Pb, Bi, Au, Ag, Sn, Fe, Cu, Ti, Cd, Co, Sb, Ga and In with a variety of glass (G. F. Taylor, 1924).

A number of authors have reported adopting a method based around Taylor wire process. In (Markus A Schmidt, Sempere, Tyagi, Poulton, & Russell, 2008), work in pumping molten metal into the hollow channels of a photonic crystal fiber at very high pressure is reported. Metal core sizes of 120 nm were successfully produced but are limited to only a few cms in length. Jing Hou (Hou et al., 2008) presented fabrication of selectively metal-filled in the hollow core PCF. The author reported the fabrication of copper-filled PCF by modified stack-and-draw method. Jing Hou mentioned that the fiber size could not be reduced while maintaining the PCF structure due to the instability of fabrication's processes. In 2010 (Tyagi et al., 2010), Tyagi and his colleagues developed a gold-filled step index fiber to study the interaction between the step-index core guided mode and the plasmon resonance from the gold nanowire. The method of fabrication is similar to Schmidt's proposed work. The fabrication involves preparing the step index fiber with hollow channel placed next to the core. Then, by applying vacuum at one end the molten gold was filled in the hollow channel. Tyagi reported to produce 260 nm gold nanowire with only the length of 20 μm and separated by micrometer-gaps. One major drawback of this approach is that to fill the tiny holes with metal in long fiber lengths is extremely challenging. Also, the produced wire was not uniform and continuous. As presented in (Tuniz et al., 2011), the fabrication of magnetic metamaterials devices using fiber drawing method successfully fabricated. The technique presented allows continuous wire by kilometers. However, the material used in this fabrication is Poly (methyl methacrylate) -PMMA and indium metal. In 2014 (Percival, Vartanian, & Zhang, 2014) demonstrated the ultra-long platinum and gold nanowires by preparing a small part of

gold microwire placed in quartz, followed by pulling it using a bench-top micropipette laser. The nanowires inside the quartz can be easily released by removing the quartz with HF acid etching. However, only short length of the wire produced and the size of the quartz was not uniform. Different fabrication techniques for metal wires are summarized in Table 2.1.

University of Malaya

Table 2.1: Different metal wire fabrication techniques

Fabrication Technique	Wire Diameter	Wire Length	Fabrication Conditions	Reference
Pulled by hand under the flame near to softening point of the glass. (Taylor-wire process)	10 μm	300 mm	High temperature at 1200 $^{\circ}\text{C}$	(G. F. Taylor, 1924)
High-temperature pressure cell technique	120 nm	Up to 40 mm	High temperature at 1100 $^{\circ}\text{C}$ and 60 bars of pressure	(Markus A Schmidt et al., 2008)
Modified stack-and-draw with the combination of Taylor-wire process	4.2 μm	70 mm	High temperature at 1880 $^{\circ}\text{C}$	(Hou et al., 2008)
High-temperature pressure cell technique	260 nm	20 μm	High temperature at 1100 $^{\circ}\text{C}$ and 60 bars of pressure	(Tyagi et al., 2010)
Modified stack-and-draw with the combination of Taylor-wire process (using PMMA)	<10 μm	Up to kilometer	Low temperature at 156.6 $^{\circ}\text{C}$	(Tuniz et al., 2011)
Laser pulled	10 μm	1 mm	Pull using a bench-top micropipette laser	(Percival et al., 2014)

2.5.2 Design and Applications

A considerable amount of literature has been published in designing the plasmonic PCF [Rifat, 2015; Liu, 2015; Liu, 2015;Khaleque, 2015;Khaleque, 2015; Jiang, 2015; Jiang, 2015; Heikal, 2015; Heikal, 2015; Fan, 2015; Fan, 2015; Chen, 2015; Zhen-Kai, 2014(Bei et al., 2018; Dou, Jing, Li, Wu, & Wang, 2018a, 2018b; Paul, Sarkar, Rahman, & Khaleque, 2018; J. Wang et al., 2017; J. Wu, Li, Jing, Dou, & Wang, 2018; W. Zhang, Lou, & Wang, 2018; Zhou, Li, Cheng, & An, 2018)]. The reported proposed designs are classified based on their applications – biosensors, polarization filter, polarization splitters, and couplers. The key aspect of plasmonic PCFs is the high losses exhibited at a particular wavelength when the core-guided mode are strongly coupled to SPP modes. Thus, this interesting property invites interest and effort in developing filter and splitter based fiber devices and which can operate at a specific wavelength. However, most of the reported works did not report the fabrication process and only describe the simulation and numerical analysis. In this section, the designs of plasmonic PCF structures, mainly incorporating metal wires and their characteristics is reviewed. Figure 2.8 illustrated a general single core PCF with metal-filled located next to PCF's core which works as a polarization filter.

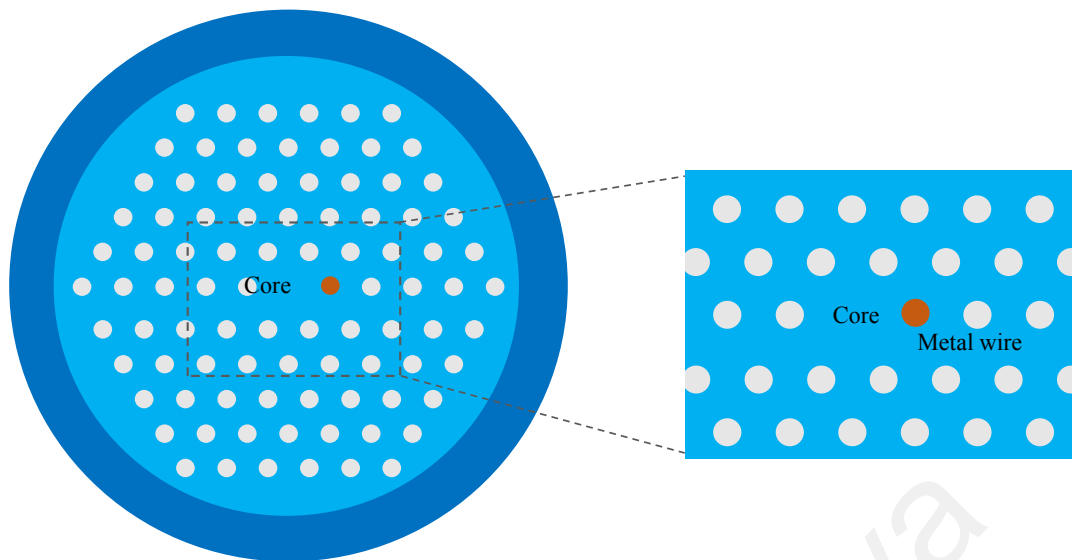
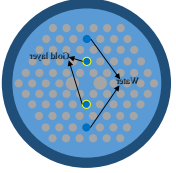
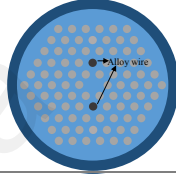
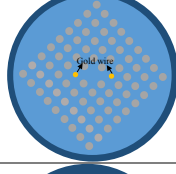
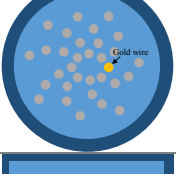
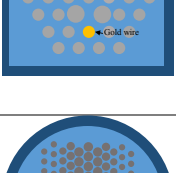
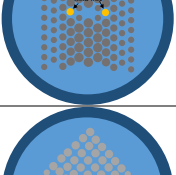
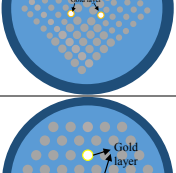
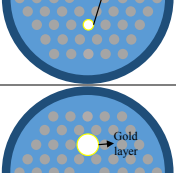
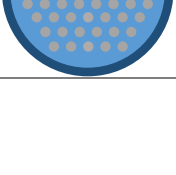


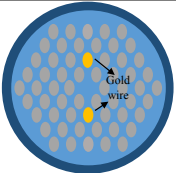
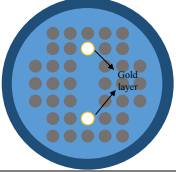
Figure 2.8: Single core PCF with metal-filled located next to PCF's core for polarization filter

In (Xue et al., 2013) the author presented two designs for polarization-wavelength dependent filters with gold nanowires in PCF with triangular-lattice of air holes. The proposed design achieves a loss of 275 dB/cm and 400 dB/cm in x- and y-polarization respectively. Du claimed the proposed design could filter wavelength at 1125nm, 1275 nm, 1295 nm, and 1550 nm. Fan *et. al* in 2014, (Fan et al., 2015) proposed a polarization-maintaining D-shaped PCF with a gold nanowire. The device operates at 1310 nm and 1510 nm, with optical bandwidths of 88 and 150 nm, respectively. The alloys of silver and gold composition have been reported by Shi (Shi et al., 2015) in 2014. Shi developed the plasmonic devices which control the composition of the alloy to achieve plasmonic resonance particular wavelength. In contrast, PCFs with square-lattice cladding with metal-incorporated microwires also gives significant attention for polarization wavelength-dependent filtering devices. Zhang et.al (W. Zhang, Li, An, Fan, & Bao, 2014) introduced the square lattice PCF with solid core and gold wire. Zhang reported that the diameter of the gold microwire and how the air holes being arranged around the PCF's core would give a major effect on the characteristic of the filter. Similarly as reported by An, (An, Li, Yan, Yuan, & Zhang, 2016) by adjusting the size of the gold

microwire, the characteristics of the filter can be tuned at a different wavelength. Jiang *et. al* (L.-h. Jiang et al., 2016) aimed the ultra-short PCF with single polarization filter at 1310 and 1500 nm wavelength. Single gold wire was filled in the holey channel next to the PCF's solid core in the square lattice holey cladding. Jiang also reported a single polarization filter of ultra-broadband bandwidth by injecting liquid crystal core in a hollow channel and incorporates a single gold wire next to the core. The numerical results told us that the said design was capable to obtain ultra-high extinction ratio with 850 nm width for the broadband single polarization applications. Heikal in (Heikal, Hussain, Hameed, & Obayya, 2015) investigated a polarization filter based on an elliptical core with spiral structure and incorporating gold wires into one of the air-holes. The study found that the coupling between the core-guided mode and SPP mode can be altered by varying the parameters of the PCF's structure and the number of gold wires thus the device able to filter at different wavelength. Recently, more literature with different structures have been reported (Bei et al., 2018; Dou et al., 2018a, 2018b; Lou, Cheng, & Li, 2018; Junjun Wu, Li, Dou, & Liu, 2017). The performances of the polarization filters wavelength-dependent based on metal-filled PCF are summarized in Table 2.

Table 2.2: Different PCF design for the polarization filter wavelength-dependent based on metal-filled PCF

PCF design	Metal	Loss for x-polarization (dB/cm)	Loss for y-polarization (dB/cm)	Operating wavelength (nm)	References	Design
Solid core PCF with triangular lattice PCF	Gold layer	275	400	1125, 1275, 1295, 1550	(Xue et al., 2013)	
Solid core triangular lattice PCF	Gold/Silver alloy wires	24.42	309.14	1100	(Shi et al., 2015; W. Zhang et al., 2014)	
Solid core rhombus lattice PCF	Gold wires	279.1, 399.18	7.89, 10.2	1020, 1550	(W. Zhang et al., 2014)	
Spiral PCF with elliptic core	Gold wire	80.14	63.23	1183	(Heikal et al., 2015)	
D-shaped triangular lattice PCF	Gold wire	4, 4.6	208.4, 249.5	1310, 1550	(Fan et al., 2015)	
Solid core square lattice PCF	Gold wires	231.6	237.9	1310, 1550	(An et al., 2016)	
Solid core rhombus lattice PCF	Gold layer	9.41, 214.31	373.9, 3.88	1310, 1550	(L.-h. Jiang et al., 2016)	
Solid core PCF with triangular lattice PCF	Gold layer	-	803.56, 732.69	1550, 1480	(Junjun Wu et al., 2017)	
Solid core PCF with triangular lattice PCF	Gold layer	-	2318.24	1.26-1.55	(W. Zhang et al., 2018)	

Elliptical PCF	Gold wire	1.5	333.84	1.55	(J. Wu et al., 2018)	
Solid core PCF with octagonal lattice	Gold layer	729.47	542.78	1.31 1.55	(Lou et al., 2018)	

University of Malaya

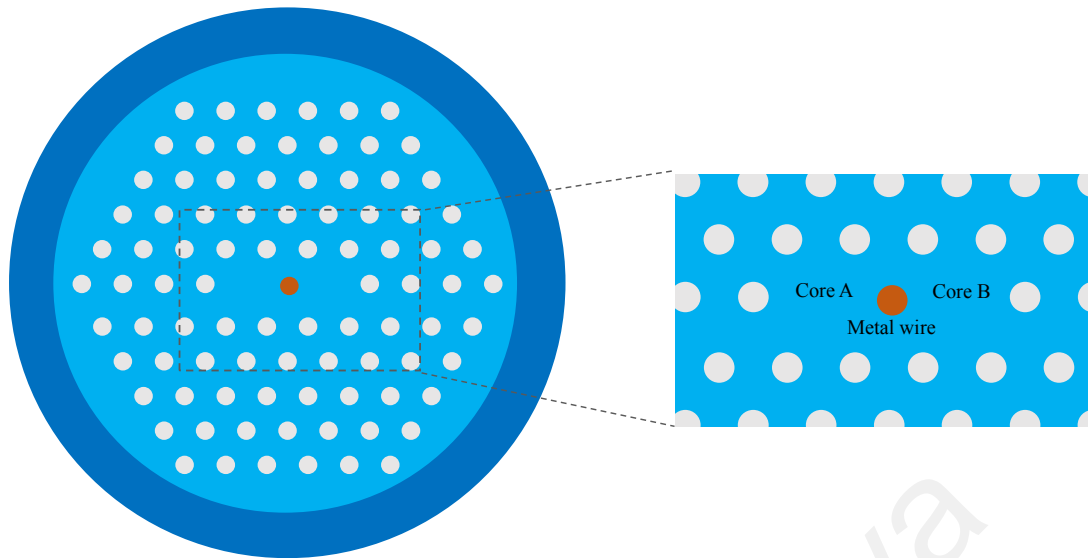
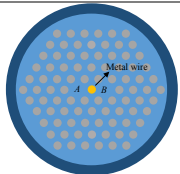
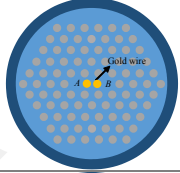
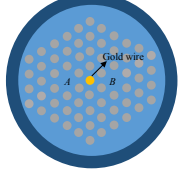
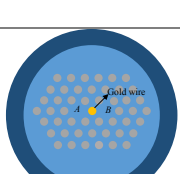
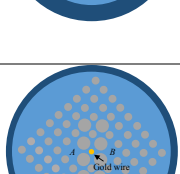
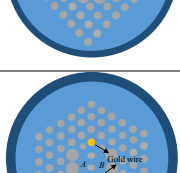
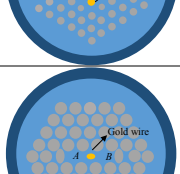
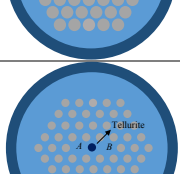
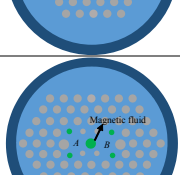


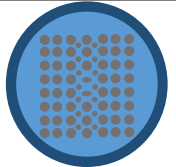
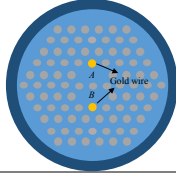
Figure 2.9: Dual-core PCF with metal-filled located between the PCF's cores for polarization splitter

Besides polarization filtering devices, polarization splitting could be achieved with dual-core PCFs and metal-filled wire located between the cores as depicted in Figure 2.9. The polarization splitting characteristics utilize the difference in resonance coupling of odd and even supermodes, high polarization and high birefringence dependence in transmission (Fan, Li, Liu, Chen, & Wang, 2016; L.-h. Jiang et al., 2016; P. Li & Zhao, 2013; Q. Liu et al., 2015; Lu, Lou, & Wang, 2013; Shi et al., 2015; Sun, Chen, Zhang, & Zhou, 2015; Sun, Chen, Zhou, & Zhang, 2013; S. Zhang et al., 2012). As in dual-core PCFs, the extinction ratio between each output fiber core can be specified as the ratio of undesired power and the desired power of polarization. Zhang *et. al* (S. Zhang et al., 2012) proposed dual-core PCF with triangular lattice arrangement with silver-coated and silver wire which placed between the dual core. The author introduced the supermode and coupled mode theory to investigate the enhancement of the power transfer between each fiber core. The presence of the plasmonic material between the dual cores would give a difference in resonant wavelength at the phase matching condition. Zhang claimed that the proposed design could achieve a coupling ratio of up to -30.5 dB. Similarly, Li *et. al.* (P. Li & Zhao, 2013) presented the difference in confinement loss, resonance coupling, dispersion for odd and even supermodes in dual-core PCF with gold-nanowires in

between both cores. The author proved that two orthogonally polarized light can be split exactly at 1330 nm. The light input in one core was only x-polarized and the other core was only y-polarized after a certain propagation length. The extinction ratio of the orthogonal polarization in each core was about -40 dB. In (Sun et al., 2013), the polarization splitter of 63 mm length was proved by using silver wire-filled in dual-core PCF. The PCF's coupling length ratio of x- and y- polarized showed the two orthogonal polarizations of a factor two. They also claimed that the bandwidth of the proposed splitter was over a 146 nm wavelength range with an extinction ratio below -20 dB. Two years later, Sun (Sun et al., 2015) improved the design by obtaining a shorter fiber length with a broader bandwidth. Khaleque *et. al* (Khaleque, Mironov, & Hattori, 2015) proposed the polarization splitter with PCF structures of high-birefringence with two gold wires filled in the cladding for wide broadband PCF splitters. Dual-core PCF with triangular lattice arrangement comprised an elliptical gold in the centre of PCF for polarization splitting at 1310 nm and 1550 nm in (Fan et al., 2016). In contrast, a dual-core square-lattice cladding PCF used a gold wire in the center was demonstrated by (Dou et al., 2018a; L. Jiang, Zheng, Hou, Zheng, Jiying, et al., 2015). The proposed design presented ultra-broadband polarization splitters at 1550 nm wavelength with an extinction ratio of -78.2 dB better than -20 dB and bandwidth of 430 nm. Table 3 summarizes the performance of the polarization splitters utilizing metal-filled dual-core PCF.

Table 2.3: Polarization splitters using different types of metal wires

Metal/Material	Length (mm)	Extinction Ratio-A (dB)	Extinction Ratio-B (dB)	Operating Wavelength (nm)	Bandwidth below -20 dB (nm)	References	Design
Silver	-	-30.54	-	1550	-	(S. Zhang et al., 2012)	
Gold	0.5942	-40	-40	1310	-	(P. Li & Zhao, 2013)	
Silver	63	-39.4	-35.2	1550	x-pol:1441-1587 (146 nm) y-pol:1430-1605 (175 nm)	(Sun et al., 2013)	
Silver	0.5775	-34	-42	1596	x-pol:1439-1689 (250 nm) y-pol:1421-1700 (279 nm)	(Sun et al., 2015)	
Gold	4.036	-78.2	-	1550	1250-1680 (430 nm)	(L. Jiang, Zheng, Hou, Zheng, Jiying, et al., 2015).	
Gold	0.117	-100	-	1550	x-pol: 1250-1710 (460 nm)	(Khaleque et al., 2015)	
Gold	2.937	-70	-	1310	x-pol: 1290-1380 (90 nm)	(Fan et al., 2016)	
Tellurite	0.51	-20	-	1550	1461-1745 (284 nm)	(Q. Liu, Li, Gao, & Feng, 2017)	
Magnetic Fluid	8.13	-100	-	1550	-	(J. Wang et al., 2017)	

Air-filling	0.103	-73	-45	1550	1458-1635 (177 nm)	(Dou et al., 2018a)	
Gold	0.290	-56.5	-	1550	1540-1599.2 (19.2 nm)	(Q. Xu, Zhao, Xia, Lin, & Zhang, 2018)	

2.6 Summary

An overview of metal-filled PCF has been presented covering the PCF's key parameter, optical properties of metal and recent advances in metal-filled PCF in fabrication technique and application. Metal-filled PCF has potential applications in passive optical devices such as polarization filter and splitter which is important in integrated optics. Most literature was only based on numerical study and analysis. Thus, in this work, we will design, fabricate and characterize the metal-filled PCF.

In the following chapter, fabrication of copper-core cane and fiber will be presented. A technique which was based around the Taylor wire's process is adopted by utilizing the fiber drawing tower facilities in the Faculty of Engineering, University of Malaya. Following from this, the copper-cane is used to fabricate copper-filled photonic crystal fiber.

CHAPTER 3: COPPER-IN-GLASS FABRICATION METHODS

3.1 Introduction

This chapter concerns the details of fabrication method of copper-in-glass. We fabricated the metal-dielectric waveguide via a standard optical fiber drawing approach. This method opens the possibility of nano-sized copper wires encapsulated in silica. We introduce the fabrication facilities for fiber drawing which are available in the University of Malaya. Then, we discuss the general process for fabrication of the optical fiber – pre-, during and post-fabrication process. The following section will briefly discuss the fabrication process of copper-core optical fiber, which is the main component in fabricating the copper-filled photonic crystal fiber. We tested the fabricated copper-core optical fiber in terms of its electrical continuity and conductivity.

3.2 Fabrication Facilities

This section introduces the fabrication facilities for fiber drawing at the University of Malaya. The facilities are operated by Integrated Lightwave Research Group (ILRG). The 5 metres fiber drawing tower is located in Faculty of Engineering. The furnace heating capability is up to 2700 °C. The fiber tower includes a high-precision motorized chuck, vacuum/pressure system, pyrometer, preform feeder, coating unit, fusion ultra-violet curing system, laser diameter gauge, capstan wheels with built-in tension monitor, cane puller, drum winder, dancers/tensioners, and furnace chiller. Figure 3.1 and Figure 3.2 depict the schematic diagram and images of the fiber drawing tower, respectively.

The furnace is vacuumed and purged with argon gas before fiber drawing to eliminate impurities and prevent oxidization of the furnace elements. Argon gas is set to flow continuously after purging to create a low oxygen environment in the furnace. Subsequently, a fiber preform is fixed firmly at the high precision motorized chuck, which

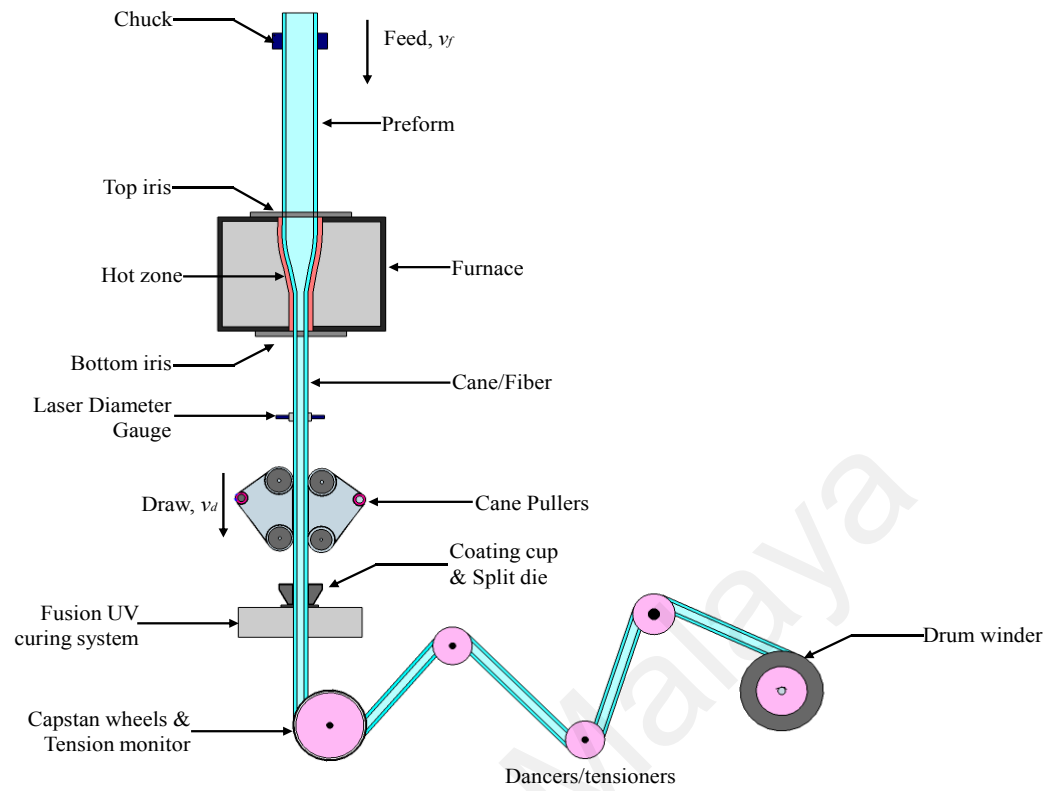


Figure 3.1: Schematic of Fiber Draw Tower in University of Malaya is capable of feeding preform into the furnace at the rate of 0.2-20 mm/min with 0.1 mm/min resolution.

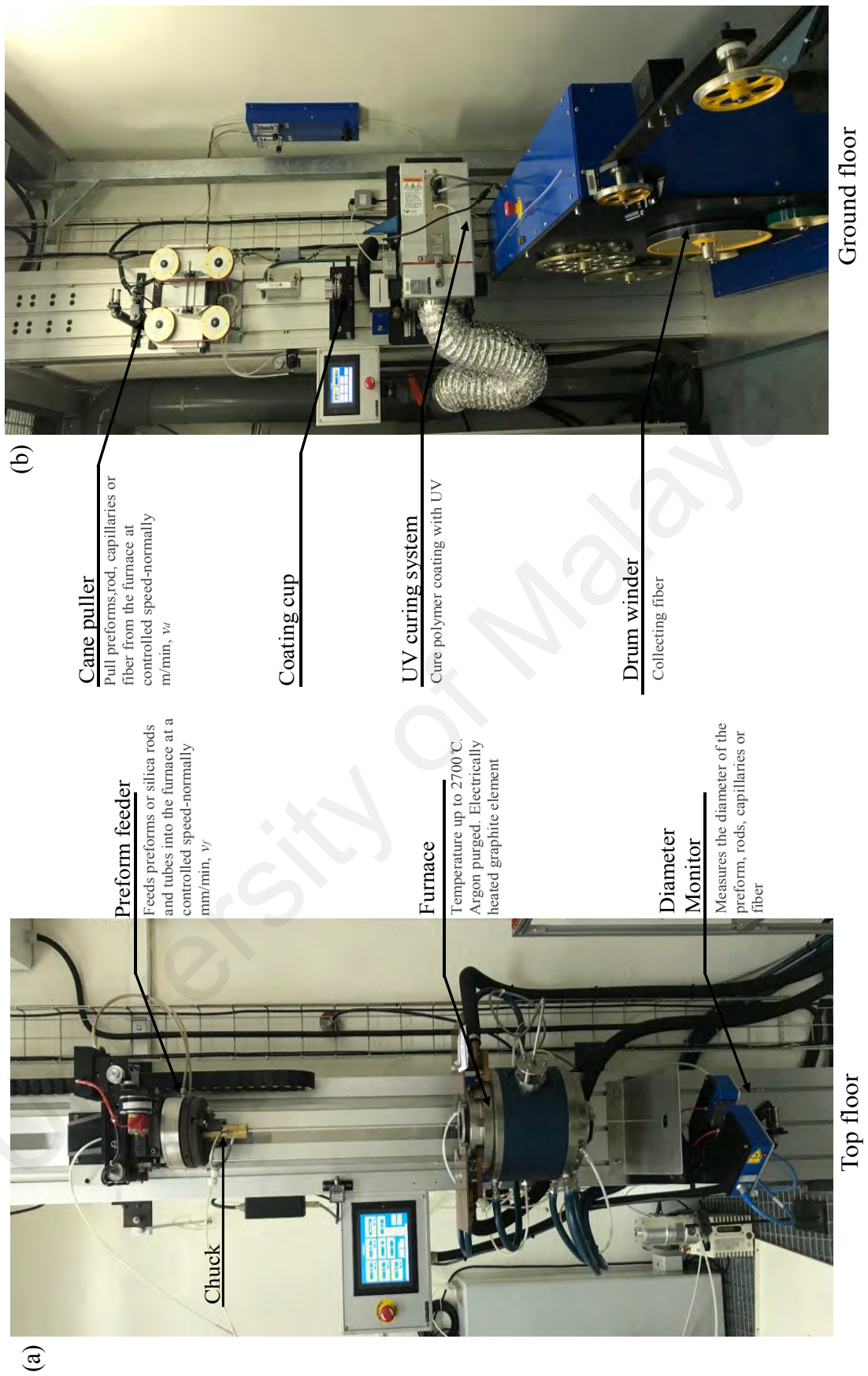


Figure 3.2: (a) Top-floor elements (b) Ground floor elements

3.3 General Fabrication Process

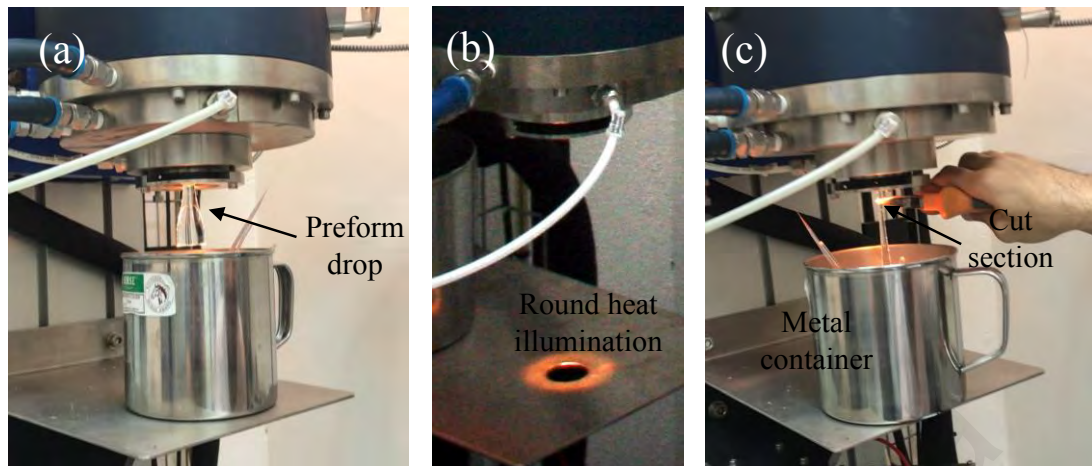


Figure 3.3: (a) Preform's drop passing through the bottom iris. (b) Round heat illumination appears from the bottom iris. (c) Cutting at the neck-down of the preform.

The furnace's top iris are opened and the fiber preform is lowered slowly until it gets to the same degree as the furnace's top opening. Transverse x-y position of the preform is adjusted to the middle of the furnace bore. Then, the vertical position of the preform is reset and the preform is loaded into the furnace for a distance of approximately 155 mm. The vertical position of the heat zone from the furnace top entry is 125 mm. Thus, the preform drop (Figure 3.3 (a)) will be approximately 35 millimeters in length. When the preform is in position, the furnace temperature is set to ramp up gradually from room temperature to the silica melting point, 2100 °C. About 10 minutes is required for the furnace to reach the melting point. The furnace temperature is read by a pyrometer installed at the furnace's heat zone, which has a temperature range of 350-2500 °C with 1 °C resolution.

At melting point, the segment of the fiber preform of the heat zone develops a neck-down profile and sets about to sink. The preform drop generates gravitational force that elongates the fiber preform, resulting in a long section which is greatly reduced in diameter. Depending on the mass per unit length of the preform, the time taken for the preform drop to exit the furnace's bottom opening may vary from 10 to 15 minutes.

Assuming the same lengths of preform drops, those with larger mass per unit length will require more time for heat absorption before melting. Yet, the extended time is compensated by the large mass per unit length of the drop from the same preform which induces greater gravitational force and in turn precipitate the drop process. As the preform's drop starts to fall, the round heat illumination through the small opening of bottom iris will expand in diameter as shown in Figure 3.3 (b). By noticing this indication, the bottom iris must be opened immediately to let the preform drop pass through. The preform drop is then collected in a metal-container and cut at the neck-down section as depicted in Figure 3.3 (c).

The cut section is pulled gently by hand to reach the cane pullers. Alternatively, a small weight could be attached to the end of the cut section to give a constant and slow pulling speed as shown in Figure 3.4 (a). The cane pullers are set to clamp as the cut section reaches their central position. Subsequently, micro-screw controlling the spacing between the cane pullers are adjusted carefully to give a gentle grip to the cane, followed by starting the feeding and drawing speed simultaneously. If the preform is a cane, feeding speed should begin directly after cutting preform drop to prevent breaking of fiber within the furnace, which goes to unnecessary wastage of another preform drop. Feed rate and draw speed are set according to the simplified mass conservation equation to obtain approximate final sizes.

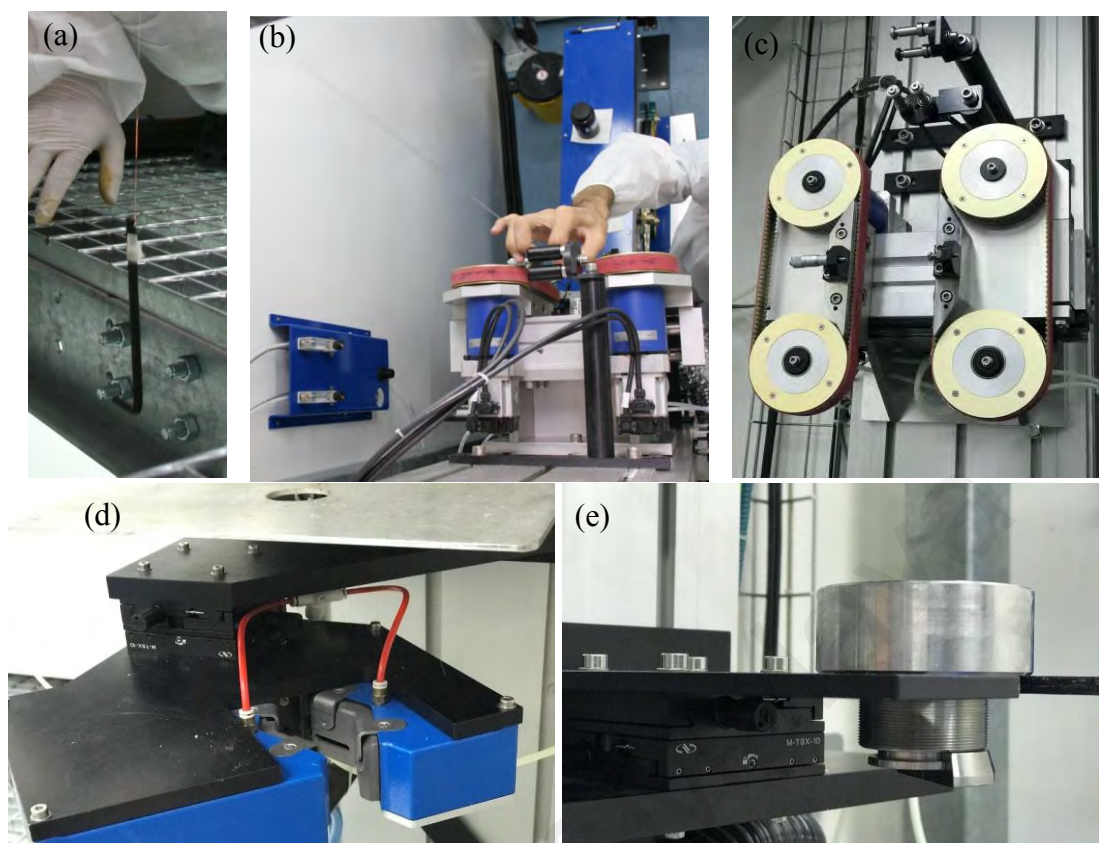


Figure 3.4: (a) Attaching a small weight to pull the fibers at a constant rate (b) Applying speed after the fiber reached the clamp (c) the clamp (cane pullers) which controls speed (d) laser diameter gauge (e) coating cup.

The size of fiber/cane is measured in-line by a laser diameter gauge (Zumbach USYS 2100, ODAC18XY), as depicted in Figure 3.4 (d) which can read diameter in the range of 0.08-18.00 mm with resolution of 0.1 μm . A coating cup with split die as shown in Figure 3.4 (e) of 375 μm diameter orifice is used, together with the fusion UV curing system. The UV lamp power is controlled automatically with respect to the draw speed.

For optical fiber pulling, the fiber size is first adjusted to reach around the intended size by using the cane pullers as shown in Figure 3.5 (a), followed by winding the fiber according to the predefined route starting from the tension meter, then to the capstan wheels (Figure 3.5 (b)), dancers (Figure 3.5 (c)) and finally to the drum winder (Figure 3.4 d). After winding is completed, cane pullers are unclamped and capstan wheel is set to turn at the specified draw speed. As the size of fiber stabilizes at the intended diameter, acrylate coating could be applied to the fiber.

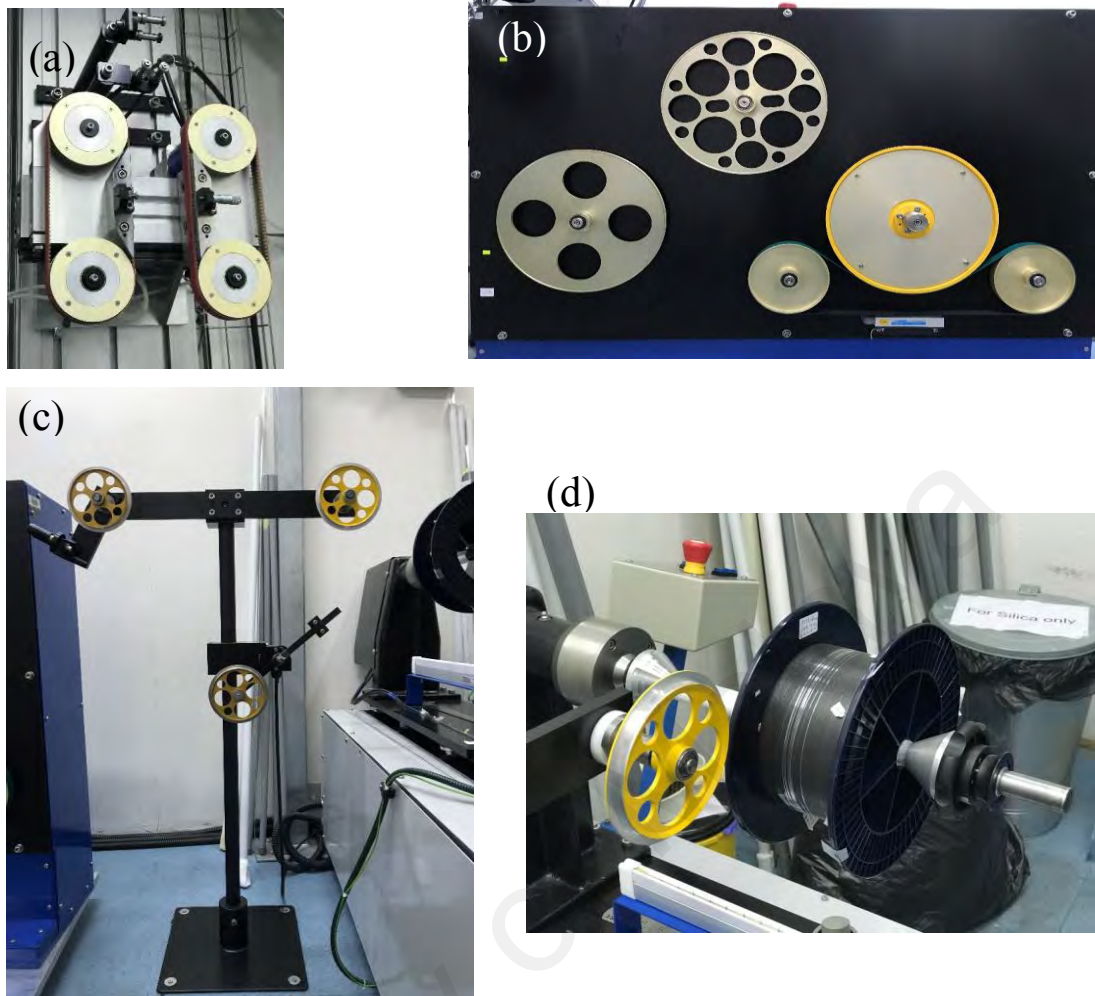


Figure 3.5: (a) Cane pullers (b) Capstan wheel and tension meter (c) Tensioner/Dancers (d) Drum winder

Further details on optical fiber fabrication are outlined in (Izawa & Sudo, 1987; T. Li, 2012). Here, some additional practical aspects pertaining to fiber fabrication in UM are discussed. The fiber drawing facilities are installed in a cleanroom environment. Humidity and room temperature are set at 50 Rh% and 24 °C respectively. In the event where preform vacuum or pressurization is needed, a custom-made preform mount is used to facilitate airtight gas transport between the vacuum/pressurization outlet pipes and preform tube. The preform mount was made from brass and was designed to fit the preform size, the inner structure consists of a hollow shaft with top and side openings. The weight of preform mounts alone could ensure airtight contact with the preform tube. No rubber contact is used in preform to mount as the thermoplastic behavior of rubber

prevents it to withstand high temperature. Throughout the whole process, both the top and bottom irises should be closed to avoid oxidation of the furnace's element. Due to the absence of an automatic temperature ramping feature between two intermediate temperatures, manual change of temperature of more than 200 °C should be done in a gradual manner (less than 50 °C per step) as any sudden and large shift of temperature may shorten the lifetime of the heating element. In order to avoid breaking of fiber at the beginning of pulling, the draw speed should start from 1 m/min and increase slowly towards the intended speed. The laser diameter gauge is set to display the fiber's *x* and *y* axis diameter and its ovality. In fabricating PCFs, ovality is a central indicator of the structural deformation.

In the event of drawing preform with the small diameter of less than 5 mm, the preform should be extended out of the bottom iris as the small preform weight will result in long waiting time for a drop. In this case, when the temperature reaches the softening point, the drop should be pulled down manually by hand. Using a dicing pen or ceramic cutter, short fiber samples are cut for every few meters of fiber length and viewed under the microscope to ensure their quality. The fiber is then inserted through the coating cup and fusion UV curing system before coating. At the same time, the fusion UV curing system is set to standby mode.

When the fiber size stabilizes, the drawing force is changed from cane pullers to capstan wheels. This process requires the presence of two operators, one person manually directs the fiber leading end to capstan wheels while another person unclamps the cane pullers and starts the capstan wheels simultaneously from the main control cabinet. Subsequently, the two split dies are attached to the coating cup slowly, the groove on split dies are aligned carefully to the moving fiber and tightened gently. Automatic transverse *x-y* alignment is activated to ensure fiber passes through the exact center position of the

coating cup, preventing fiber fracture due to scratching with split dies. The coating material used in this work is acrylate, the solution is heated up in a water bath at 50 °C for eight hours before coating. Depending on the amount needed, some solution is poured into the coating cup and the fusion UV curing system is set to operate immediately.

Fiber tension is monitored continuously throughout the whole process. When tension increases over 50 g, one should increase furnace temperature or reduce draw speed to avoid breaking of fiber. The fabricated fiber is then spooled to a polystyrene drum using a drum winder, initially in test band for quality checking before proceeding to the main band. For each fiber pulling session of two hours, at least 100 bar pressure of argon gas is needed. Nitrogen gas is used only in machine pneumatic movements and coating process, thus about 60 bar pressure is enough for a pulling session. After fabrication, the temperature of furnace is set to ramp down. To protect the furnace heating element from oxidation, only after the gas valve of furnace turns off automatically, the gas supply, main control cabinet, and the other equipment could be shut down accordingly.



Figure 3.6: Flow diagrams of the general fabrication process

3.4 Fabrication of Copper-Core Optical Fiber

Fabrication of high purity, precise dimensions, and ultra-clean interaction surfaces remains non-trivial in ensuring high repeatability (Hameed, Alrayk, Shaalan, El Deeb, & Obayya, 2016; W. Li, Ren, & Zhou, 2016; Liang et al., 2016). The ability to launch light into a surface plasmon structure without the use of prisms is an added advantage. Also, eliminating the use of free space optics in collecting plasmon chip outputs would lead to miniaturized modules, reducing the barrier to technological adoption. To this end, performing the plasmon process within a fiber structure is attractive as the approach lends to all the advantages mentioned above. This places the need to fabricate micron, or nano-sized metal wires – simply referred to here as nanowires – within an optical fiber structure.

The fabrication procedure involves the preparation of a quartz capillary. The quartz capillary (inner diameter: 10mm and outer diameter: 28mm) are cleaned by using isopropyl alcohol to eliminate dirt. We use pure copper powder with a particle size of $<63\mu\text{m}$. We prepared another quartz capillary for jacketing purpose (inner diameter: 3.5mm and outer diameter: 10mm) so that it can be inserted into the main capillary. With jacketed capillary, we could avoid the diffusion of molten copper into the glass wall which can lead the glass to break during the drawing process.

In producing these copper microwires via a standard fiber drawing method, we took three following key steps as schematically illustrated in Figure 3.7. Filling a few cm of a one-end-sealed glass tube (large diameter and wall-thickness) with copper bar and melt the copper inside the tube Figure 3.7(a). Due to relatively large air hole size in the tube, the molten copper can easily fill up the bottom of the tube and fill all spaces.

The copper-filled tube is first drawn into cane shape using first stage drawing as shown in Figure 3.7 (b). Due to the surface tension, the copper inside the output cane will become segmented with tens of cm continuous lengths and short gaps in between along the cane. Finally, by re-drawing one segment of the cane with continuous copper as shown in Figure 3.7 (b), the copper-core fiber can be fabricated up to several meters of micron-size fiber with continuous copper. The fabrication started by jacketing a quartz capillary measuring 3.5/9.8 mm inner to outer diameters were jacketed with another 10/28.8 mm tube using the furnace in drawing tower.

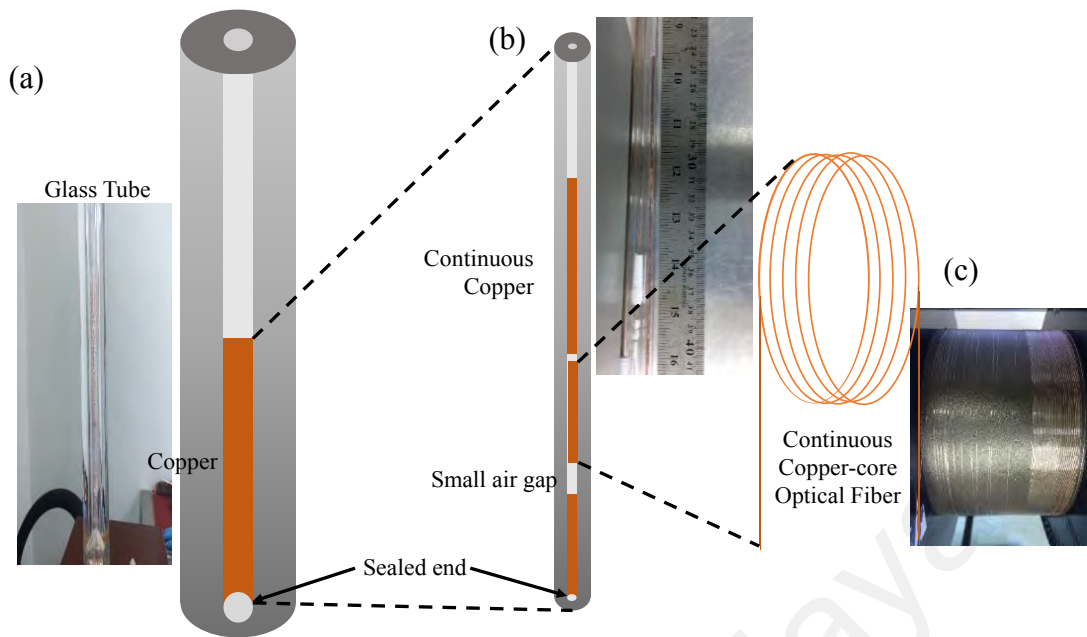


Figure 3.7: Copper-core optical fiber fabrication hierarchy, (a) bulk size tube glass with short-length copper-filled and melted inside, (b) copper-core cane fabricated from the preform in (a), and (c) output copper-core optical fiber.

This is performed by pressurizing the inner capillary where sealed from the bottom side and pressurized from the top by applying a pressure of around 75 kPa while the whole preform swept in the furnace's hot zone with a speed of 100 mm/min at a temperature of around 2100 °C. Next, around 10-15 cm length of the jacketed capillary was filled with copper powder.

The copper inside the capillary is then melted using the furnace in the drawing tower by sweeping it over the furnace hot zone area with a speed of 100 mm/min at temperature of around 1800 °C, while a piece of copper wire of 2 mm, also serves as a medium, was used to push and compact the copper powder in the said capillary. This copper rod is etched with dilute sulphuric acid to remove excess oxide. The resulting copper filled preform was then drawn into a cane measuring 3.5 mm in diameter. We used the simple conservation of mass equation to determine fiber pulling parameters such as preform feed and tractor feed rates which is summarized in Equation 3.1.

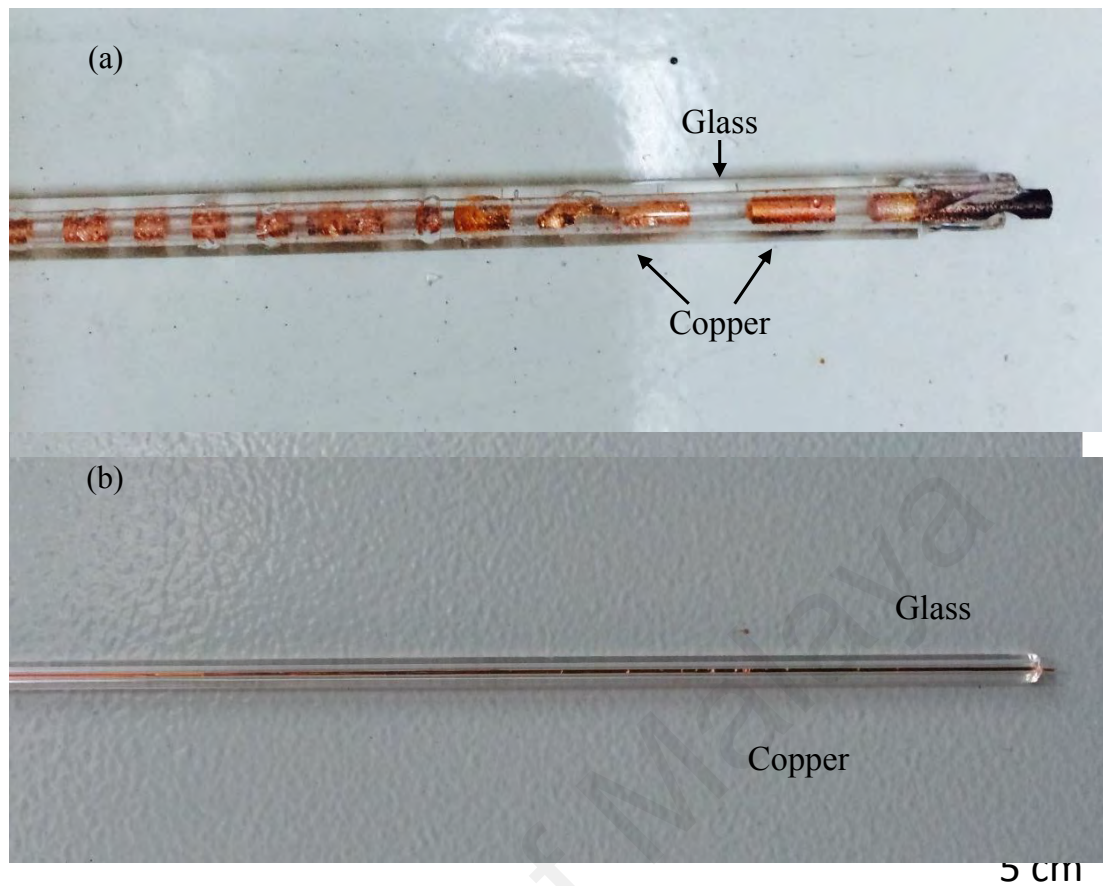


Figure 3.8: The longitudinal view of copper-cane showing (a) discontinuity of copper formed in the glass capillary without applying pressure with a copper rod. (b) The perfect continuous copper formed in the glass capillary.

$$A_1 V_f = A_2 V_d \quad (3.1)$$

Where A_1 and A_2 are the cross-sectional areas of preform and cane, while V_f and V_d are the feeding and drawing speeds, respectively.

The draw temperature was set to 2100 °C and feed rate and draw speeds were 14.5 mm/min and 1 m/min, respectively. Canes measuring up to 50 cm lengths with continuous copper layer were produced with no presence of discontinuity and bubbles. This is depicted in Figure 3.8(b). The image of fabricated copper-cane is depicted in Figure 3.9.

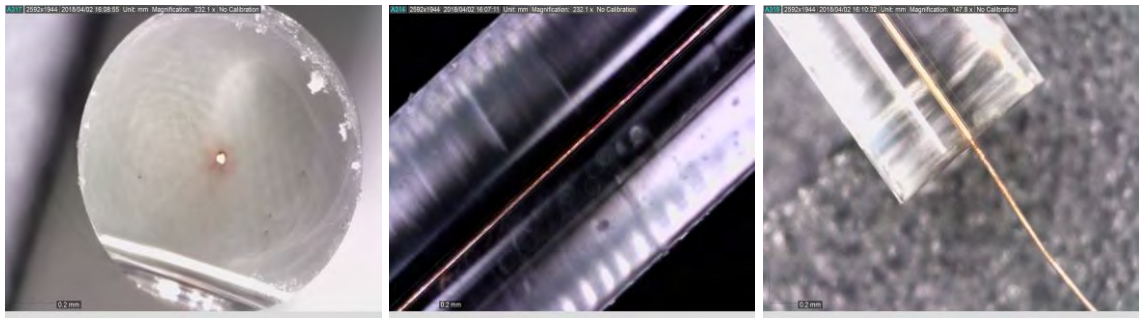


Figure 3.9: Images of cane size, copper-in-glass capillary

The short length of the cane necessitates the use of quartz handles/extensions to be attached to both ends of the cane to allow pulling into a fiber format as depicted in Figure 3.10 (b). The said handle/extensions are fused by oxygen-butane flame. We used 2.8 mm/min for the preform feed rate, 1.5 m/min for drawing speed at a temperature of 1930 °C. Hundreds of meters of copper core fiber were produced with dimensions measuring 22.9 μm copper core diameter, and an outer fiber diameter of 170 μm , as shown in Figure 3.11(a).

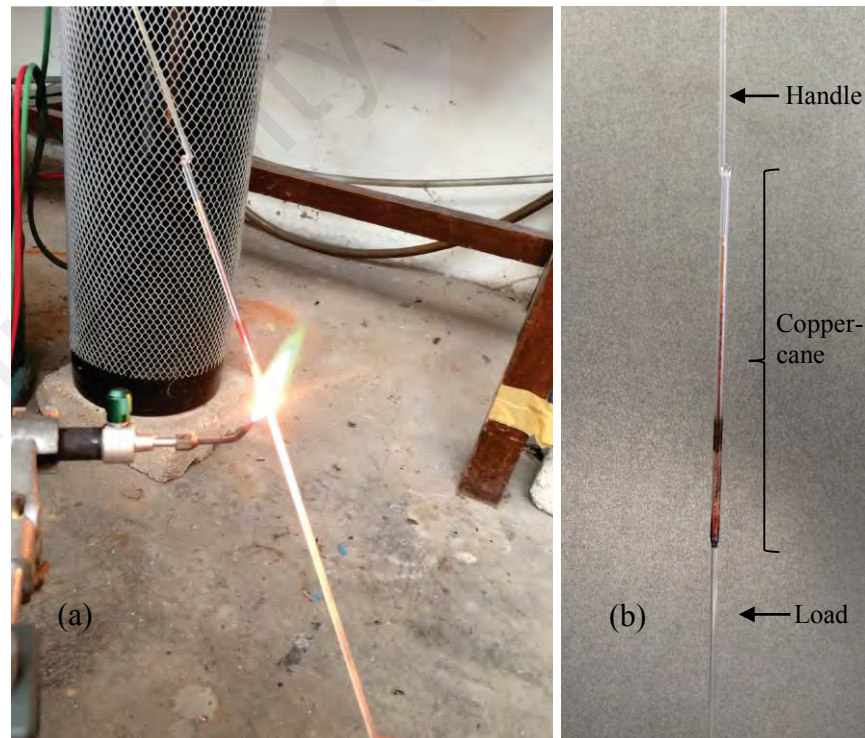


Figure 3.10: (a) Oxygen-butane flame to fuse handle and load (b) an extension of the copper cane.

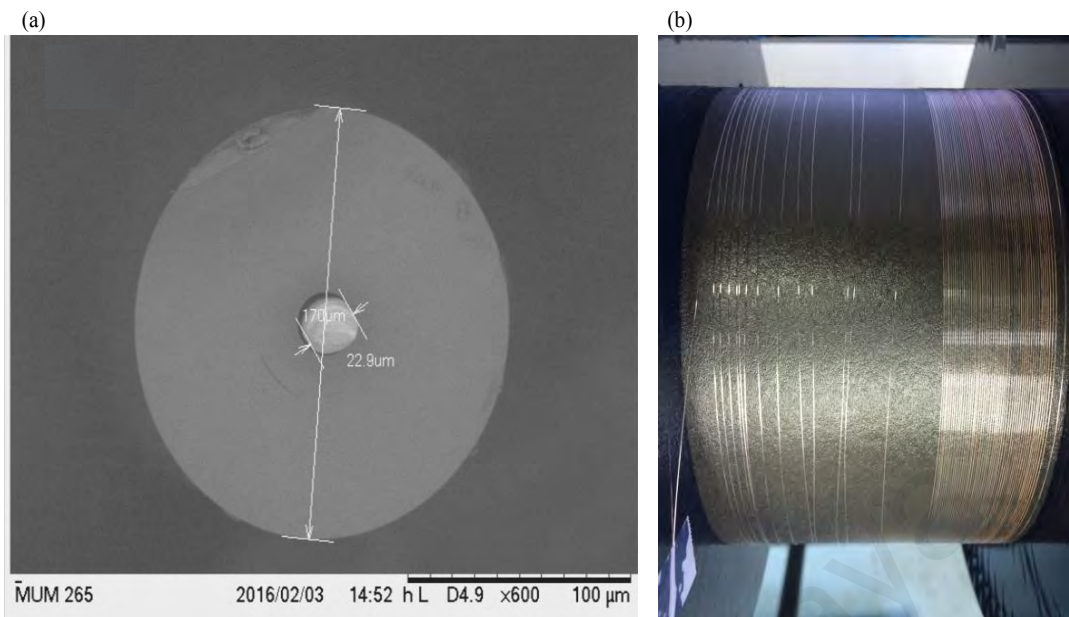


Figure 3.11: (a) SEM images for copper core optical fiber. The dimension of the fiber with 170µm cladding and 22.9 µm copper core (b) Fabricated copper-core optical fiber with more than 6 m continuous copper-in-glass, the longest reported so far.

3.5 Result and Discussions

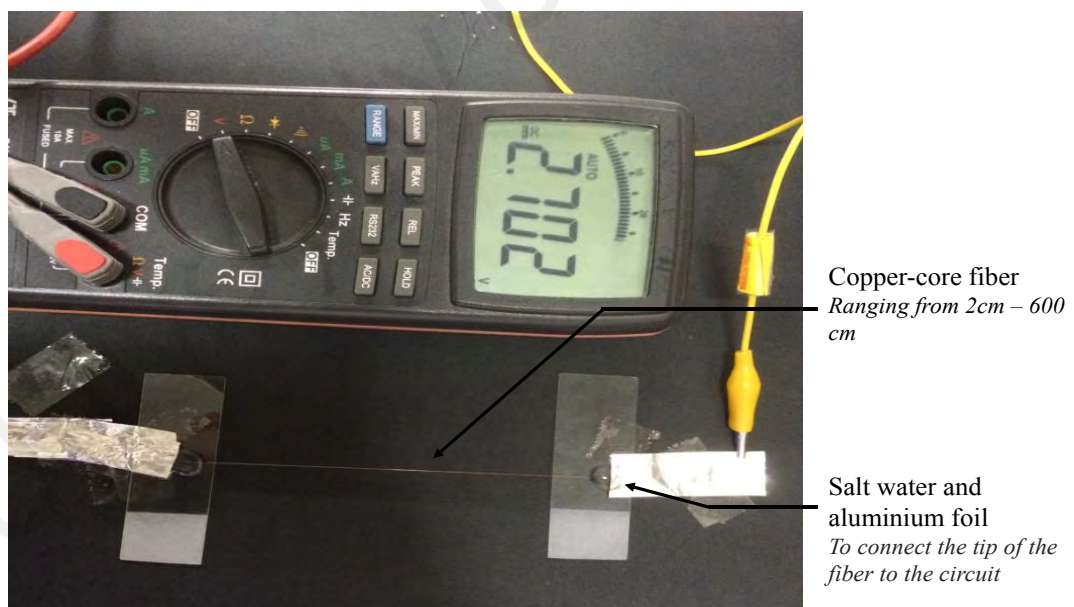


Figure 3.12: Conductivity and continuity test for copper-core optical fiber

Simple conductivity test was used to test the continuity of the copper-core fiber as illustrated in Figure 3.12. First, a small part of the glass is removed to expose the copper by using ceramic scribe. Then salt water is used to increase the surface contact of the copper wire. 60 samples of copper-core optical fiber ranging from 2 cm to 600 cm were

prepared to be tested its conductivity. Resistivity experiment and I-V characteristic were obtained to verify the continuity of copper-core optical fiber. The resistivity experiments is also conducted by varying the length from 50 cm to 600 cm and measure their resistance by connecting the exposed copper wire to a multimeter. For both experiments, we performed repeat measurements on multiple sets of identical fiber structure and as such, uncertainties with regards to these calculations are shown in the error bar¹ on the measured result.

The result shows that the resistance increases proportionally to fiber length. Interestingly, we successfully measured up to 600 cm of continuous copper fiber. The resistivity of each copper fiber sample is determined using equation 3.2.

$$R = \frac{\rho l}{A} \quad (3.2)$$

Where R is the resistance of the measured copper fiber, ρ is the resistivity, l is the length of the fabricated copper fiber and A is the cross-sectional area. From the Figure 3.13, by assuming the cross-sectional area of the fiber is circular, the resistivity of the fabricated copper fiber is $1.84 \times 10^{-8} \Omega\text{m}$. This value is close to the bulk resistivity valued of the copper metal at room temperature, which is $1.68 \times 10^{-8} \Omega\text{m}$.

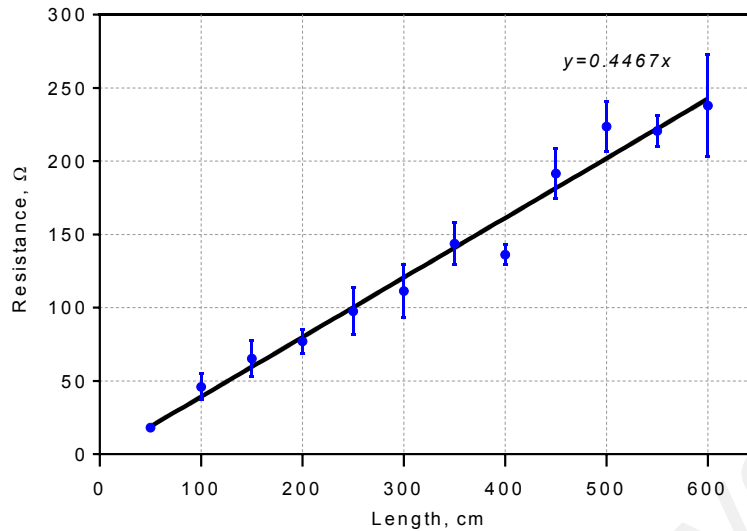


Figure 3.13: Resistance of each length of copper fiber

The I-V characteristic experiment is conducted to verify the resistance value of the copper fiber. We choose 30 cm, 80 cm and 110 cm length of the sample to be tested and connect the circuit as shown in Figure 3. 14. We could not have a longer sample since the value of the current obtained would be too small. The linear graph of the I-V characteristics of the copper fiber of 30 cm, 80 cm, and 110 cm is presented in Figure 3.13. The connection of the sample are connected in series and voltage is adjusted by using a rheostat and the circuit diagram is shown in the inset of Figure 3.14. The resistance of the single copper fiber is determined by the slopes of the lines. The 30 cm, 80 cm and 110 cm copper fiber showed a total resistance of 19.5 Ω, 56.5 Ω and 70.9 Ω respectively, which close to the resistance of the measured copper fiber in Figure 3.14¹.

¹
The error bars represent the standard deviation, σ of the data collected given by $\sigma = [(1/N) \sum_{i=1}^N (x_i - \bar{x})^2]^{1/2}$, where N is the number of measurements made, \bar{x} is the mean value of the measured data and $i=1 \dots N$.

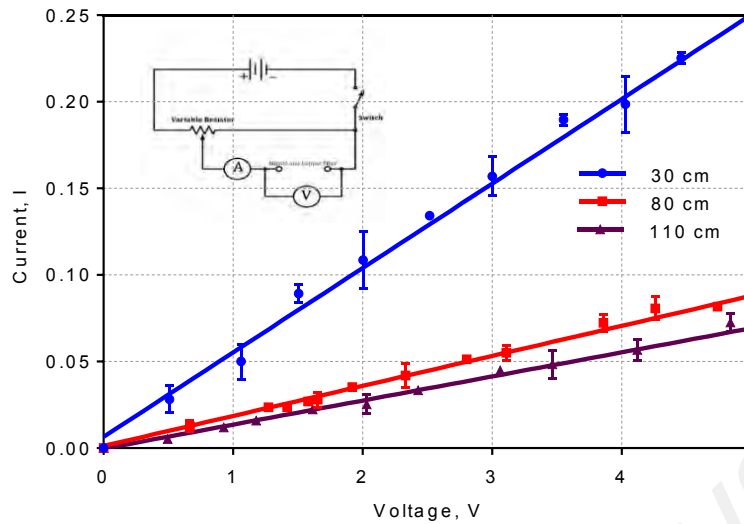


Figure 3.14: The I-V linear graphs for 30 cm, 80 cm, and 110 cm to evaluate the resistance of the sample. Inset is the circuit diagram of conductivity tests.

3.6 Summary

In this chapter, we demonstrated the successful fabrication of a long and continuous copper-core optical fiber. The fabrication method allows the production of small-scale copper wire encapsulated in silica as an alternative for planar substrate plasmon waveguide and also as optic-electric simultaneous transmission. Copper has a low melting temperature (1081 °C) than the silica's softening point (1900 °C). The temperature mismatch and surface tension that occur between the melted copper and the glass capillary resulted in copper globules which leads towards metal discontinuity/segmentation. Furthermore, this globules will diffuse into the glass capillary and it will cause the glass to crack and easy to break while the first stage drawing. This problem was circumvented by:

- Jacketing the capillary, resulting in thicker wall glass capillary to avoid diffusion and,
- Feeding the molten-copper by copper rod to fill the empty spaces after the copper starts to melt.

In conclusion, a new technique to fabricate a long and continuous copper-core optical fiber via a top-down approach have been demonstrated. The results showed that the fiber can be pulled up to 170 μm with 22.9 μm copper as a core. The continuity of the fabricated copper is tested by electrical measurements. The results proved that the copper was continuous up to 600 cm long. The resistivity value of the copper fiber was close to the bulk resistivity value of copper with 9.5% different percentage. This method can be successfully applied with a different metal such as gold or silver and it can be repeated to produce nanowire would be very useful in optical and electric application such as biosensor, nanowire laser, optical passive devices and metamaterial devices. At this point, knowledge we gained in this fabrication technique will be useful to fabricate copper-filled PCF which will be discussed in next chapter.

CHAPTER 4: COPPER-FILLED PHOTONIC CRYSTAL FIBER FOR POLARIZATION FILTER

Passive optical device such as filters, splitters, and couplers are crucial in optical communications. In this chapter, we design a wavelength-dependent polarization filter based on copper-filled photonic crystal fiber. The fabricated polarization filter is numerically analyzed and experimentally characterized to study its properties.

4.1 Couple-mode theory of metal-filled PCF.

In metal-filled PCFs, the light propagated in the fiber core eventually couple to the SPPs wave if the distance between the fiber core and metal is close enough. We could understand the coupling theory by viewing the metal-filled PCF as a directional coupler, which the PCF acting as a waveguide for core guided mode, and metal as a waveguide for SPPs mode. The new mode will evolve from the coupling of core-guided mode and SPP mode when the phase matching condition is satisfied. This condition will cause a high confinement loss as the energy from the core is absorbed by the surface of the metal. The coupled mode theory introduced by (Z. Zhang, Shi, Bian, & Lu, 2008) can further explain this phenomenon. When the coupling happens, the core-guided and SPP mode equations are given by:

$$\frac{dE_{core}}{dz} = i\beta_{core}E_{core} + i\kappa E_{SPP} \quad (4.1)$$

$$\frac{dE_{SPP}}{dz} = i\beta_{SPP}E_{SPP} + i\kappa E_{core} \quad (4.2)$$

where β_{core} and β_{SPP} are the propagation constants of core-guided and SPP mode, respectively. E_{core} and E_{SPP} are the mode fields of core-guided and SPP mode, respectively. κ and z are the coupling strength and the propagation length, respectively.

E_{core} and E_{SPP} can be described by $E_{core} = P \exp(i\beta z)$ and $E_{SPP} = Q \exp(i\beta z)$ and β is the propagation constant of the coupling mode. We substitute into eqs 4.1 and 4.2, thus

$$(\beta - \beta_{core})P - \kappa Q = 0 \quad (4.3)$$

$$(\beta - \beta_{SPP})P - \kappa Q = 0 \quad (4.4)$$

This equation can be represented as 2 X 2 matrix as follows:

$$\begin{bmatrix} \beta - \beta_{core} & -\kappa \\ -\kappa & \beta - \beta_{SPP} \end{bmatrix} \begin{bmatrix} P \\ Q \end{bmatrix} = \begin{bmatrix} 0 \\ 0 \end{bmatrix} \quad (4.5)$$

and by solving the determinant of $\begin{vmatrix} \beta - \beta_{core} & -\kappa \\ -\kappa & \beta - \beta_{SPP} \end{vmatrix} = 0$, the propagation constant of coupling mode β can be simplified as:

$$\beta_{\pm} = \beta_{ave} \pm \sqrt{\kappa^2 + \delta^2} \quad (4.6)$$

$$\text{where } \beta_{ave} = \frac{\beta_{core} + \beta_{spp}}{2}, \text{ and } \delta = \frac{\beta_{core} - \beta_{spp}}{2}.$$

Both core-guided and SPP modes are leaky modes, as their real parts of effective refractive index are lower than the background material (silica). Generally, for leaky modes, β_{core} and β_{SPP} are complex. Therefore, δ can be represented by $\delta = \delta_r + i\delta_i$. Moreover, the real parts of propagation constants of core-guided and SPP modes are equal ($\delta_r = 0$) when the phase matching condition is satisfied. Therefore, we can derive that $\delta^2 + \kappa^2 = -\delta_i^2 + \kappa^2$. When $\delta_i < \kappa$ the real parts for both β_+ and β_- are different but have equal imaginary parts. This condition is called complete couplings. Meanwhile, when $\delta_i > \kappa$, the real parts are equal but the imaginary parts are different. This condition

is called incomplete couplings. From the above discussion, since the coupling strength, κ is high, we assume the complete coupling of the core-guided mode of PCF and the SPP mode from the metal. The high value κ can be obtained by placing the metal and core close enough. The transmission characteristics for metal-filled PCF is strongly dependent on wavelength due to the coupling mechanism which only occurs at particular phase-matching wavelength also referred to as the resonant condition.

4.2 Design and Fabrication Process

Standard conventional fiber is normally with 125 μm in diameter and it is therefore advantageous for PCF to be fabricated to the same diameter for ease of cleaving and connecting to standard equipment. As the available silica tubes have a limited range of internal and outer diameters (IDs and ODs), the number of periods and wall thickness of the silica jacket must be appropriately selected for the final fiber diameter to reach ~ 125 μm without compromising the desired wave-guiding characteristics. Additionally, the ID to OD ratio of the capillaries must be chosen to closely match the air-hole diameter to pitch ratio (d/Λ) of the final structure while allowing for the slight collapse of the holes that will occur when the glass is passed through the furnace. The drawn capillaries must be closed at one end to retain the air-hole structure from completely collapsed.

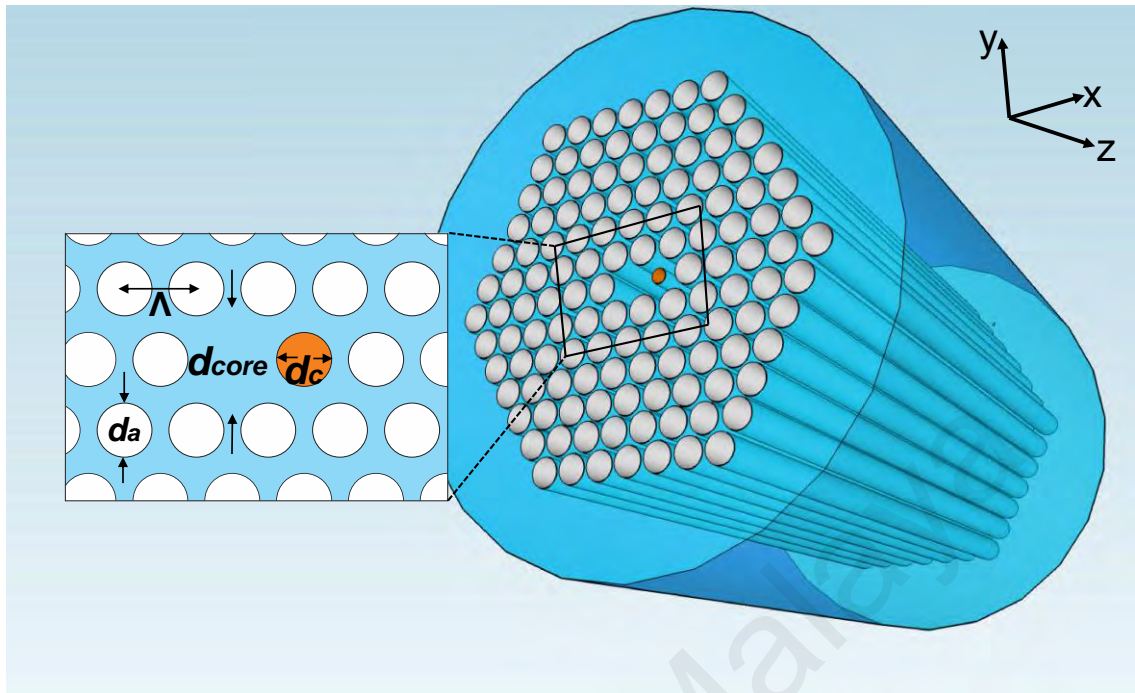


Figure 4.1: 3D-sketch and the cross-section of the design copper-filled PCF

Figure 4.1 depicts the proposed design for polarization filter based on copper-filled PCF. The copper wire is placed next to the solid core by removing one air hole. We design the PCF with six rings which can help to reduce leaky modes and propagation loss. PCFs has been successfully fabricated by a number of techniques include stack-and-draw (Knight, 1996), extrusion (Ravi Kanth Kumar, 2002) and sol-gel casting. Throughout this thesis, the fabrication of copper-filled PCF undergoes the traditional stack-and-draw technique, which offers clean, relatively fast, low-cost and flexible processes compared to extrusion and the sol-gel casting method (Knight, 1996). Usually, fabrication of PCF is divided into two stages: preform-to-cane fabrication and cane-to-fiber drawing due to the stability of the fabrication processes. The stack-and-draw technique begins with fabricating capillaries of required sizes with specific ID and OD. The capillaries of ~ 1.34 mm are drawn from commercially available preform tubes with an outer diameter of 25 mm and 17.5 mm inner diameter. A silica rod with same size also drawn from a rod preform as PCF's core. The copper cane was earlier prepared (discussed in Chapter 3) with 1/1.34 mm ID/OD before the stacking process. The preform construction in the

stack-and-draw technique consists of building up a stack of the same length of silica glass capillaries, silica rod, and a copper-cane, into triangular lattice using custom-made jigs. Capillaries are placed one row at a time. The solid core is placed in the center with copper-cane next to it. The process to draw fiber, canes, or preform is very similar and briefly discussed in the following subsection.

4.2.1 Capillaries Fabrication

Capillaries are the basic elements to build PCF preform produced by stacking method. To ensure a good structural uniformity of fabricated PCFs, quality of capillaries must be given a good attention as to produce less brittle PCF and avoid optical attenuation that arises from impurities. Capillaries for stacking are fabricated from high-grade silica preform tubes (Hareus Suprasil F300), drawn to nominal outer diameter of 1.34 mm. Smaller capillary sizes will result in the difficulty of keeping individual capillary in its respective lattice position during stacking process due to the presence of electrostatic. On the other hand, larger capillary diameters will lead to lesser rings of air holes which will increase the confinement loss. To control the size of capillary, preform feeding rate and tractor drawing speed are set according to the simplified mass conservation as introduced in Equation 3.1. It should be noted that this mathematical relation provides only a rough estimation of the capillary diameter. Careful adjustments of drawing speed and temperature are important to achieve the intended size.

The temperature of furnace is maintained between silica softening points, around 1950 °C to 2050°C. High-temperature increases the surface tension of silica and therefore reduces the ID/OD ratio, while the process does not follow the mass conservation equation. The outer diameter of the capillary is measured real-time using a laser diameter gauge.

4.2.2 Stacking Copper-Filled PCF's preform

Proper stacking is important to form the periodic cladding of PCF. Fabricated capillaries are cleaned and cut into ~40 cm lengths. The capillaries must be cleaned as contaminants such as dust and fingerprint will increase PCF scattering loss and also reduce mechanical strength. Dust residue inside the PCF preform will burn in high temperature and diffuse into the glass matrix which causes more losses and fragilities. Capillary surface is cleaned using iso-propyl alcohol while the inner wall of the capillaries is cleaned by ultrasonic bath. Single end of the capillaries is sealed by high-temperature butane-oxygen fuel hand-torch, to create high pressure inside the capillaries using fiber drawing which could prevent PCF holes from collapsing. We used a copper-cane with size of 1/1.34 mm which described in Chapter 3.

Custom-made hexagonal jigs are used as a template to stack capillaries into triangular lattice arrangement. Stacking is done with all sealed ends facing in one direction. By using the hexagonal jigs, capillaries are initially stacked in a suitable jacketing tube which is usually shorter than the capillaries for easy-handling. Voids at the six hexagonal sides are filled tightly (as shown in Figure 4.2 (a)) with packing rods of different sizes, which are cut shorter to avoid compressing and breaking of the bulging sealed ends. The central part of the PCF is replaced with a same size silica rod and a copper-cane is placed next to it. The stack of capillaries stacking (in hexagonal shape) is being held together by PTFE (polytetrafluoroethylene) tapes. Then, the hexagonal jigs are released before transferring the stacked capillaries into the longer preform tube.

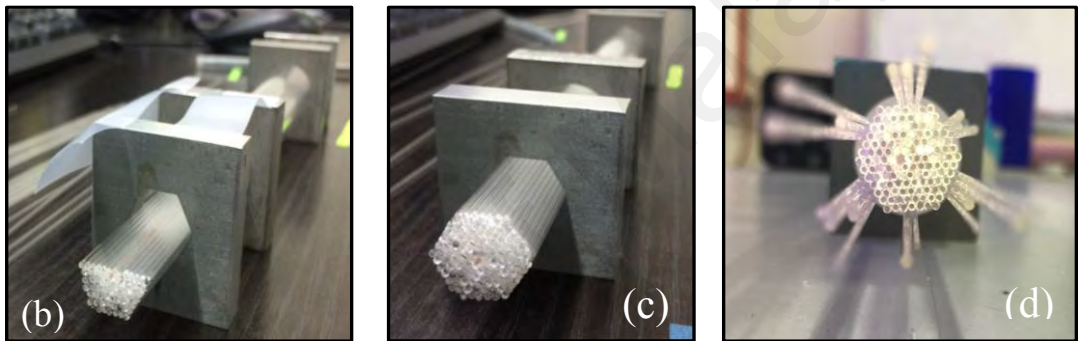
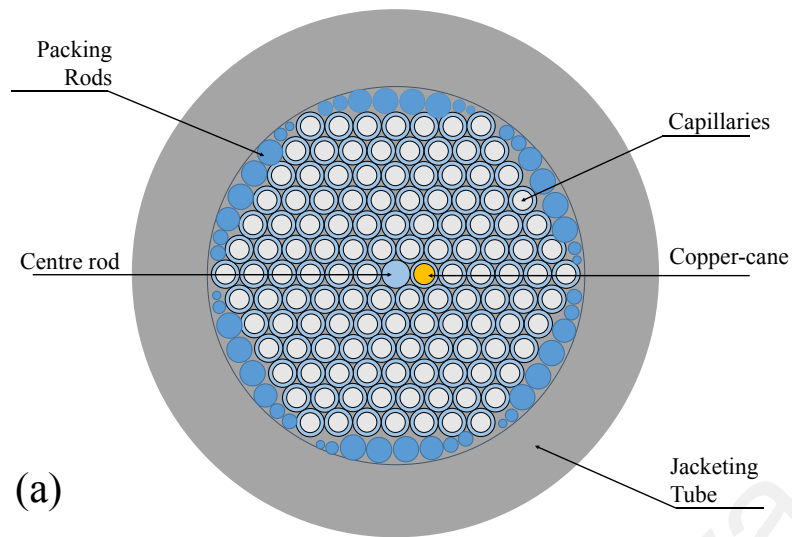


Figure 4.2: (a) Schematic diagram of cross-section of copper-filled PCF with packing rods. (b) Stacking the capillaries, solid rod and copper-cane. (c) Completed stacking in the hexagonal jig. (d) The complete stacking is transferred into silica tube with packing rods to fill the empty space.

Subsequently, the stacked structure is transferred slowly into a longer preform tube. The cross-section of copper-filled PCF preform stacking is illustrated in Figure 4.2. Figure 4.2 (b), (c) and (d) depicted a stacking process in hexagonal jig to form a triangular lattice arrangement.

4.2.3 Drawing Copper-Filled PCF's preform

We draw the preform (the completed stacking as shown in Figure 4.2 (c)) into a cane with a diameter of $\sim 1\text{-}2\text{ mm}^1$. Figure 4.3 depicts a cross-sectional view of the copper-filled PCF cane. The preform is mounted into the feeder chuck and fed into furnace. A vacuum of 15 kPa is applied as an aid to collapse of the holes and the capillaries and rods, called interstitial holes. The furnace temperature and drawing speeds are set to ensure the structure is maintained while the interstitial holes are completely closed under the vacuum. Temperature of the furnace is set in the range of $1950\text{ }^\circ\text{C} - 2050\text{ }^\circ\text{C}$. Temperature above $2050\text{ }^\circ\text{C}$ will result in complete collapse of air-holes or irregular hole shapes due to low viscosity and surface tension whereas temperature lower than $1950\text{ }^\circ\text{C}$ may lead to random cracks and interstitial holes. The initial feeding rate and drawing speed is set according to the mass conservation equation. A slow draw speed of 1 m/min is set to ensure complete collapse of interstitial holes and retaining a good structure. The cross-section surface of cane samples is observed under the microscope from time to time to ensure the formation of uniform lattice patterns.

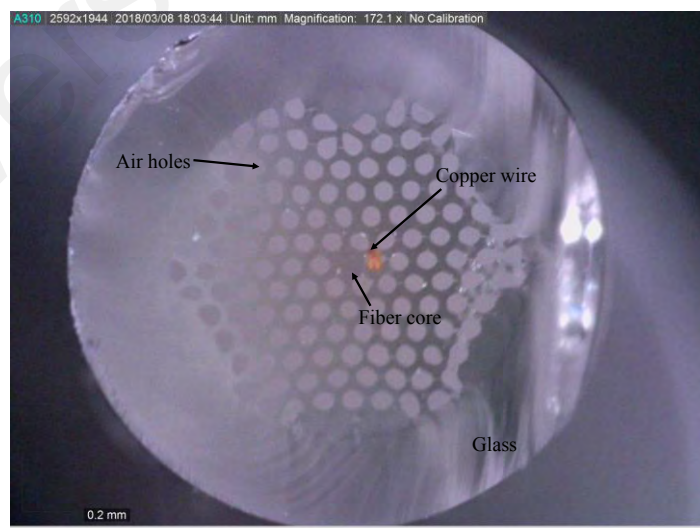


Figure 4.3: Fabricated copper-filled PCF cane measuring 1.7 mm diameter

¹ The best cane size is usually in this range. The smaller diameter will result in difficulty to convert into fiber format, whereas the larger diameter will result in bad fiber structure.

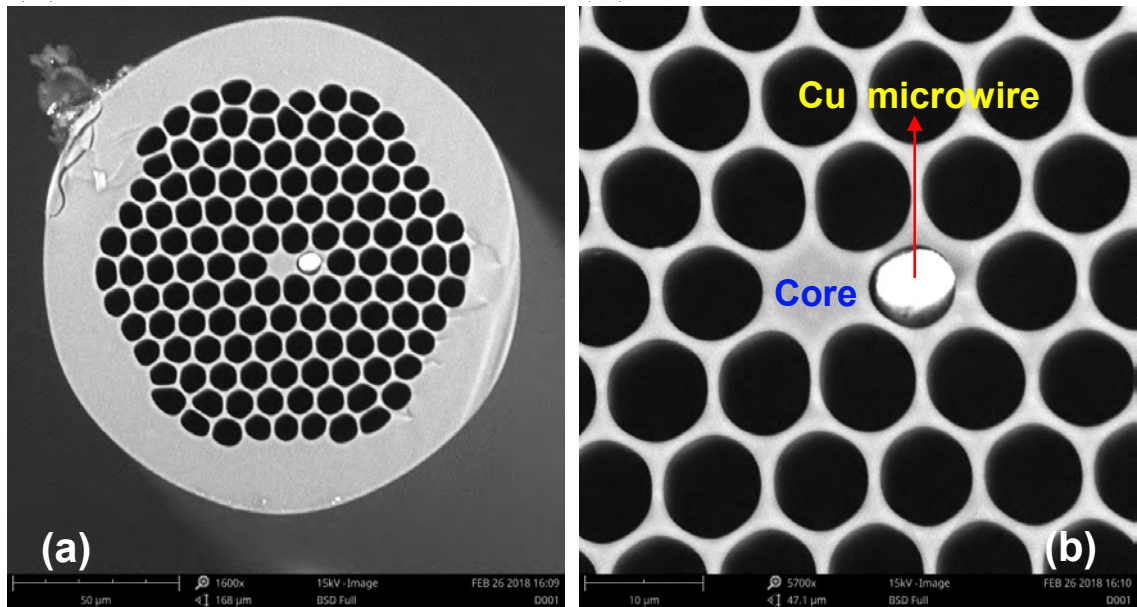


Figure 4.4: (a) SEM images for fabricated copper-filled PCF fiber. (b) Magnified view of the core area of the PCF indicating the presence of copper and a solid core.

Then, the cane undergoes the second stage drawing which converts it into fiber format. The size of the air holes can be controlled to some extent by applying pressure of 1-3 kPa. The fiber is pulled from the furnace at 1850 °C by capstan that also measures the fiber's tension. The value of the tension gives an indication of the effect of temperature on the fiber structure. A low tension reading usually below 50 g, which indicates high temperature and the holey structure might be collapsed. If the tension is too high usually more than 130 g, the fiber could break. The fibers are fragile if there are scratch marks on it. Thus, if long lengths of fiber are to be drawn, a protective polymer is coated to the fiber so that it can wind on the bobbins without breaking. After leaving the polymer cup, the coatings are then cured immediately by UV light. Figure 4.4 (a) and (b) illustrates the SEM image of copper-filled PCF fiber. Figure 4.5 illustrates a summary of copper-filled PCF fabrication process.

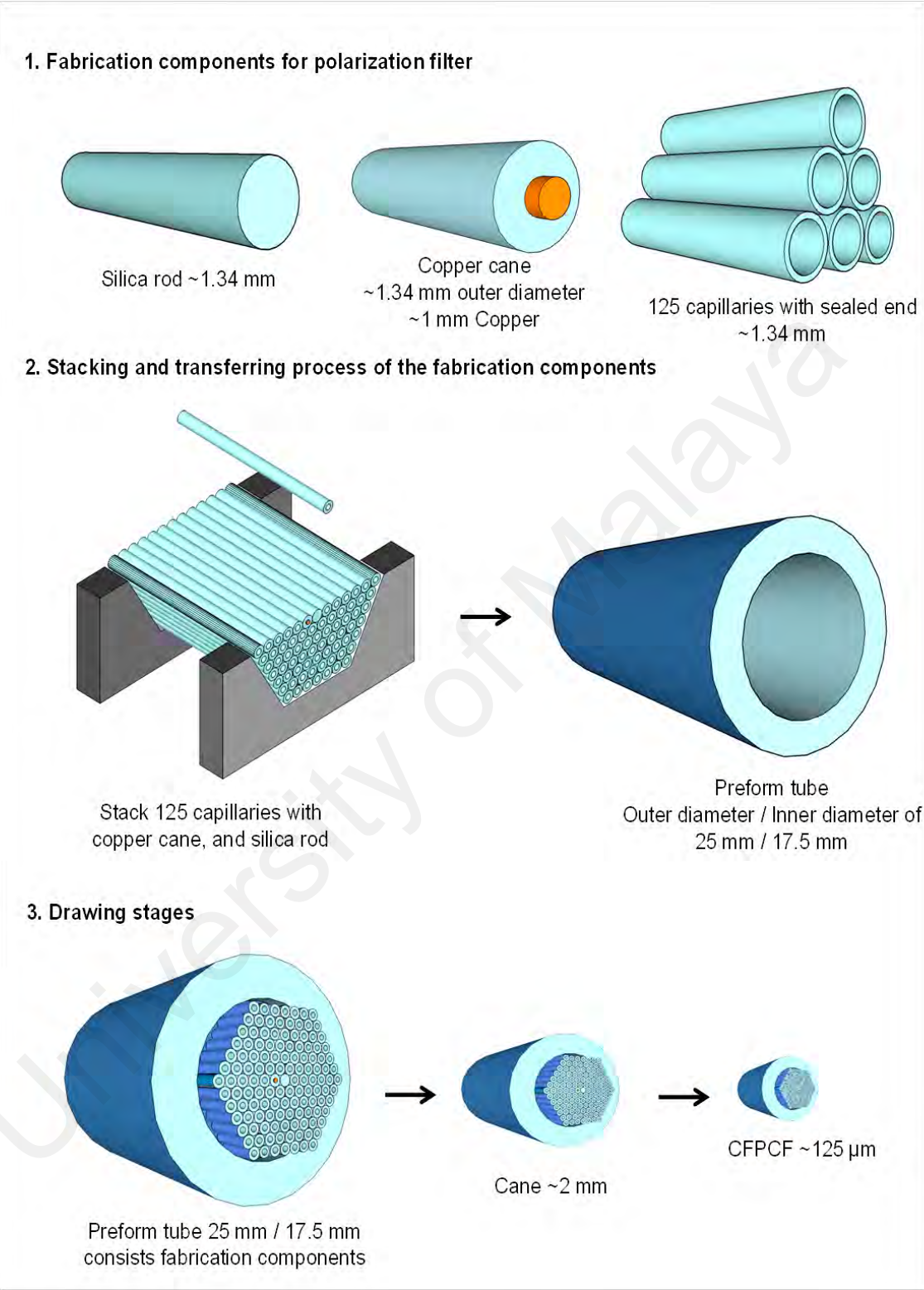


Figure 4.5: An illustration of copper-filled PCF (CFPCF) fabrication process

4.3 Numerical analysis and characterization of Copper-filled PCF (CFPCF)

The theoretical analysis of the dispersion relation of CFPCF is subjected to the material properties of silica and copper microwire. Consequently, this analysis was supported by using Equations 1 and 2. For silica, the dispersion relation was calculated by using the Sellmeier equation as represented in Equation 4.7 (Tatian, 1984).

$$n^2(\lambda) = 1 + \frac{B_1\lambda^2}{\lambda^2 - C_1} - \frac{B_2\lambda^2}{\lambda^2 - C_2} - \frac{B_3\lambda^2}{\lambda^2 - C_3} \quad (4.7)$$

n is the refractive index of silica and λ is the wavelength. The Sellmeier coefficients are as follows:

$$B_1 = 0.696163, B_2 = 0.4079426, B_3 = 0.897479401, C_1 = 4.67914826 \times 10^{-3} \mu\text{m}^2, C_2 = 1.35120631 \times 10^{-2} \mu\text{m}^2, \text{ and } C_3 = 97.9340035 \mu\text{m}^2 \text{ (Tatian, 1984)}$$

In addition, Equation 4.8 was used to analyze the dispersion relation for copper in terms of their dielectric constant. The dielectric constant of copper has been modeled using a Drude plus two critical points (D2CP) (Ando, Tuniz, Kobelke, & Schmidt, 2017):

$$\varepsilon = \varepsilon_\infty - \frac{1}{\lambda_p^2 (1/\lambda^2 + i/\gamma_p \gamma)} + \sum_{k=1}^2 \frac{A_k}{\lambda_k} \left[\frac{e^{i\phi_k}}{1/\lambda_k - 1/\lambda - i\gamma_k} + \frac{e^{-i\phi_k}}{1/\lambda_k + 1/\lambda + i\gamma_k} \right] \quad (4.8)$$

where λ_p is plasma wavelength, γ_p is the damping with the function of wavelengths, λ_j is the interband transition wavelength, γ_j is the transitions broadenings with the function of wavelengths, and A_j is the dimensionless critical point amplitudes. The corresponding coefficient values of the D2CP equation for permittivity (ε) of the copper were set according to the experimental data from Johnson and Christy as shown in Table 4.1

Table 4.1: Fit parameters for the D2CP model of permittivity for copper

Parameter (units)	Data from Johnson and Christy
ϵ_∞	4.5761
λ_p (nm)	138.24
γ_p (nm)	12790.84
A_1	3.5710
ϕ_1 (rad)	0.7204
λ_1 (nm)	252.22
γ_1 (nm)	490.9
A_2	0.6167
ϕ_2 (rad)	1.3077
λ_2 (nm)	560.97
γ_2 (nm)	4331.1

The corresponding values for the permittivity of copper have been fitted to the experimental data (Ando et al., 2017). The confinement loss (C_L) of the structure can be determined by considering the imaginary part of the effective refractive index (I_m) and is defined by [refs].

$$C_{L(x,y)}[dB/cm] = 8.686 k_0 \times I_m[n_{eff}] \times 10^4 \quad (4.9)$$

where $k_0 = 2\pi/\lambda$ is the wave propagation number in the free space and the wavelength λ is in micrometer. The core-guided mode will eventually match with that of SPP mode

which can result in resonance loss peak at a particular wavelength, known as resonance wavelength. The SEM image of the fabricated CFPCF was used for all simulation studies reported in this paper. The simulation study was carried out by using COMSOL Multiphysics 5.3 software, which is based on the finite element method (FEM). This was performed by extracting and importing the SEM image of the fabricated CFPCF into COMSOL geometry interface. Convergence tests were executed by optimizing the mesh size and perfectly matched layer (PML) thickness, which led to more accurate results. We used the built-in circular PML with 10 μm thickness, which is added in the outer region of structure. The meshing is divided into three regions, which are the PML layer, cladding region, and core region (including the first two air-hole rings), as shown in Figure 4.6. The core region is the densest area compared to the PML and the cladding region, which leads to more accurate computational analysis. The maximum mesh element size of the core is 0.2 μm while the cladding and PML regions' mesh sizes are 0.8 μm and 1.6 μm , respectively. The full structure is meshed with 1,221,576 number of smallest elements.

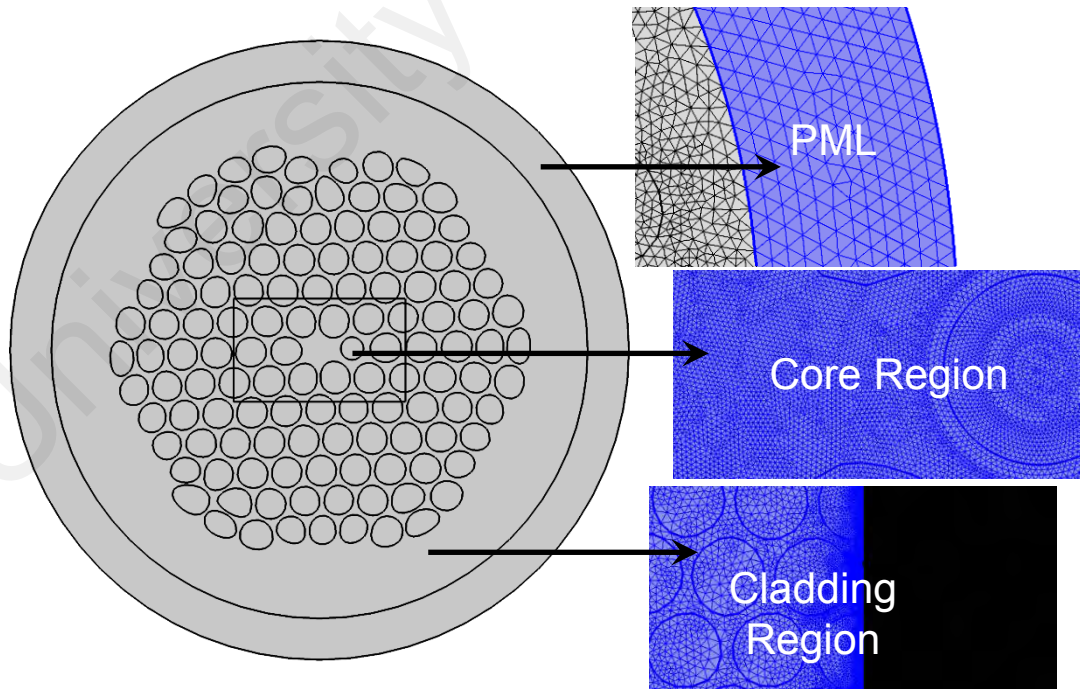


Figure 4.6: The extracted SEM image from COMSOL with meshing structure for PML, core, and cladding region.

4.4 Experimental Setup

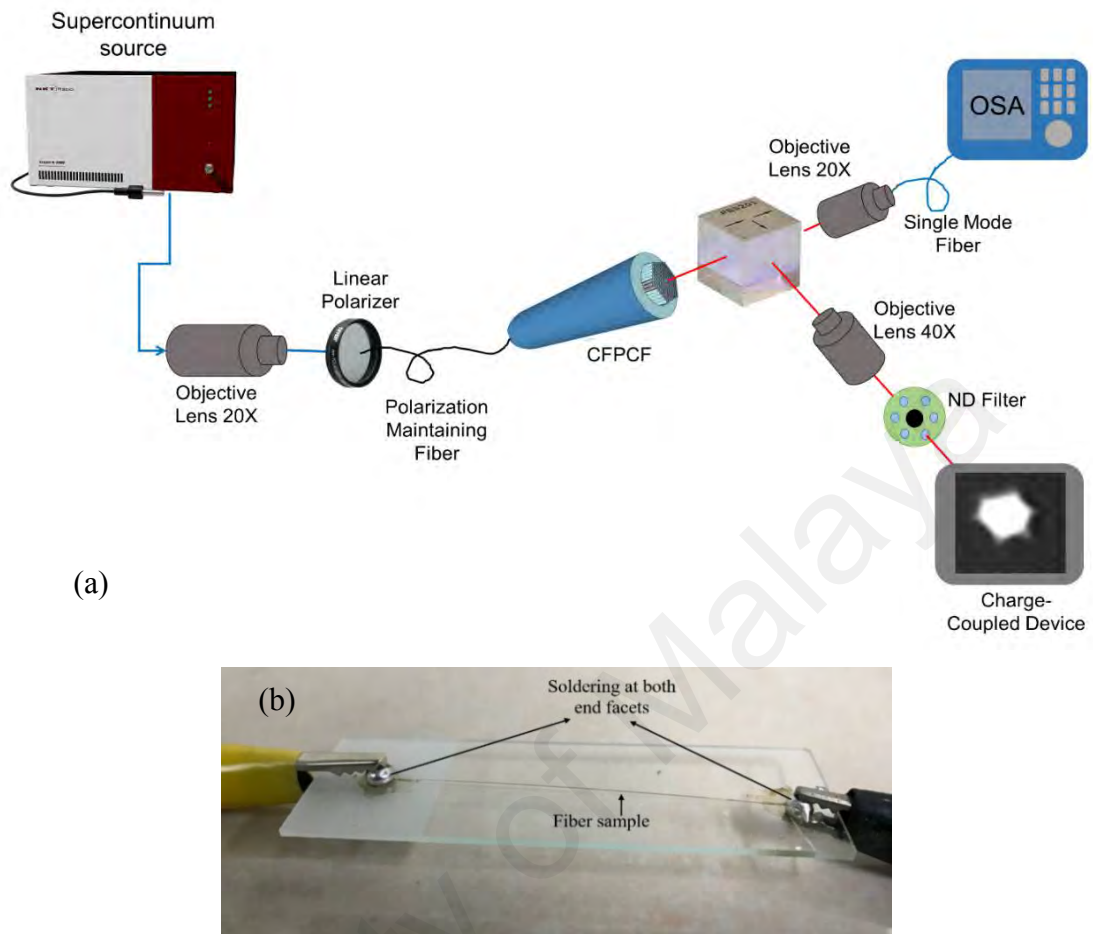


Figure 4.7: (a) Experimental setup to measure transmission spectrum and CCD imaging. (b) Connecting both end facets by metal-soldering for continuity tests.

The experimental setup to measure the transmission spectrum of the CFPCF was exhibited in Figure 4.7 (a). A supercontinuum source (SuperK, NKT Photonics) was used as the input light source. Efficient light coupling was ensured by using a 20 \times objective lens. Controlled polarization of input light was achieved by employing a linear polarizer followed by a polarization maintaining fiber (PMF). The output light from the CFPCF was split into two directions by using a polarization beam splitter. A perpendicularly directed light beam reached the charge-coupled device (CCD) (MicronViewer 7290A, Electrophysics) camera via a 40 \times objective lens and neutral-density (ND) filter while a parallel beam was directed to an optical spectrum analyzer (OSA). The ND filter before the CCD was used to control the intensity of light. We ensured an upward orientation of the CFPCF during all measurements by checking its mode image on the CCD camera and

the transmission spectrum was recorded by using the OSA. The continuity of the copper has been tested using conductivity test. The method for the conductivity test is the same as shown in Section 3.4.

4.5 Results and Discussion

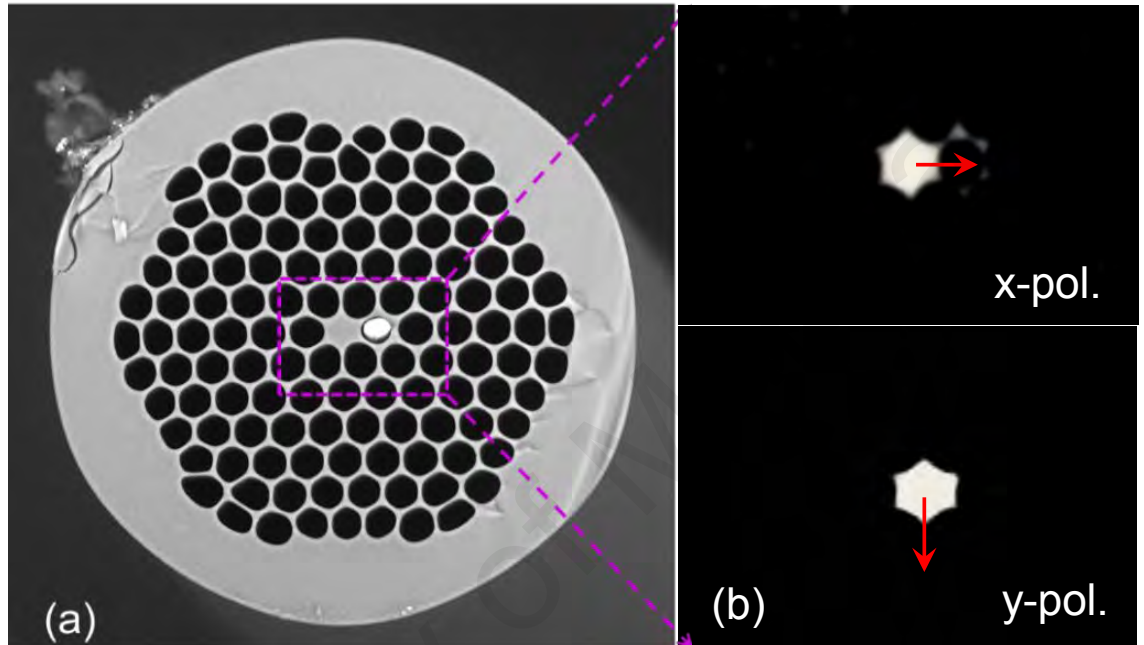


Figure 4.8: (a) SEM image of the fabricated CFPCF, and (b) mode profile image taken from the CCD for x- and y-polarized modes

The SEM image of the CFPCF and the mode image was taken from the CCD camera as depicted in Figure 4.8 (a) and (b). We ensured the correct orientation of the CFPCF throughout the measurement of the transmission spectrum.

The dispersion relation and the modal analysis for different orders of SPP modes and the core-guided mode of the CFPCF in x-polarization (horizontally polarized) and y-polarization (vertically polarized) are depicted in Figure 4.9. The effective refractive index of the second-order SPP mode is much higher than the effective refractive index of the core-guided mode. As a result, the second-order SPP mode would match to the core-guided mode at a wavelength larger than 2000 nm. As shown in Figure 4.9 (a), the phase-matching phenomenon occurred when the effective refractive index of the third-order

SPP mode crossed the effective refractive index of the x- and y-polarizations core-guided mode at the wavelengths of 1790 and 1890 nm, respectively. During this phase-matching phenomenon, the resonance loss of x- and y-polarizations reached a maximum with 37.0 dB/cm at 1790 and 19.7 dB/cm at 1890 nm, respectively, as illustrated in Figure 4.9 (b). The electric field distributions of the respective guiding modes of x- and y-polarizations at the phase matching phenomenon were portrayed in Figure 4.9 (c) and 4.9(d).

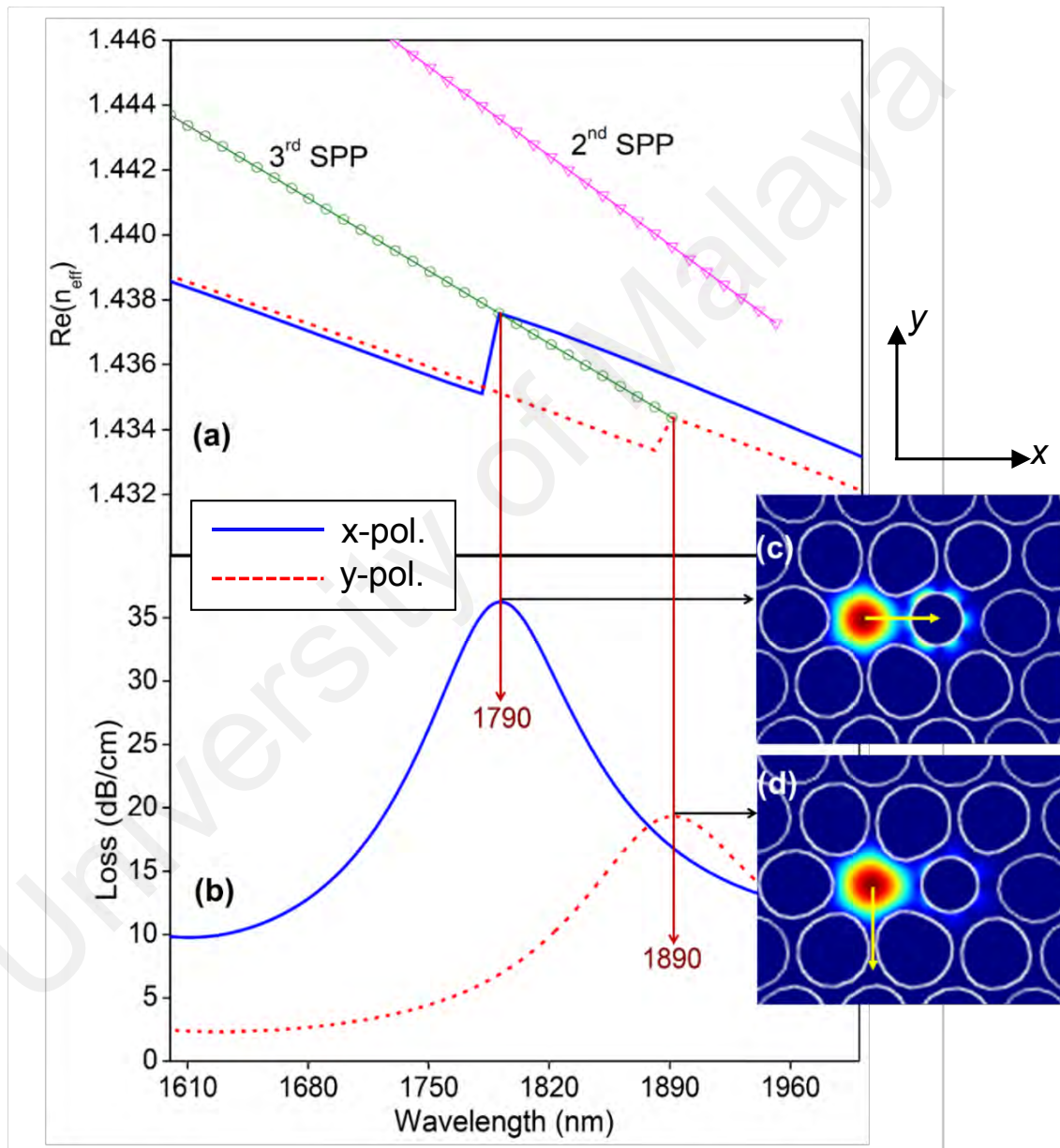


Figure 4.9: Simulated results for (a) dispersion relation of the CFPCF polarization filter. (b) Loss spectrum for CFPCF for x- and y-polarizations. Electric field distribution of the fundamental mode of (c) x-polarization at 1790 nm and (d) y-polarization at 1890 nm.

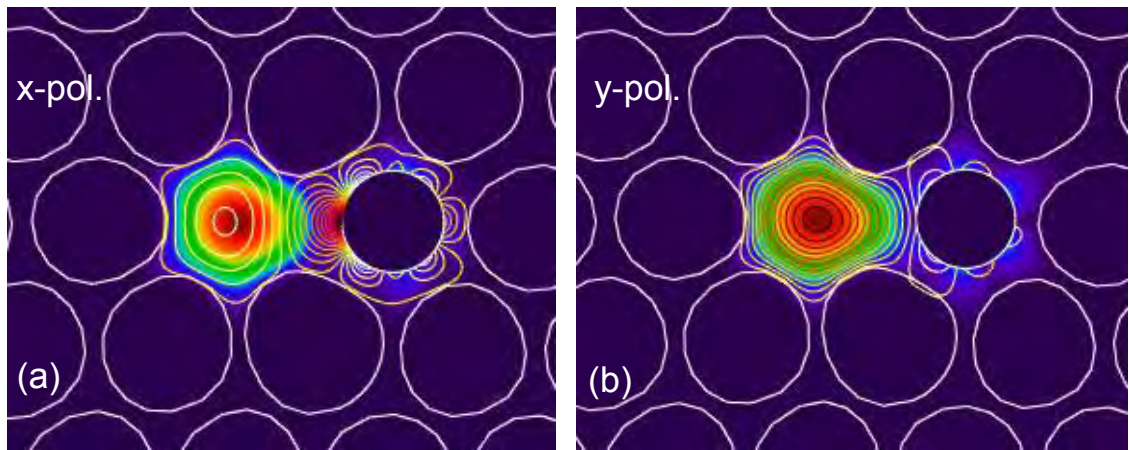


Figure 4.10: Contour line of transverse electric field vector distribution of the (a) x-polarization, (b) y-polarization, representing the coupling strength of the phase matching phenomena.

In addition, transverse electric field vector distribution of the x-polarization coupling of the core-guided and SPP modes shows that the lobe fields of the SPP mode are strongly attracted to core-guided lobe fields, as shown Figure 4.10 (a). In contrast, Figure 4.10 (b) exhibits the loss in the lobe fields of SPP modes toward y-polarization core-guided lobe fields. This is because of the metal position dependency where the position of the copper wire was horizontally placed next to the CFPCF's core. These indicate higher resonance loss for the x-polarized mode than y-polarized. The same observation was also reported elsewhere (Shi et al., 2015; Tyagi et al., 2010).

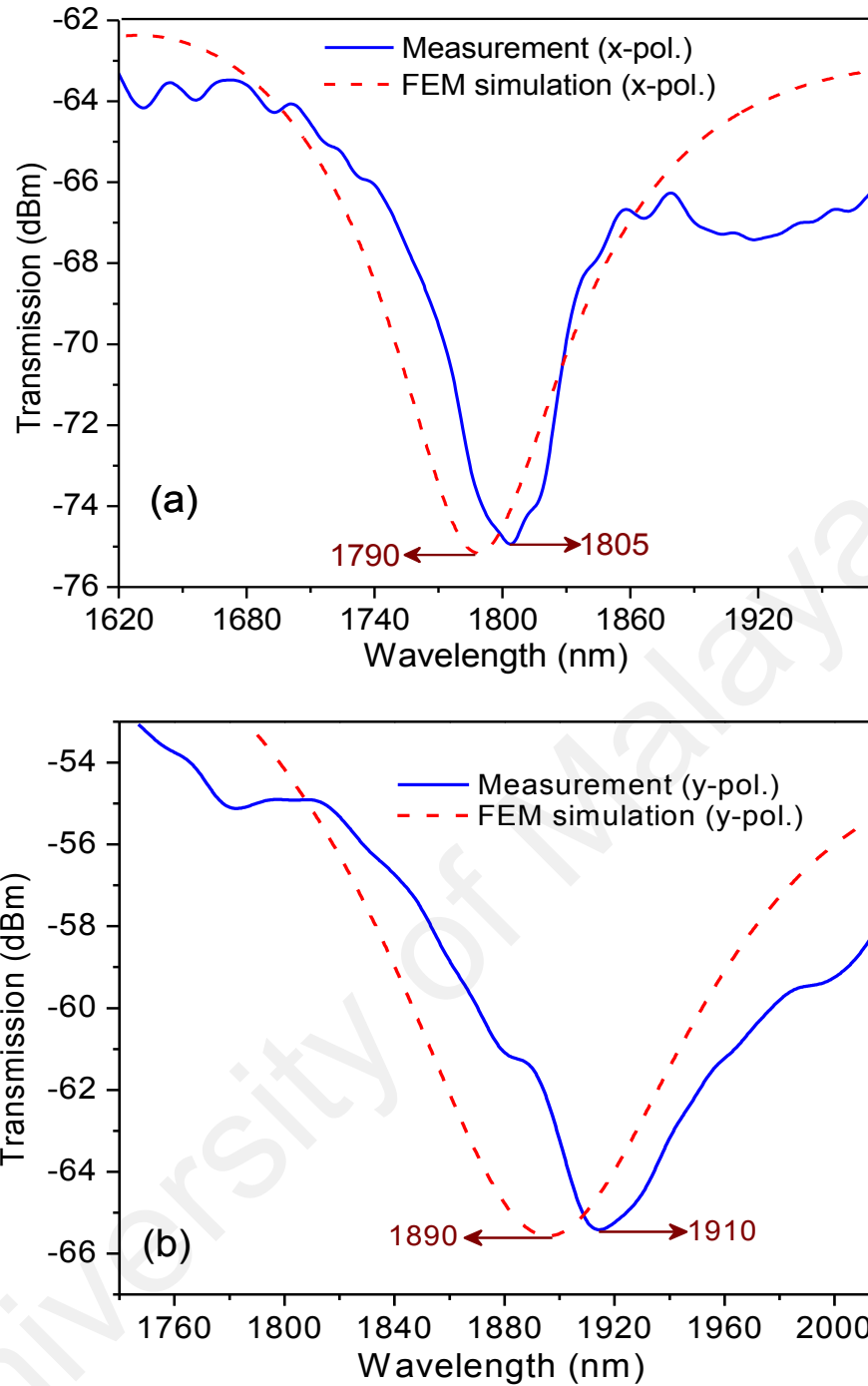


Figure 4.11: Transmission spectra of measurement and FEM simulation: (a) x-polarization, (b) y-polarization.

Figure 4.11 highlights the transmission spectra of x- and y-polarizations measured via a broadband source by using the OSA. Both measured transmission spectra (continuous line in blue color) have a resonance dip which corresponds to the phase-matching condition between the core-guided mode and the third SPP mode at the respective

wavelengths of 1805 and 1910 nm. On the other hand, the transmission spectra of FEM simulation of x- and y-polarizations were observed at 1790 and 1890 nm, respectively. It is found that both measurements of resonance dips are shifted from their FEM simulations by 15 and 20 nm to a longer wavelength. This can be explained due to the thermal shrinkage of the metal during the fabrication, which led to form air gaps between the copper and the (M. A. Schmidt et al., 2008).

Cross talk is one of the key elements used to control and limit the undesirable polarized modes during the fabrication of a polarization filter. Cross talk also characterizes the quality of transmission by defining its ability to eliminate the undesirable polarized mode [17]. The cross talk is developed by Beer–Lambert laws [29] in which it can be simplified as a function of the fiber length as given in Equation 4.10

$$\text{Crosstalk [dB]} = 20 \log_{10} [\exp((CL_x - CL_y)L)] \quad (4.10)$$

where L , CL_x , and CL_y are the length of the fiber and loss of x- and y-polarization modes, respectively. We have used the electromagnetic wave frequency domain for modal analysis based on the FEM to calculate cross talk which involves the imaginary part of the effective refractive index. Furthermore, the available optical bandwidth of the CFPCF can be measured as the wavelength encompasses within the cross-talk line below -30 dB (Dou, Jing, Li, Liu, & Bian, 2016).

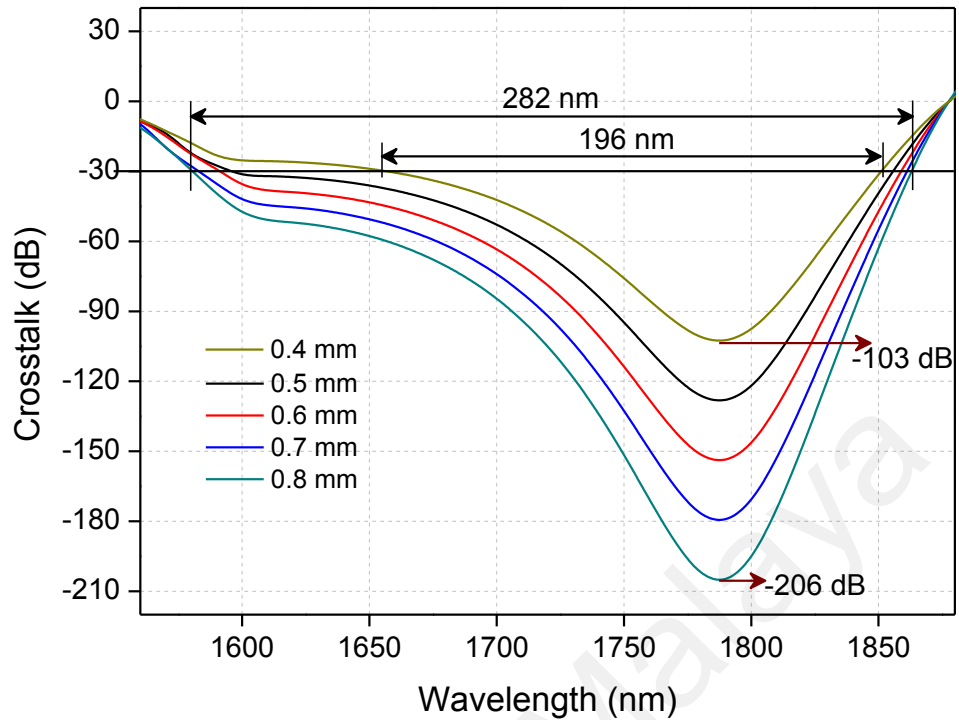


Figure 4.12: Calculated crosstalk for five different lengths of CFPCF polarization filter

Figure 4.12 presents the calculated cross talk of the CFPCF in different lengths as a function of wavelength. The cross-talk dip appears at the resonance wavelength of 1790 nm. As the fiber length increases, the degree of the cross talk increases too. The magnitude of cross talk for the shortest fiber length of 0.4 mm achieved is -103 dB, while the magnitude of cross talk reaches up to -206 dB for a 0.8 mm long CFPCF at the wavelength of 1790 nm. It is crucial for the cross talk to be sufficiently high as a polarization filter to eliminate the unwanted polarized mode and also retains a large optical bandwidth. The bandwidth of the 0.8 mm CFPCF is the widest, which is 282 nm (1580– 1862 nm). Besides the confinement loss and the cross-talk value, the insertion loss (IL) is one of the key performances for the polarization filter. The IL can be calculated by considering the loss value of the wanted polarization mode. The IL of a filter can be calculated using Equation 4.11 [refs].

$$IL_{x,y} [dB] = -10 \log_{10} \left(\frac{P_{out(x,y)}}{P_{in(x,y)}} \right) \quad (4.10)$$

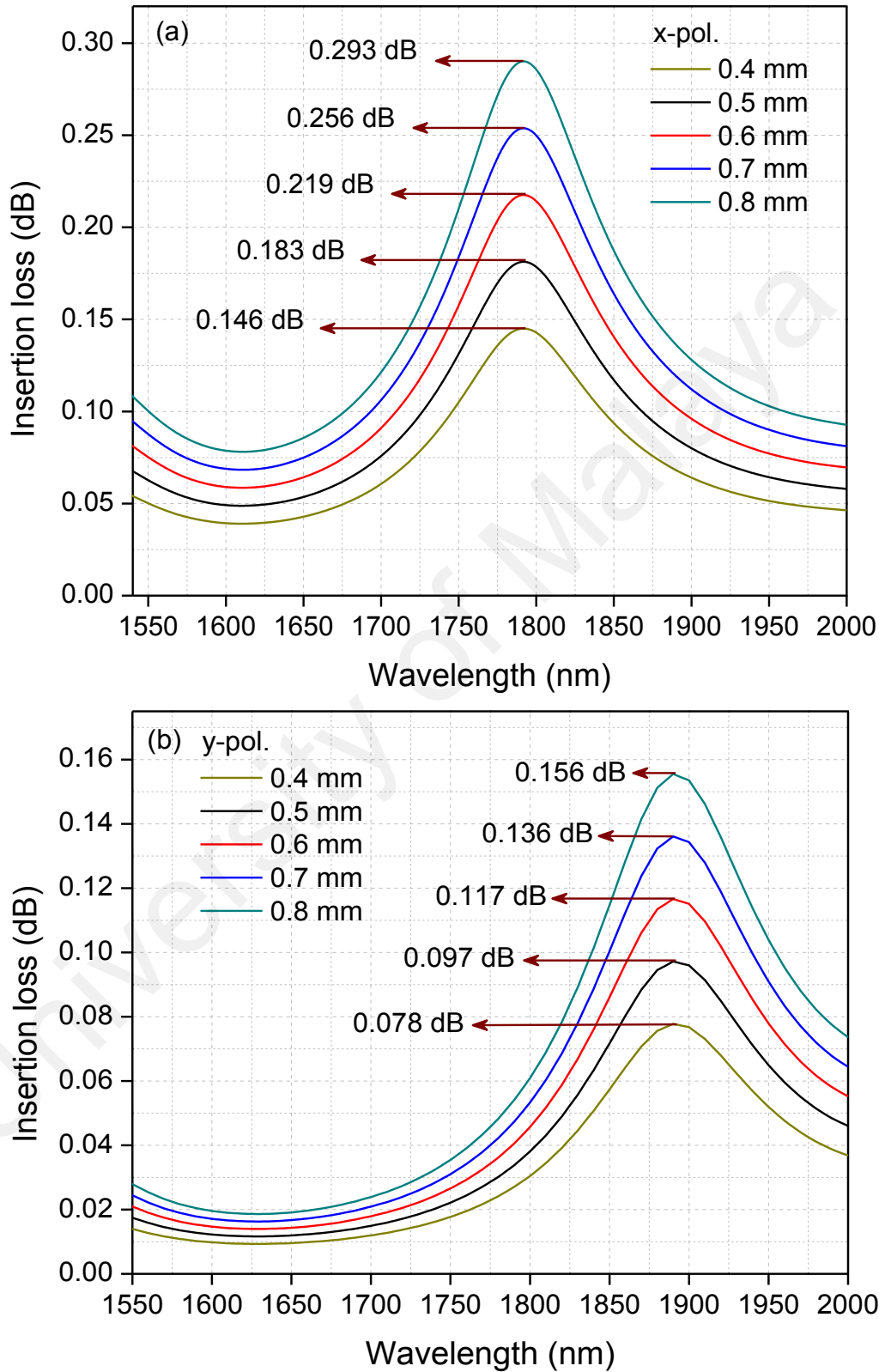


Figure 4.13: IL with varying fiber length for (a) x-polarization, (b) y-polarization.

The ILs for both x- and y-polarizations by varying the fiber length are depicted in Fig. 10. As shown in Figure 4.13 (a), the IL for x-polarization has the highest peak at the resonance wavelength of 1790 nm with 0.8 mm fiber length, which gives 0.293 dB. Furthermore, at the y-polarized resonance wavelength (1890 nm), the IL of 0.156 dB is achieved with the 0.8 mm fiber length. It is noticeable that the IL for both x- and y-polarized modes is relatively low around 0.10 dB from the 1550 to 1700 nm wavelength. In general, the IL is increased when the length increased. These characteristics mentioned above would make the fabricated CFPCFs as the potential candidate for a polarization filter device.

4.5.1 Impact of copper-wire diameter, d_c on characteristics of polarization filter.

The characteristics of the polarization filter, such as the magnitude of the resonance loss, cross talk, and the optical bandwidth, can easily be altered by changing the diameter of the copper wire (d_c). Here, we considered phase matching of the third-order SPP mode with the core-guided mode to understand the impact of d_c on the polarization characteristics. The second-order's resonance coupling might be matched at the wavelength longer than 2000 nm. Four different d_c values of 0.4λ , 0.5λ , 0.6λ , and 0.7λ μm have been tested to understand the trend of resonance loss. As shown in Figure 4.14, by increasing the d_c value, the magnitude of the resonance loss increases, while the resonance wavelength shifts toward the longer wavelengths. This trend is observed in both x- and y polarizations, as depicted in Figure 4.14 (a) and 4.15 (b), respectively.

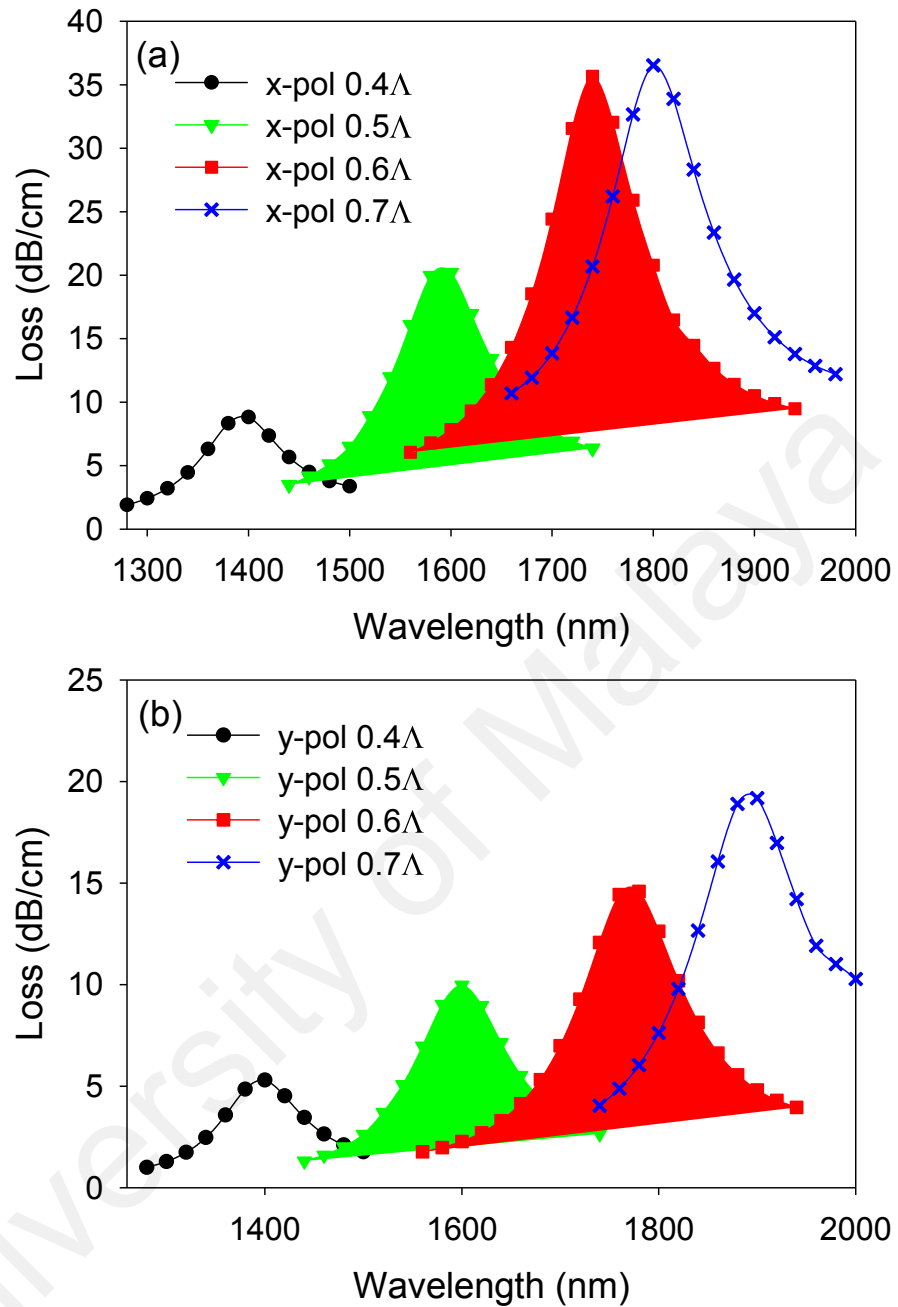


Figure 4.14: Resonance loss for four different sizes of the copper wire (a) x-polarization (b) y-polarization.

The results show by increasing the copper core diameter in the CFPCF from 0.4Λ , 0.5Λ , 0.6Λ , and 0.7Λ μm , the resonance losses of x-polarization are found to be 8.8, 20.2, 35.7, and 37 dB/cm, respectively. The corresponding resonance losses of y-polarization are observed to be 5.8, 11.2, 16.8, and 19.7 dB/cm. The dependency of the resonance wavelength to the diameter of the copper wire d_c is depicted in Fig. 4.13. The CFPCF can

filter at communication wavelengths of 1310 and 1550 nm by choosing d_c to be 0.32Λ and 0.48Λ , respectively.

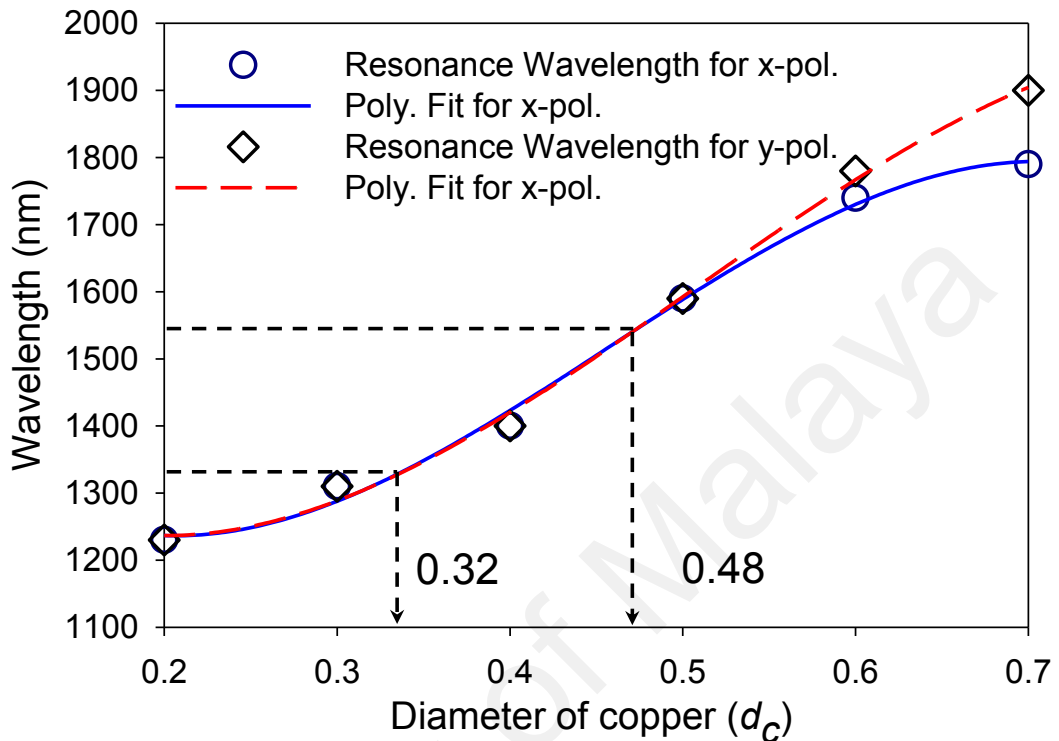


Figure 4.15: Resonance wavelength for different diameter of copper wire

The amounts of crosstalk for different d_c are shown in Fig. 13 for a fixed CFPCF length of 0.8 mm. The results show that the CFPCF with d_c of 0.4Λ , 0.5Λ , 0.6Λ , and 0.7Λ μm can filter the polarized light at the central wavelengths of 1390, 1582, 1733, and 1790 nm with cross-talk values of -40.0 , -88.8 , -163.4 , and -206.0 dB and bandwidths of 89, 235, 260, and 282 nm, respectively, as summarized in Table 2.

¹Polynomial fit of resonant wavelength with third order polynomial. The equation given is $Y=B0 + B1*(X - MeanX) + B2*((X - MeanX)^2) + B3*((X - MeanX)^3)$ with $B0=0.01529, B1=0.1634, B2=0.3984, B3=3.024, X=6, MeanX=0.45$

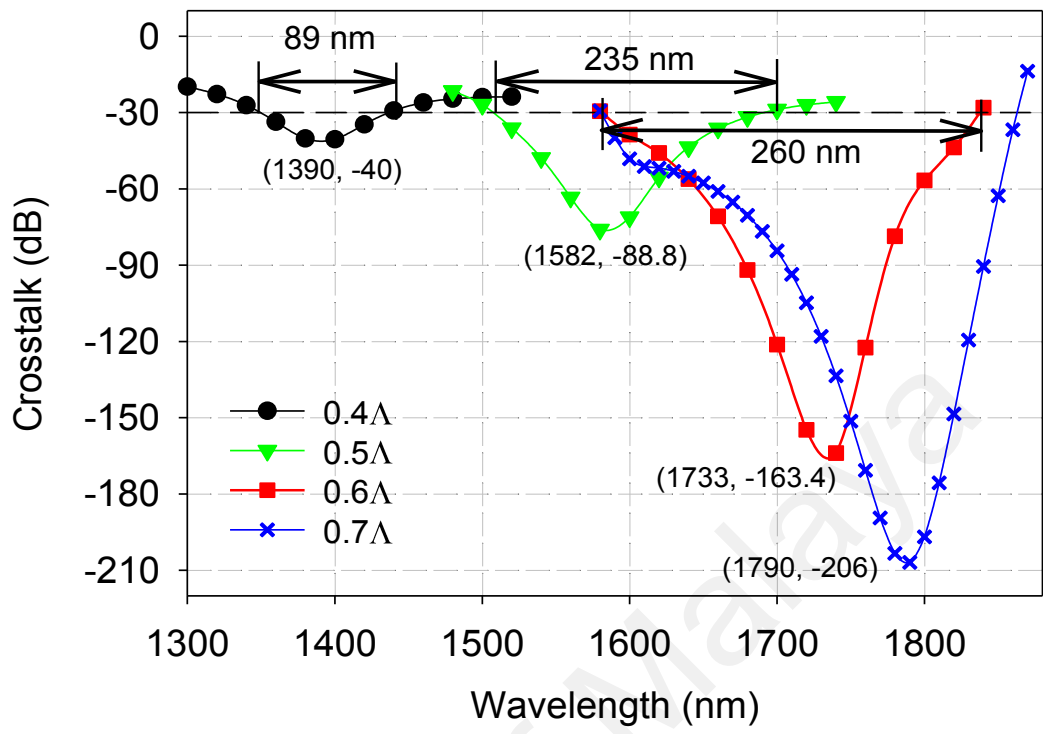


Table 4.2: Polarization Characteristics with respect to the Diameter of Copper Wire (d_c)

Copper diameter, d_c (μm)	Loss in x-polarized (dB/cm)	Loss in y-polarized (dB/cm)	Operating wavelength x-polarized (nm)	Operating wavelength y-polarized (nm)	Crosstalk lower (dB)	Bandwidth (nm)
0.4Λ	8.3	5.8	1390	1390	-40	89
0.5Λ	20.2	10.0	1582	1582	-88.8	235
0.6Λ	35.7	14.6	1732	1790	-163.4	260
0.7Λ	37.0	19.7	1790	1890	-206.0	282

4.6 Summary

In summary, a simple structure of a polarization filter based on CFPCF have been designed and fabricated. The CFPCF is fabricated by following the conventional stack-and-draw method. The resonance loss of the fabricated fiber is measured for x- and y-polarizations, which are 37.0 and 19.7 dB/cm, respectively. The measured transmission spectrum shows a good agreement with the simulated transmission of x- and y-polarizations with slight redshift in wavelength. Other characteristics of the CFPCF as polarization filter are numerically analyzed by using the SEM image of the fabricated fiber. The results show that the cross talk between x- and y-polarizations can be reduced by increasing the fiber length and/or the copper wire diameters. In the former approach, the central wavelength of the filter remains unchanged by increasing the fiber length, while in the latter method, the central wavelength shifts toward longer wavelengths as the copper diameter increases. For resonance loss and filter bandwidth, both of them are relatively increased by increasing the fiber length and/or copper diameter. It is shown that for a fixed length of 0.8 mm, by varying the diameter of the copper wire from 0.4 Λ to 0.7 Λ μm , the resonance wavelength can be tuned from 1390 to 1890 nm with a cross talk of -40 to -206 dB and bandwidth of 89 to 282 nm, respectively. Under the same

circumstances, the insertion loss is relatively low for both polarizations. For x-polarization, the IL is ranging from 0.071 to 0.293 dB, whereas for y-polarization, the IL is ranging from 0.042 to 0.156 dB. Also, the CFPCF polarization filter can work in the communication bands of 1310 and 1550 nm by setting the copper diameter at 0.32Λ and 0.48Λ μm , respectively. The results suggest that the proposed CFPCF would be a suitable candidate for designing polarization filters. Furthermore, our CFPCF fabrication technique may open a new way to selectively fill the metallic wires inside microstructured fibers, which paves a broad range of applications. In Chapter 5, the characteristics of polarization splitter based on copper-filled in dual-core photonic crystal fiber will be introduced.

CHAPTER 5: COPPER-FILLED PHOTONIC CRYSTAL FIBER FOR POLARIZATION SPLITTER

In this chapter, we will introduce the wavelength-dependent polarization splitter based on copper-filled dual-core photonic crystal fiber. We demonstrate a dual-core PCF with a copper-core placed between the PCF's cores. A brief description of numerical modeling using the plane-wave expansion method (PWEM) and finite element method (FEM) is given. We used a commercially available software package COMSOL Multiphysics 5.2 to simulate the copper-filled dual-core PCF. We then present the properties of the copper-filled dual-core PCF as a polarization splitter.

5.1 Polarization Splitter

Polarization splitter is one of the most far-reaching passive optical devices in a modern optical communication system. It can split incoming two orthogonally polarized light into two- polarization states (x- and y- polarized) after an optimized propagating length. Traditionally, polarization splitters have been fabricated by conventional fibers and one major disadvantage is their long coupling length (C. W. Wu, Wu, & Chang, 1995). For example, the length of polarization splitters reported in (Peng, Tjugiarto, & Chu, 1990) and (Miliou, Srivastava, & Ramaswamy, 1993) is 262 mm and 25 mm, respectively. Thus, PCF provides a new approach to design a shorter polarization splitter owing to its design flexibility and their unique properties.

There is a vast amount of literature on the application of dual-core PCFs in polarization splitters. The solid cores are placed adjacently close to each other into a single PCF as optical fiber couplers due to its flexible design, huge index contrast, and compactness in size (Fan et al., 2016; L.-h. Jiang et al., 2016; L. Jiang, Zheng, Hou, Zheng, Peng, et al., 2015; Khaleque et al., 2015; Q. Liu et al., 2015; Sun et al., 2015). Nonetheless, the coupling length of the fiber coupler is commonly long since it is strongly dependent on

the fiber structure. Hence, this will result in a low coupling efficiency which leads to many communication problems such as intermodal dispersion in the transmission which could result in the propagation of short pulses in a dual-core optical fiber (Chiang et al., 1997). Thus, the metal wire is introduced in the center between the dual-cores to improve the directional power transfer (L. Chen et al., 2014; H. Jiang et al., 2014; Sun et al., 2013). As discussed in Chapter 4, the phase matching condition is met when the guided core mode coupled with the surface plasmon modes at a particular wavelength. The resonant coupling between the surface plasmon modes by the metal wire and the fiber core-guided modes can be used to enhance the performance of dual-core fiber coupler by an order of magnitude reduction in coupling length. The metal wire acts as a bridge to transfer the energy between cores. This could enhance the coupling efficiency which implies potential applications in miniaturized fiber-based photonic devices such as optical switches (Chiang et al., 1997), and wavelength multiplexing system (Saitoh, Sato, & Koshiba, 2003).

With the development of modern optical communication system, more compacted polarization splitters are developed as explained in section 2.5.2. In this chapter, we will numerically analyze the copper-filled based on dual-core PCF as a polarization splitter.

5.2 Numerical Simulation

5.2.1 Numerical Methods

Numerical methods for analyzing waveguides can be categorized into two types, wave propagators and mode solvers. Mode solving methods are based on the assumptions that the waveguides are uniform in the propagation direction. Whereas the wave propagation technique analyses waveguides of changing structures in the propagation direction. In this thesis, the mode solving method is considered in analyzing PCFs. A few examples of

mode solving techniques are plane wave expansion method (PWEM), multipole method (MM), eigenmodes expansion method (EME) and finite element method (FEM).

PWEM is a frequency-domain method that expresses eigenvalue problem from Maxwell's equations (S. G. Johnson & Joannopoulos, 2001). This method is mainly beneficial in solving for the band structure of a particular photonic crystal geometry, computing modal solutions of Maxwell's equations over an inhomogeneous or periodic structure. The electric or magnetic fields, together with the permittivity are expanded in terms of Fourier series components along the reciprocal lattice vector for each field component. The disadvantage of the PWEM is that the wave-vector is used as the input parameter, whereas the frequency eigenvalues are retrieved from the calculation. It is often more convenient to specify the frequency and solve for the required propagation constant for some applications involving dispersion.

MM is based on mathematical series of a function that depends on angles, which can be used for full-vector modal calculations of PCFs (Botten et al., 2005). It gives both the real and imaginary parts of the mode propagation constant with the ability to achieve high accuracy and rapid convergence with practical computational resources. Also, it treats each dielectric boundary in MM as a source of radiating fields. An advantage of the method is that it uses frequency as input parameter to solve for the propagation constant. This is important in simulation involving a dispersive media.

EME is a linear frequency domain method that relies on the decomposition of the electromagnetic fields into a set of local eigenmodes that exists in the cross-section of waveguide (Gallagher & Felici, 2003). The algorithm is fundamentally bi-directional and exploits the scattering matrix technique to connect different section of the waveguide. Therefore, all reflections are taken into account. The method can simulate light

propagation at any angle even at 90° . However, EME is limited to linear problems, and nonlinear problems may be modelled using iterative techniques.

FEM is a numerical approach for finding the estimated solutions of partial differential equation (PDE) by solving complex boundary value problems (Koshiba, 1992). The field region is divided into basic forms, such as triangular and rectangular, named as finite elements to estimate a more complex equation over a larger domain. The solution approach is based either on removing the differential equation completely as in steady state problems. Furthermore, the PDE is interpreted into the corresponding ordinary differential equations. A commercial FEM software, COMSOL Multiphysics 5.2, is used in this work.

5.2.2 Modelling

The modelling is conducted at the wavelength λ ranged from $1.2 \mu\text{m}$ to $2.0 \mu\text{m}$. The copper-filled dual-core PCF was modelled to investigate the properties of a polarization splitter. Figure 5.1 shows the flow diagram of the processes involved in obtaining simulated results.

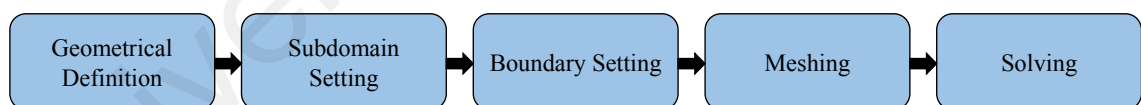


Figure 5.1: Flow diagram of simulation process

5.2.2.1 Geometrical Definition

Full structure has been considered in this work in order to investigate the existence of higher order mode. The required shapes of hexagon, circular, and rectangular are drawn through the settings of the dimensions (height and width) and the positions (x, y) . Here, circle with the same diameter d are drawn and positioned on the desired lattice with constant pitch, Λ as shown in Figure 5.2.

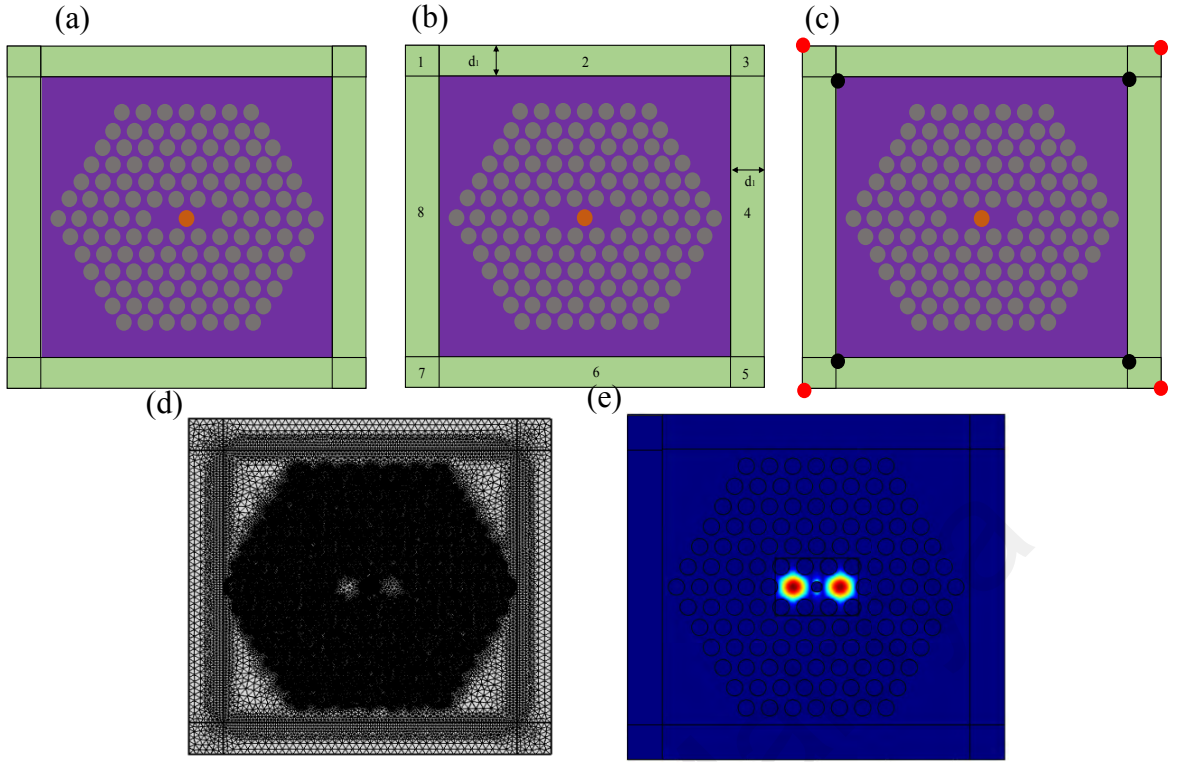


Figure 5.2: FEM simulation on copper-filled dual-cores PCF: (a) structural design; (b) subdomain definition; (c) setting of the boundary conditions; (d) mesh generation; (e) solution.

The Perfectly Matched Layers (PML) is used to avoid the energy from the outer boundaries being reflected into the domain and match an infinite structure with a finite domain. Depending on the formulation, either square as shown in Figure 5.2(a) or circular shapes can be employed.

5.2.2.2 Subdomain Setting

The physical properties of each material in each subdomain need to be set. The grey holes in Figure 5.3(a) indicate the air region (refractive index equal to 1), while the orange is copper. The purple region corresponds to fused silica, whose refractive index can be determined as a function of frequency using the Sellmeier equation (Tatian, 1984).

$$n^2(\omega) = 1 + \sum_{i=1}^p \frac{B_i \omega_i^2}{\omega_i^2 - \omega^2} \quad (5.1)$$

where resonant frequencies, ω_i and the strength of their resonances, B_i depend on the glass material. The external, green layers are the PMLs introduced to limit the

computational domain. PMLs are absorbing layers, specially designed to introduce zero reflections for any angle of incidence, frequency or polarization of the incoming electromagnetic radiation, and are therefore perfectly suited to surround the simulation area. Their original concept was introduced by Berenger in 1994 (Berenger, 1994), even though in that first definition they required the modification of Maxwell's equations. Shortly after, Sacks *et al.* demonstrated that the same absorbing and non-reflection behavior could be achieved without modifying Maxwell's equations, provided that the material is appropriately defined as anisotropic and complex (Sacks, Kingsland, Lee, & Lee, 1995). This approach is much more easily implemented into standard numerical methods and immediately gained much popularity.

According to Sacks, the PMLs are defined as anisotropic materials, whose permittivity and permeability diagonal tensors are (Sacks et al., 1995)

$$[\varepsilon] = \varepsilon_0 n^2 [\chi] \quad (5.2)$$

$$[\mu] = \mu_0 [\chi] \quad (5.3)$$

where ρ is:

$$\Lambda = \begin{bmatrix} \frac{s_y}{s_x} & 0 & 0 \\ 0 & \frac{s_x}{s_y} & 0 \\ 0 & 0 & s_x s_y \end{bmatrix} \quad (5.4)$$

where ε_0 and μ_0 are the permittivity and permeability of free space, n is the refractive index of the adjacent region and the PML parameters s_x and s_y are defined (Saitoh & Koshiba, 2001) in Table 5.1 for region 1 to 8 in Figure 5.2b.

Table 5.1: PML parameters

PML parameter	PML region							
	1	2	3	4	5	6	7	8
s_x	s_1	1	s_2	s_2	s_2	1	s_1	s_1
s_y	s_3	s_3	s_3	1	s_4	s_4	s_4	1

Here s_i ($i = 1, 2, \dots$) must be a complex number, the real part of which decreases potential evanescent waves, while the imaginary part is effective in damping the propagating waves. In many studies (including the present one) the imaginary part is modelled by a polynomially increasing profile, so that

$$s_i = b + ja_{\max} \left(\frac{\psi}{d_i} \right)^\alpha \quad (5.5)$$

where ψ is the distance from the beginning of the PML, d_i ($i = 1, 2$) is the PML width in the horizontal or vertical direction, b , a_{\max} , and α are PML free-parameters. It is decided to fix a parabolic profile ($\alpha = 2$) with $b = 1$ for all simulations according to a frequent convention in preceding studies (Poletti, 2007) and after a number of tests. A number of convergence test on the best value of a_{\max} are also conducted and these are reported in Section 5.2.4.

5.2.2.3 Boundary Setting

The physical properties of all boundaries of the simulation domain then have to be set. The boundary condition (BC) at an edge outside the PML (red dot in Figure 5.3(c)) is generally irrelevant, as the field at that point has been attenuated to a negligible level. Therefore the BCs for a full-structure simulation can be set arbitrarily. Internal boundaries between subdomains (black dot in Figure 5.3(c)) need, in COMSOL Multiphysics, to be assigned the ‘internal boundary’ condition, which guarantees the continuity of both displacement and magnetic fields at the interfaces.

5.2.2.4 Meshing

Several mesh parameters can be adjusted, to determine both accuracies of the solution and calculation time. As a general rule, a large number of triangles need to be positioned both around curved boundaries, in order to accurately define their shape. Whereas high accuracy is required (e.g. where the field is more concentrated or where it changes more rapidly). An example is provided in Figure 5.3(d) where an inner hexagonal zone has been defined around the core with the only purpose of allowing a finer mesh. Generally, a mesh convergence test is needed in order to ensure that the structure has properly meshed, and to minimize the related numerical errors (see Section 5.2.3).

5.2.2.5 Solving

The COMSOL Multiphysics utilizes MUMPS (Multifrontal Massively Parallel sparse direct Solver) as a direct solver for eigenvalue problems. Once the solver is chosen, the most important parameters to be defined are the presumption for the eigenvalue and the number of eigenvalues to be calculated around this value. For example, in the modal analysis of copper-filled dual cores PCF, the estimated effective index n_{eff} is the guess for the eigenvalue.

5.2.3 Accuracy

Convergence tests are run for the main free-parameters of the algorithm in order to verify the method. The size of the finite element mesh and the PML parameters is tested. It is generally a widespread practice as mentioned in the previous section, to fix $\alpha = 2$ and $b = 1$ in the PMLs (for example (Saitoh & Koshiba, 2001)). Therefore the parameters whose convergence will be analyzed in the following are the maximum value of the imaginary part of s_i , a_{max} , and the size of the finite element mesh.

By testing its results against the known analytical result, the general practice to validate a numerical method would be tested. However, no analytical results are available for

PCFs as has been previously explained. Furthermore, comparisons with the analytical solution of a step index fiber would be insufficient for testing the imaginary part of the propagation constant. It has become a common practice, to validate a numerical code by comparison with the results obtained with the method which is recognized as the most accurate PCF modelling: the multipole method. The most employed ‘benchmark’ for such comparisons is typically the fiber with a single ring of 6 equally spaced holes studied at $\lambda = 1450$ nm (White et al., 2002).

Figure 5.3 compares the effective index calculated by the MM ($n_{eff} = 1.445395345 + j3.150 \times 10^{-8}$) with the results obtained with the FEM for increasing values of a_{max} . A full structure with a mesh of 173412 triangles, denser in the core, has been used for the FEM. A good convergence of $\text{Im}[n_{eff}]$ is observed for α larger than 5 while the real part of n_{eff} is almost unaffected by the change of α . Therefore a value of $\alpha = 10$ will be employed for all simulations in this work. The n_{eff} convergence as a function of mesh density is shown in Figure 5.3 for the same fiber and with $\alpha = 10$.

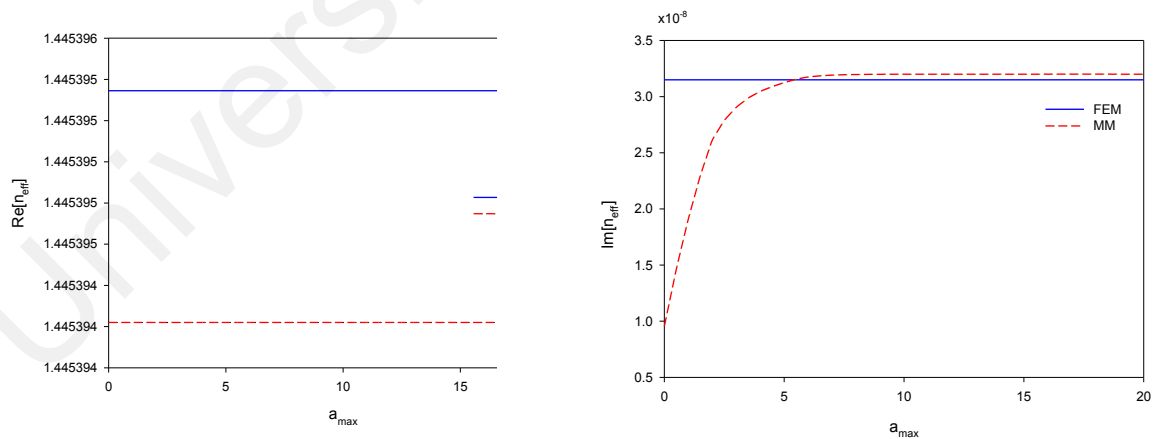


Figure 5.3: Effective index dependence on a_{max} for the fundamental mode of the fiber studied in (White et al., 2002), calculated with the FEM (blue); the MM result is shown in red for comparison.

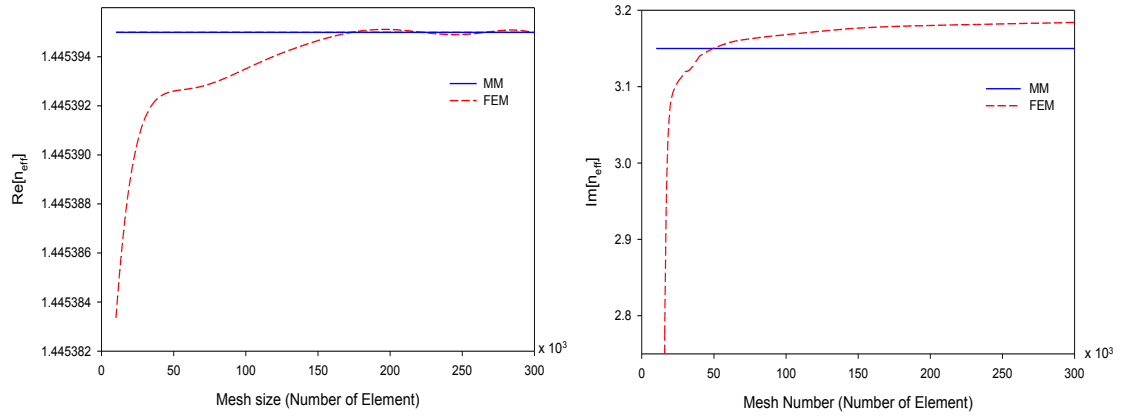


Figure 5.4: Effective index dependence on the mesh size for the fundamental mode of the fiber studied in (White et al., 2002), calculated with FEM (blue); the MM result is shown in red for comparison.

Both $Re[n_{eff}]$ and $Im[n_{eff}]$ are affected by an increase in the number of points, but for a number of triangles greater than ~ 160000 they both seem to have converged to a stable value. For this converged value the difference in the real part of n_{eff} between two methods lies in the 6th significant digit ($\sim 1 \times 10^{-6}$), while the error in the imaginary part is around 1×10^{-10} , corresponding to a variation of less than 1% in the calculated confinement loss.

The level of accuracy found for our implementation of the FEM is therefore in line with other numerical methods. For all the studies reported in this thesis it is well above the accuracy that can be obtained in practice when modelling the fabricated fibers.

5.3 Structural Design of Copper-Filled Dual Core PCF for a Use of Polarization Splitter.

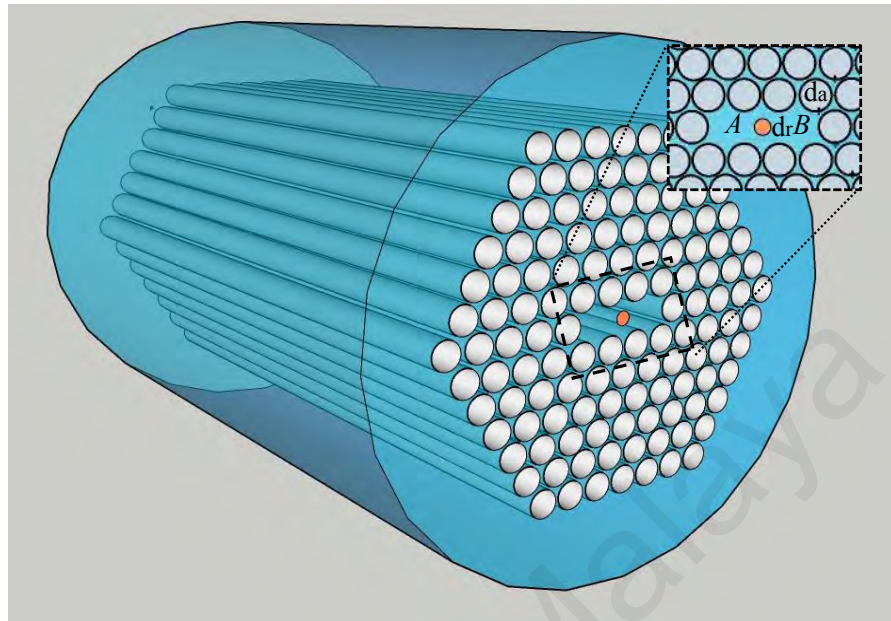


Figure 5.5: Structural design for Copper-Filled Dual Core PCF

The design of copper-filled dual-core PCF is illustrated in Figure 5.5. The diameter of the copper wire d_c is $2.97 \mu\text{m}$ is placed in the center in between the dual-cores, A and B . The PCF is arranged in a triangular lattice with pitch size of $\Lambda = 6.7 \mu\text{m}$ consisted of six rings of air holes. The cladding air holes diameter, d_a is set to be $4.69 \mu\text{m}$. Moreover, the diameter of both cores, d_r , (core A and B) are $9.57 \mu\text{m}$. The fabrication process of the copper-filled PCF is quite similar as discussed in Chapter 4. The only step to be taken is by removing two air holes and replace with silica rod and replace the centre core with copper-cane. Figure 5.6 depicts the SEM images for fabricated copper-filled dual-core PCF.

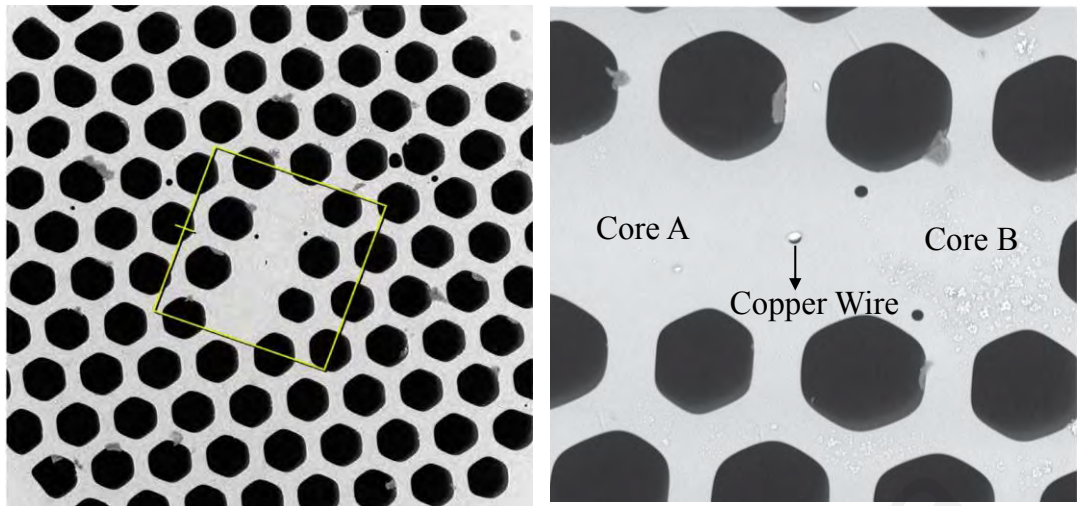


Figure 5.6: SEM images for copper-filled PCF

The refractive index of air of 1 is used. A perfectly matched layer (PML) as shown in Figure 5.7 is added to the outer layer to absorb the incident radiation and also the energy from the evanescent fields.

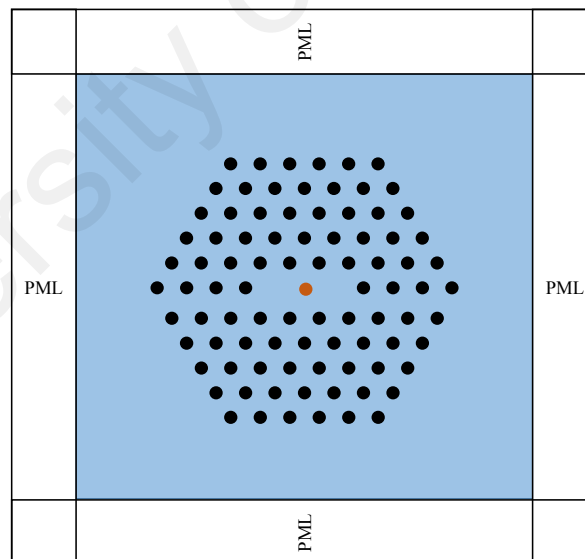


Figure 5.7: The schematic diagrams of design copper-filled PCF with PML

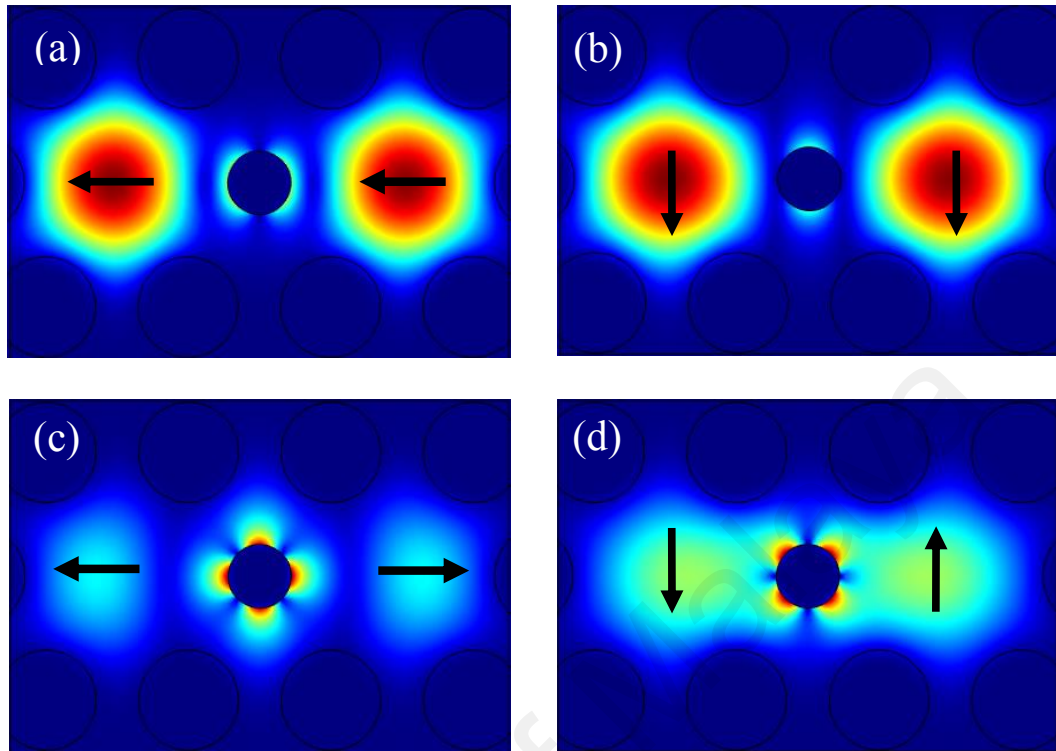


Figure 5.8: Electric field distribution for (a) x-even mode, (b) y-even mode, (c), x-odd mode, (d) y-odd mode

The dispersion of silica as the background material is following the Sellmeier equation

$$n^2(\lambda) = 1 + \frac{B_1\lambda^2}{\lambda^2 - C_1} - \frac{B_2\lambda^2}{\lambda^2 - C_2} - \frac{B_3\lambda^2}{\lambda^2 - C_3} \quad (5.6)$$

n is the refractive index of silica and λ is the wavelength. The Sellmeier coefficients are as follows:

$B_1 = 0.696163$, $B_2 = 0.4079426$, $B_3 = 0.897479401$, $C_1 = 4.67914826 \times 10^{-3} \mu\text{m}^2$, $C_2 = 1.35120631 \times 10^{-2} \mu\text{m}^2$, and $C_3 = 97.9340025 \mu\text{m}^2$ (Tatian, 1984).

Figure 5.8 shows the electric field distribution of even and odd mode for x- and y-polarization. In the numerical studies, the permittivity of copper wire is approximated by using the Drude-Lorentz model as shown in Equation 5.7:

$$\epsilon_{CU} = \epsilon_{\infty} - \frac{\omega_D^2}{\omega(\omega + j\gamma_D)} - \frac{\Delta\epsilon \cdot \Omega_L^2}{(\omega^2 - \Omega_L^2) + j\Gamma_L\omega} \quad (5.7)$$

5.4 Result and Discussion of Copper-Filled Dual Core PCF

An efficient polarization splitter will possess good coupling characteristics which can be obtained through mode coupling theory proposed by (Saitoh et al., 2003) and explained in section 4.1. According to the coupled-mode theory, as discussed in section 4.1, the dual-core PCF will have four exact modes which are even and odd modes in both x- and y-polarizations as depicted in Figure 5.8. The coupling lengths L_c is interpreted as the shortest fiber length, where the maximum power transfer occurs between the two cores. The L_c is defined as a basic parameter to represent a coupler. L_c for different polarization states is expressed as:

$$L_c = \frac{\pi}{|\beta_{even} - \beta_{odd}|} = \frac{\lambda}{2(n_{eff}^{even} - n_{eff}^{odd})} \quad (5.8)$$

where $\beta = \frac{2\pi}{\lambda}(n_{eff})$ is the propagation constant. From Equation 5.8, L_c is inversely proportional to the difference between the real effective index, $R(n_{eff})$ value of the even and the odd supermode. The length of L_c^x and L_c^y are not equal which indicates a complete power transfer for x- and y-polarization occurs at different length. In order to achieve a shorter coupling length, L_c , a high birefringence structure by considering metal will significantly increase the $R(n_{eff}^{even} - n_{eff}^{odd})$. By referring to the coupled-mode theory, the light with two polarization states is launched into one of the cores of a dual-core PCF can be exactly separated when the coupling ratio of the two polarization state meets $L_c^y/L_c^x =$

p/q , where p and q are the positive integers, and the parity should be dissimilar. At the end of the splitter, the x-polarization light in core A will still remain while the y-polarization light is coupled into core B . This implies the two-orthogonal polarization components of light are split from each other. In order to obtain the short coupling length and better performance, the optimum value of coupling ratio must be 2. When the coupling ratio of 2 is achieved, the coupling length would be $z = L_c^y$. To investigate the impact of introducing a copper wire in a dual-core PCF, we will calculate the coupling lengths of the dual-core PCF without copper wire. Figure 5.8 highlights the coupling length with and without the presence of copper wire. It is apparent from the graph depicted in Figure 5.9 that the coupling length of the PCF without the presence of copper wire is almost more than thirty times magnitude higher than the PCF with copper-filled. As illustrated in Figure 5.9 (a) the coupling length at $1.55 \mu\text{m}$ is $L_c^x = 590.7 \mu\text{m}$ and $L_c^y = 1196 \mu\text{m}$ for x- and y-polarization, respectively. Significantly, for PCF without copper-filled, the coupling length achieved at $1.55 \mu\text{m}$ is $L_c^x = 30000 \mu\text{m}$ and $L_c^y = 38000 \mu\text{m}$, for x- and y-polarization, respectively. This suggests that, by adding copper wire into the structure, the shorter coupling length could be easily obtained.

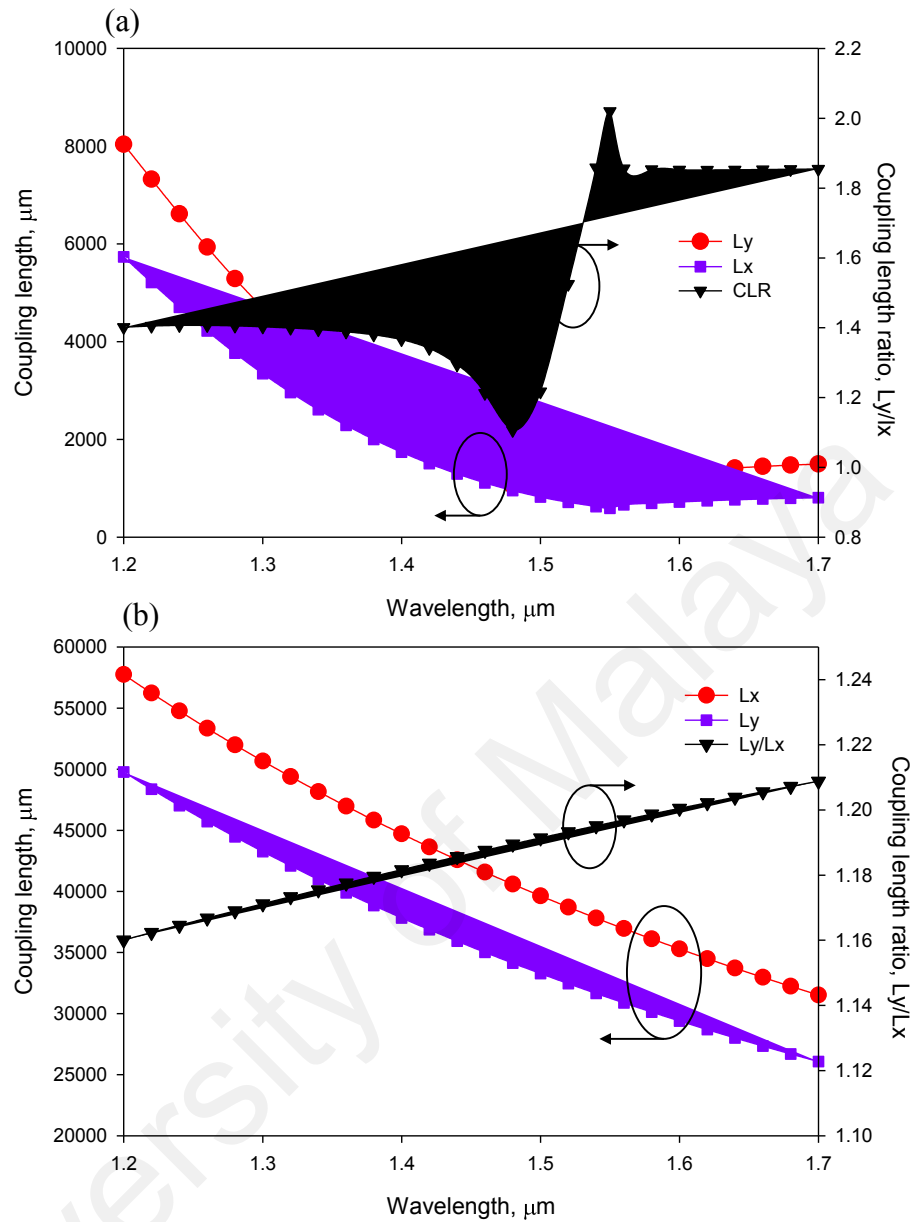


Figure 5.9: (a) The coupling length of PCF with copper-filled, (b) without copper-filled

We will denote the L_y/L_x the coupling ratio. Coupling length for x-polarization is shorter than y-polarization due to the coupling of surface plasmon mode with core-guided mode is stronger and faster power dissipation due to the horizontal position of fiber core and copper wire (P. Li & Zhao, 2013). For a given coupling length, the coupling ratio indicates the dimension and the sensitivity of the structure depending on its structure variations. On the other hand, the higher the coupling ratio, the greater the sensitivity.

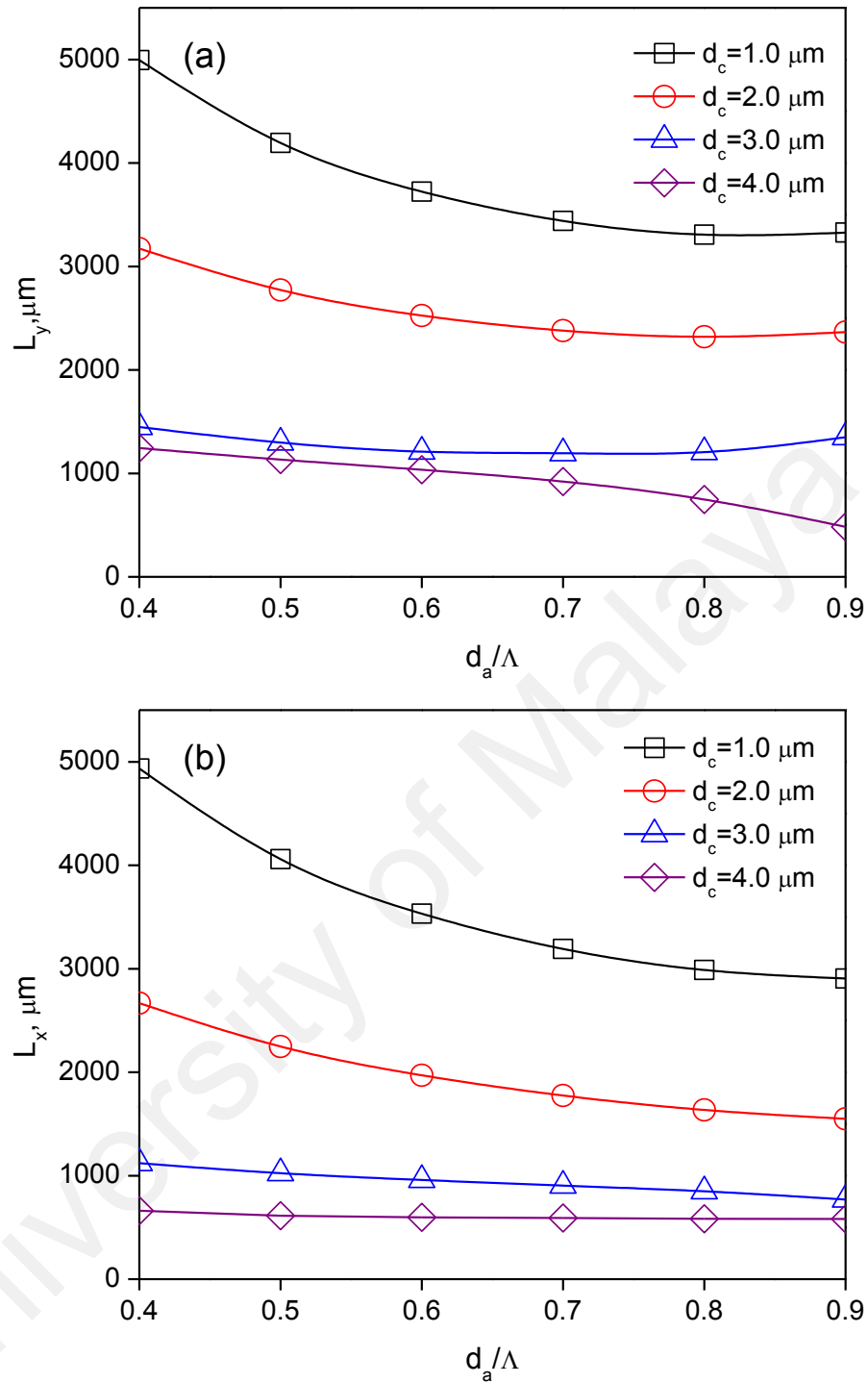


Figure 5.10: Coupling length comparison of the diameter of copper wire, d_c with respect to lattice-spacing ratio, d/Λ (a) coupling length of x-polarization (b) coupling length of y-polarization at 1.55 μm wavelength

Figure 5.10 shows a variation of coupling length of the lattice-spacing ratio, d/Λ with respect to the copper size, d_c at 1.55 μm wavelength. By varying d/Λ ratios, we could alter the coupling length between both cores. Small value of d/Λ indicates the diameter of air-holes are small compared to the size of pitch. Also, the leaky mode for smaller lattice-

spacing ratio will increase the loss of the fiber. Larger ratio of the lattice-spacing will result in better guiding in PCF by confining light from leaking (Knight et al., 1996). This leads to better coupling between core-guided mode and SPP mode. Generally, the coupling length performance improves (low L_x and L_y) as d/Λ decreases. Figure 5.11 illustrates the different between the large and small ratio of d/Λ . Figure 5.11 shows a summary of the coupling ratio for different d/Λ at $1.55 \mu\text{m}$ wavelength with respect to d_c .

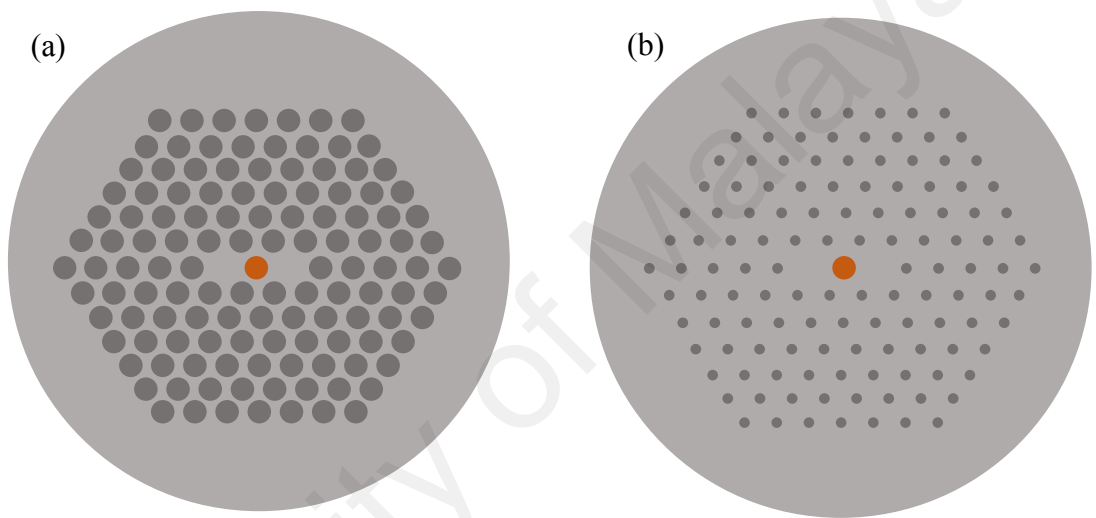


Figure 5.11: Different lattice-spacing ratio. (a) Larger ratio with larger diameter of air holes, d . (b) Smaller ratio with smaller diameter of air holes, d .

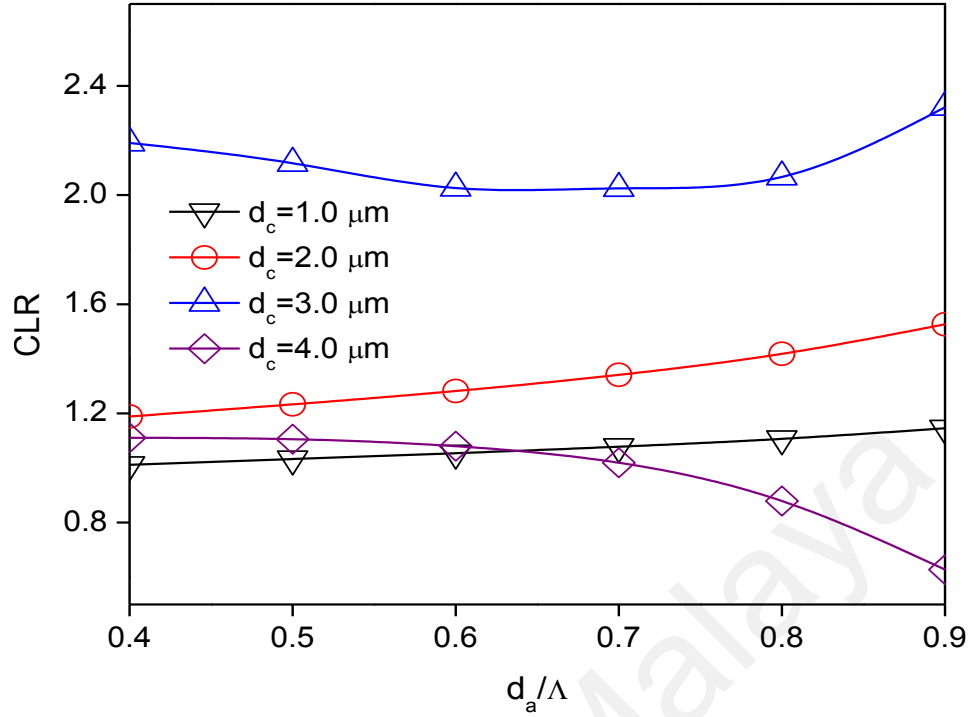


Figure 5.12: Coupling ratio comparison the diameter of copper wire, d_c with respect to lattice-spacing ratio, d/Λ at 1.55 μm wavelength

The coupling ratio for different air holes to pitch ratio, d/Λ with respect to d_c is depicted in Figure 5.12. With 0.7 d/Λ , the coupling ratio of 2 can be achieved, compared to others which could not possibly reach factor of 2. Consequently, this will result in producing a shorter splitter and high-performance polarization splitter.

The magnitude of power in the core A and core B can be defined as in Equation 5.9 and 5.10. The coupling of both core A and B can be described by the even and odd supermodes, which are formed by the coupling between the modes either from core A , or core B .

$$P_{x,y}^{out,A} = P_{in} \sin^2\left(\frac{\pi z}{2L_{x,y}}\right), \quad (5.9)$$

$$P_{x,y}^{out,A} = P_{in} \cos^2\left(\frac{\pi z}{2L_{x,y}}\right) \quad (5.10)$$

where P_{in} is the input power $L_{x,y}$ is the coupling length for x- and y polarizations, z is the fiber length.

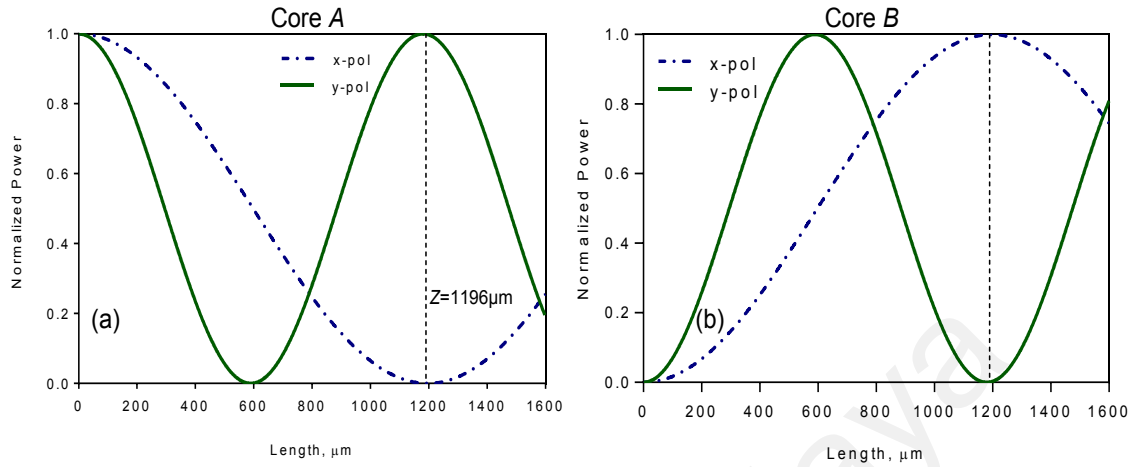


Figure 5.13: Normalized power transfer in (a) Core A, (b) Core B for the proposed dual-core copper-filled PCF at wavelength 1.55 μm

Figure 5.13 illustrates the normalized power in core A and core B along the certain propagation length. We can observe the two polarization states can be separated when the propagation length is equal to the coupling length, z . The polarized light can be separated at fiber length of $z=L_y=1196 \mu\text{m}$. When the light is launched into core A at $z(0)$, the power of y-polarization will become maximum in Core A, and when $z=1196 \mu\text{m}$, x-polarization will become maximum in Core B. This result demonstrates the capability of the proposed copper-filled dual-core PCF to split incoming light into two polarization states.

The other key fundamental of a good splitter is extinction ratio. Extinction ratio (ER) is defined as the power ratio between the unwanted and the wanted polarized states at each output core. The incident light that launches into core A for both x- and y-polarization is to be split when the ER is better than -20 dB. Consequently, ER could determine the available bandwidth if the fiber achieved better than -20 dB. The extinction ratio for core is represented in Equation 5.11:(S. Zhang et al., 2012)

$$ER = 10 \log_{10} \frac{P_{x,y}^{out,A}}{P_{x,y}^{out,B}} \quad (5.11)$$

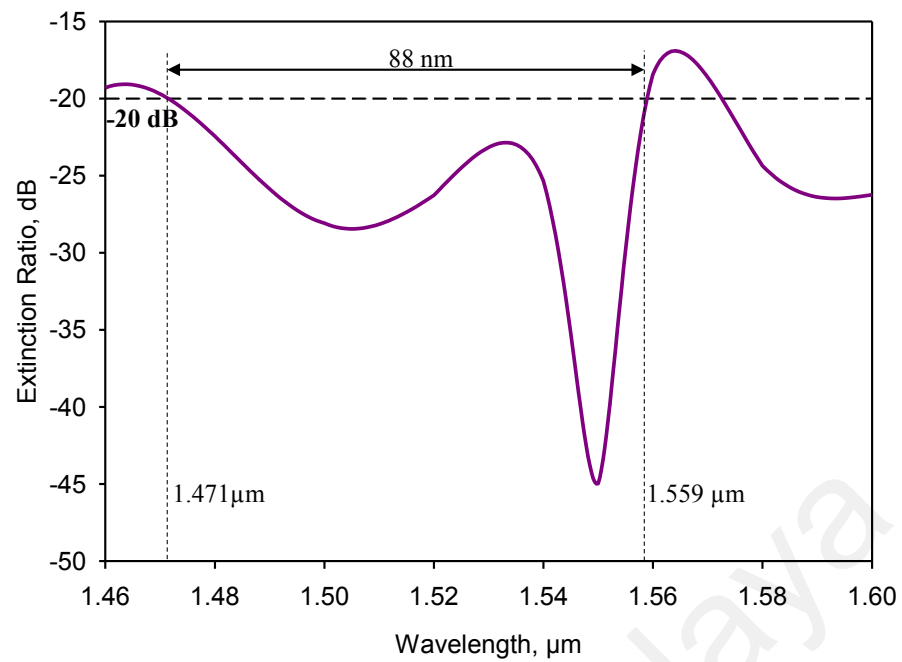


Figure 5.14: Extinction ratio of copper-filled dual-core PCF

Figure 5.14 depicts the ER as a function of wavelength when the fiber length split at $z=1196 \mu\text{m}$. The PCF obtained a very low ER of -40 dB at the wavelength of $1.55 \mu\text{m}$. The bandwidth of the PCF is 88 nm from $1.471 \mu\text{m}$ to $1.559 \mu\text{m}$ indicating the broad bandwidth splitter which operates at the wavelength of $1.55 \mu\text{m}$.

Table 5.2: Comparison with existing literature for polarization splitter

Metal-Wires	Length (mm)	Extinction Ratio-x (dB)	Extinction Ratio-y (dB)	Operating Wavelength (nm)	Bandwidth below -20 dB (nm)	References
Silver	-	-30.54	-	1550	-	(S. Zhang et al., 2012)
Gold	0.5942	-40	-40	1310	-	(P. Li & Zhao, 2013)
Silver	63	-39.4	-35.2	1550	x-pol:1441-1587 (146 nm) y-pol:1430-1605 (175 nm)	(Sun et al., 2013)
Silver	0.5775	-34	-42	1596	x-pol:1439-1689 (250 nm) y-pol:1421-1700 (279 nm)	(Sun et al., 2015)
Gold	0.2546	-111	-	1550	x-pol: 1420-1980 (560 nm)	(Khaleque et al., 2015)
Gold	0.117	-100	-	1550	x-pol: 1250-1710 (460 nm)	(Khaleque et al., 2015)
Gold	2.937	-70	-	1310	x-pol: 1290-1380 (90 nm)	(Fan et al., 2016)
Gold	4.036	-78.2	-	1550	1250-1680 (430 nm)	(L. Jiang, Zheng, Hou, Zheng, Jiyang, et al., 2015).
Gold	0.290	-56.5	-	1550	1540-1599.2 (19.2 nm)	Q. Xu, Zhao, Xia, Lin, & Zhang, 2018
Copper	1.196	-40	-	1550	1471-1559 (88 nm)	This work

5.6 Summary

To sum up, the effect of filling a copper-wire between the dual-cores in PCF was studied. The analysis from this study implies that the proposed structure would be beneficial in polarization wavelength-dependent splitter application– a passive optical device. Copper wire will increase the birefringence of the PCF structure thus would lead to shortening the coupling length between core *A* and core *B*. Furthermore, copper wire acts as a bridge to transfer the energy easily between both cores. Short coupling length is one of the key parameters of a good splitter. The coupling length for the proposed structure is 1196 μm with coupling ratio of 2 which could operate at 1.55 μm , the communication band. Plus, the extinction ratio for the copper-filled dual-core PCF is considerably low at 1.55 μm with -40 dB. The bandwidth achieved with extinction ratio lower than -20 dB is 88 nm – realizing a broadband and single splitting device which operates at 1.55 μm . Even though the existing literatures outperform this work, based on the coupling length, we successfully use fiber fabrication with single-step processes to obtain the sample. Furthermore, copper is used as a plasmonic material due to its cost-effectiveness and widespread availability compared to gold and silver.

CHAPTER 6: CONCLUSION AND FUTURE WORKS

6.1 Conclusion

Throughout my Ph.D. journey, I have demonstrated the following:

i) *Incorporating metal (copper) in fiber fabrication:*

Copper-in-glass via a standard optical fiber drawing approach was fabricated by adopting the Taylor wire process. This method opens the possibility of nano-sized copper wires encapsulated in silica. The fabrication method allows the production of copper wire encapsulated in silica as an alternative for planar substrate plasmon waveguide and also as optic-electric simultaneous transmission. Copper has low melting temperature (1081 °C) compared to silica (1900 °C). The temperature mismatch and surface tension that occur between the melted copper and the glass capillary resulted in copper globules which leads to metal discontinuity/segmentation. The issue can be circumvented by jacketing the preform tube to solve diffusion of melted copper into the glass which can lead to glass breaking. Secondly, to avoid the segmented and discontinuous copper in the glass, the melted copper is feeded by a copper wire to push the copper to the bottom of the preform before the drawing process. The results showed that the fiber can be pulled down to 170 μm with 22.9 μm copper as a core. The continuity of the fabricated copper is tested by electrical measurements. The results proved that the copper was continuous up to 600 cm long. The fabrication technique is very beneficial to design metal-dielectric structure such as metal-filled PCF and optical fiber micro and nanowire. This method can be successfully applied with different metal such as gold or silver. It can be repeated to produce nanowires which would be very useful in optical

and electric application such as biosensor, nanowire laser, optical passive devices and metamaterial devices.

ii) *Fabrication of copper-filled photonic crystal fiber for polarization filter:*

After successfully demonstrating a technique to fabricate copper-in-glass optical fiber structure, the fabricated a copper-filled photonic crystal fiber as a wavelength dependent polarization-filter was fabricated. The fabrication process of copper-filled PCF follows a conventional stack-and-draw method with an additional stage of stacking a copper cane with capillary and silica rod. This technique is well suited for mass production, ultra-clean interaction and also ensuring high repeatability.

The copper microwire is placed next to PCF core and works as polarization filter. The result showed the capability of the PCF to filter certain wavelength for both x-and y-polarization state. The phase-matching condition of the third order of SPP mode and core-guided mode occurs at 1.79 μm and 1.9 μm , respectively. The measured transmission spectrum shows a good agreement with measured loss for x- and y- polarization, with slightly shifted to a longer wavelength.

iii) *Numerical studies of copper-filled photonic crystal fiber for polarization splitter:*

The copper-filled in dual-core PCF is designed and analyzed by using commercialize software, COMSOL. The fabrication process is similar to single copper-wire polarization filter. The application of the proposed design is for polarization splitter. Copper wire will increase the birefringence of the PCF structure thus would lead to shortening the coupling length between core *A* and

core *B*. Short coupling length is one of the key parameters of good splitter. The coupling length for the proposed structure is 1196 μm with coupling ratio of 2 which could operate at 1.55 μm , the communication band. Plus, the extinction ratio for the copper-filled dual-core PCF is considerably low at 1.55 μm with -40 dB. The bandwidth achieved with extinction ratio lower than -20 dB is 88 nm – realizing a broadband and single splitting device which operates at 1.55 μm .

6.2 Future works

To further my research, I intend to fabricate and explore :

- i) *D-shaped SMF with metal coatings for biosensing.*

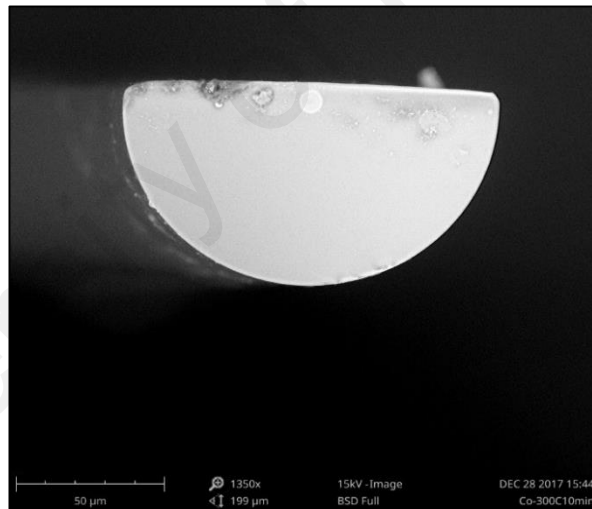


Figure 6.1: Fabricated D-shaped SMF

The D-shaped SMF is fabricated and will be coated with metal as an SPR biosensor. To date, numerous SPR sensors have been reported and most of the sensors structure are difficult to fabricate. D-shaped SMF could be potentially fabricated. The fabrication process is by polishing half side of the cane and coating a metal layer by using electron beam evaporation. Figure 6.1 shows the SEM image of D-shaped SMF that was fabricated during my PhD studies.

ii) *Wire array metamaterial*

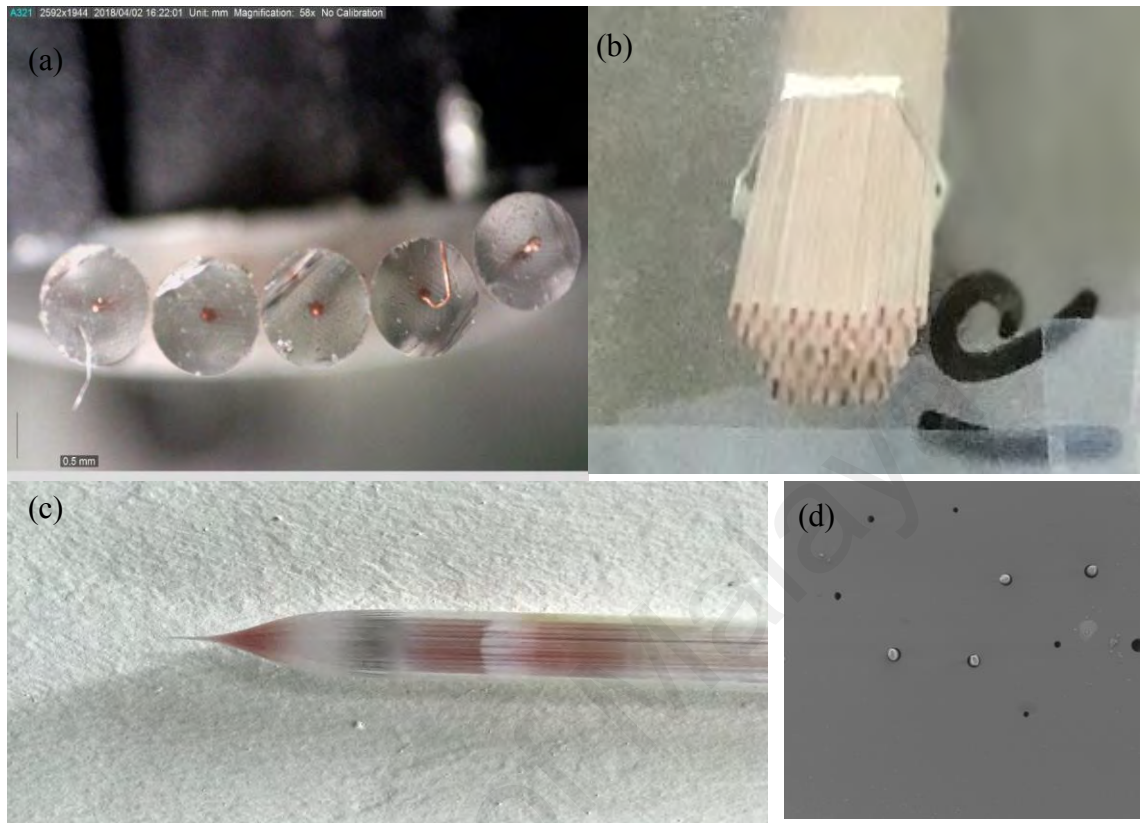


Figure 6.2: Wire array metamaterial based on copper cane (a), (b) stack copper-cane, (c) Neck-down region for stack copper-array in silica (d) SEM image for copper array cane.

Wire array metamaterial can focus light to subwavelength scale, which can be very useful for sub-wavelength imaging. The resolution of focusing and imaging devices is limited by diffraction and wire array metamaterial can solve this problem.

By using fabricated copper-cane, we will stack them in hexagonal jigs and draw down to fiber size. This technique ensures the production of wire array metamaterial. Additionally, this fabrication technique could produce nano-dimensional metal wire. A partial fabrication has been done during my PhD studies as shown in Figure 6.2.

REFERENCES

- An, G., Li, S., Yan, X., Yuan, Z., & Zhang, X. (2016). High-birefringence photonic crystal fiber polarization filter based on surface plasmon resonance. *Applied Optics*, 55(6), 1262-1266. doi: 10.1364/AO.55.001262
- Ando, R. F., Tuniz, A., Kobelke, J., & Schmidt, M. A. (2017). Analysis of nanogap-induced spectral blue-shifts of plasmons on fiber-integrated gold, silver and copper nanowires. *Optical Materials Express*, 7(5), 1486-1495. doi: 10.1364/OME.7.001486
- Atwater, H. A., & Polman, A. (2010). Plasmonics for improved photovoltaic devices. *Nature Materials*, 9, 205. doi: 10.1038/nmat2629
- Azman, M. F., Mahdiraji, G. A., Wong, W. R., Aoni, R. A., & Mahamd Adikan, F. R. (2019). Design and fabrication of copper-filled photonic crystal fiber based polarization filters. *Applied Optics*, 58(8), 2068-2075. doi: 10.1364/AO.58.002068
- Baik, J. M., Lee, S. J., & Moskovits, M. (2009). Polarized surface-enhanced Raman spectroscopy from molecules adsorbed in nano-gaps produced by electromigration in silver nanowires. *Nano letters*, 9(2), 672-676.
- Barnes, W. L., Dereux, A., & Ebbesen, T. W. (2003). Surface plasmon subwavelength optics. *Nature*, 424, 824. doi: 10.1038/nature01937
- Bei, Y., Anran, W., Exian, L., Wei, T., Jianlan, X., Rui, G., & Jianjun, L. (2018). Polarization filtering in the visible wavelength range using surface plasmon resonance and a sunflower-type photonic quasi-crystal fiber. *Journal of Physics D: Applied Physics*, 51(15), 155105.
- Berenger, J.-P. (1994). A perfectly matched layer for the absorption of electromagnetic waves. *Journal of Computational Physics*, 114(2), 185-200. doi: https://doi.org/10.1006/jcph.1994.1159
- Birks, T. A., Knight, J. C., & Russell, P. S. J. (1997). Endlessly single-mode photonic crystal fiber. *Optics Letters*, 22(13), 961-963. doi: 10.1364/OL.22.000961

- Bozhevolnyi, S. I., Volkov, V. S., Devaux, E., & Ebbesen, T. W. (2005). Channel Plasmon-Polariton Guiding by Subwavelength Metal Grooves. *Physical Review Letters*, *95*(4), 046802. doi: 10.1103/PhysRevLett.95.046802
- Bozhevolnyi, S. I., Volkov, V. S., Devaux, E., Laluet, J.-Y., & Ebbesen, T. W. (2006). Channel plasmon subwavelength waveguide components including interferometers and ring resonators. *Nature*, *440*, 508. doi: 10.1038/nature04594
- Charbonneau, R., Berini, P., Berolo, E., & Lisicka-Shrzek, E. (2000). Experimental observation of plasmon-polariton waves supported by a thin metal film of finite width. *Optics Letters*, *25*(11), 844-846. doi: 10.1364/OL.25.000844
- Chen, L., Zhang, W., Zhang, Z., Liu, Y., Sieg, J., Zhang, L., . . . Yan, T. (2014). Design for a Single-Polarization Photonic Crystal Fiber Wavelength Splitter Based on Hybrid-Surface Plasmon Resonance. *IEEE Photonics Journal*, *6*(4), 1-9. doi: 10.1109/JPHOT.2014.2331237
- Chen, Z., Holmgaard, T., Bozhevolnyi, S. I., Krasavin, A. V., Zayats, A. V., Markey, L., & Dereux, A. (2009). Wavelength-selective directional coupling with dielectric-loaded plasmonic waveguides. *Optics Letters*, *34*(3), 310-312. doi: 10.1364/OL.34.000310
- Chiang, K. S., Chow, Y. T., Richardson, D. J., Taverner, D., Dong, L., Reekie, L., & Lo, K. M. (1997). Experimental demonstration of intermodal dispersion in a two-core optical fibre. *Optics Communications*, *143*(4), 189-192. doi: [https://doi.org/10.1016/S0030-4018\(97\)00372-6](https://doi.org/10.1016/S0030-4018(97)00372-6)
- Conn, G. K. T. (1945). A thermocouple-bolometer detector. *Transactions of the Faraday Society*, *41*(0), 192-196. doi: 10.1039/TF9454100192
- Delacour, C., Blaize, S., Grosse, P., Fedeli, J. M., Bruyant, A., Salas-Montiel, R., . . . Chelnokov, A. (2010). Efficient Directional Coupling between Silicon and Copper Plasmonic Nanoslot Waveguides: toward Metal-Oxide-Silicon Nanophotonics. *Nano Letters*, *10*(8), 2922-2926. doi: 10.1021/nl101065q

- Ditlbacher, H., Hohenau, A., Wagner, D., Kreibig, U., Rogers, M., Hofer, F., . . . Krenn, J. R. (2005). Silver Nanowires as Surface Plasmon Resonators. *Physical Review Letters*, *95*(25), 257403. doi: 10.1103/PhysRevLett.95.257403
- Donald, I. W. (1987). Production, properties and applications of microwire and related products. *Journal of Materials Science*, *22*(8), 2661-2679. doi: 10.1007/bf01086455
- Dou, C., Jing, X., Li, S., Liu, Q., & Bian, J. (2016). A Photonic Crystal Fiber Polarized Filter at 1.55 μm Based on Surface Plasmon Resonance. *Plasmonics*, *11*(4), 1163-1168. doi: 10.1007/s11468-015-0155-4
- Dou, C., Jing, X., Li, S., Wu, J., & Wang, Q. (2018a). A compact and low-loss polarization splitter based on dual-core photonic crystal fiber. *Optical and Quantum Electronics*, *50*(6), 255. doi: 10.1007/s11082-018-1516-y
- Dou, C., Jing, X., Li, S., Wu, J., & Wang, Q. (2018b). Low-loss polarization filter at 1.55 μm based on photonic crystal fiber. *Optik*, *162*, 214-219. doi: <https://doi.org/10.1016/j.ijleo.2018.02.044>
- Drezet, A., Koller, D., Hohenau, A., Leitner, A., Aussenegg, F. R., & Krenn, J. R. (2007). Plasmonic Crystal Demultiplexer and Multiports. *Nano Letters*, *7*(6), 1697-1700. doi: 10.1021/nl070682p
- Du, F., Lu, Y.-Q., & Wu, S.-T. (2004). Electrically tunable liquid-crystal photonic crystal fiber. *Applied Physics Letters*, *85*(12), 2181-2183. doi: 10.1063/1.1796533
- Dudley, J. M., Genty, G., & Coen, S. (2006). Supercontinuum generation in photonic crystal fiber. *Reviews of Modern Physics*, *78*(4), 1135-1184.
- Durkan, C., Schneider, M., & Welland, M. (1999). Analysis of failure mechanisms in electrically stressed Au nanowires. *Journal of Applied Physics*, *86*(3), 1280-1286.
- Fan, Z., Li, S., Chen, H., Liu, Q., Zhang, W., An, G., . . . Bao, Y. (2015). Numerical Analysis of Polarization Filter Characteristics of D-Shaped Photonic Crystal Fiber Based on Surface Plasmon Resonance. *Plasmonics*, *10*(3), 675-680. doi: 10.1007/s11468-014-9853-6

- Fan, Z., Li, S., Liu, Q., Chen, H., & Wang, X. (2016). Plasmonic Broadband Polarization Splitter Based on Dual-Core Photonic Crystal Fiber with Elliptical Metallic Nanowires. *Plasmonics*, 11(6), 1565-1572. doi: 10.1007/s11468-016-0211-8
- Guo, X., Qiu, M., Bao, J., Wiley, B. J., Yang, Q., Zhang, X., . . . Tong, L. (2009). Direct Coupling of Plasmonic and Photonic Nanowires for Hybrid Nanophotonic Components and Circuits. *Nano Letters*, 9(12), 4515-4519. doi: 10.1021/nl902860d
- Hameed, M. F. O., Alrayk, Y. K., Shaalan, A., El Deeb, W. S., & Obayya, S. (2016). Novel multichannel surface plasmon resonance photonic crystal fiber biosensor. Paper presented at the SPIE Photonics Europe.
- Hecht, B., Bielefeldt, H., Novotny, L., Inouye, Y., & Pohl, D. W. (1996). Local Excitation, Scattering, and Interference of Surface Plasmons. *Physical Review Letters*, 77(9), 1889-1892. doi: 10.1103/PhysRevLett.77.1889
- Heikal, A. M., Hussain, F. F. K., Hameed, M. F. O., & Obayya, S. S. A. (2015). Efficient Polarization Filter Design Based on Plasmonic Photonic Crystal Fiber. *Journal of Lightwave Technology*, 33(13), 2868-2875.
- Holmgaard, T., Chen, Z., Bozhevolnyi, S. I., Markey, L., Dereux, A., Krasavin, A. V., & Zayats, A. V. (2009). Wavelength selection by dielectric-loaded plasmonic components. *Applied Physics Letters*, 94(5), 051111. doi: 10.1063/1.3078235
- Hou, J., Bird, D., George, A., Maier, S., Kuhlmeiy, B. T., & Knight, J. C. (2008). Metallic mode confinement in microstructured fibres. *Optics Express*, 16(9), 5983-5990. doi: 10.1364/OE.16.005983
- Huang, M. H., Mao, S., Feick, H., Yan, H., Wu, Y., Kind, H., . . . Yang, P. (2001). Room-temperature ultraviolet nanowire nanolasers. *Science*, 292(5523), 1897-1899.
- Jiang, H., Wang, E., Zhang, J., Hu, L., Mao, Q., Li, Q., & Xie, K. (2014). Polarization splitter based on dual-core photonic crystal fiber. *Optics Express*, 22(25), 30461-30466.

- Jiang, L.-h., Zheng, Y., Yang, J.-j., Hou, L.-t., Peng, J.-y., & Zhao, X.-t. (2016). Design of an ultrashort single-polarization wavelength splitter based on gold-filled square-lattice photonic crystal fiber. *Optical and Quantum Electronics*, 48(8), 409. doi: 10.1007/s11082-016-0674-z
- Jiang, L., Zheng, Y., Hou, L., Zheng, K., Jiying, P., & Zhao, X. (2015). An ultrabroadband polarization splitter based on square-lattice dual-core photonic crystal fiber with a gold wire (Vol. 351).
- Jiang, L., Zheng, Y., Hou, L., Zheng, K., Peng, J., & Zhao, X. (2015). An ultrabroadband polarization splitter based on square-lattice dual-core photonic crystal fiber with a gold wire. *Optics Communications*, 351, 50-56.
- Johnson, P. B., & Christy, R. W. (1972). Optical Constants of the Noble Metals. *Physical Review B*, 6(12), 4370-4379.
- Johnson, S. G., & Joannopoulos, J. D. (2001). Block-iterative frequency-domain methods for Maxwell's equations in a planewave basis. *Optics Express*, 8(3), 173-190. doi: 10.1364/OE.8.000173
- Khaleque, A., Mironov, E. G., & Hattori, H. T. (2015). Analysis of the properties of a dual-core plasmonic photonic crystal fiber polarization splitter. *Applied Physics B*, 121(4), 523-532. doi: 10.1007/s00340-015-6264-0
- Knight, J. C., Birks, T. A., Russell, P. S. J., & Atkin, D. M. (1996). All-silica single-mode optical fiber with photonic crystal cladding. *Optics Letters*, 21(19), 1547-1549. doi: 10.1364/OL.21.001547
- Kretschmann, E., & Raether, H. (1968). Notizen: Radiative Decay of Non Radiative Surface Plasmons Excited by Light *Zeitschrift für Naturforschung A* (Vol. 23, pp. 2135).
- Lee, H., Schmidt, M., Tyagi, H., Sempere, L. P., & Russell, P. S. J. (2008). Polarization-dependent coupling to plasmon modes on submicron gold wire in photonic crystal fiber. *Applied Physics Letters*, 93(11), 111102.
- Li, P., & Zhao, J. (2013). Polarization-dependent coupling in gold-filled dual-core photonic crystal fibers. *Optics Express*, 21(5), 5232-5238. doi: 10.1364/OE.21.005232

- Li, W., Ren, K., & Zhou, J. (2016). Aluminum-based localized surface plasmon resonance for biosensing. *TrAC Trends in Analytical Chemistry*, 80, 486-494.
- Liang, G., Luo, Z., Liu, K., Wang, Y., Dai, J., & Duan, Y. (2016). Fiber Optic Surface Plasmon Resonance-Based Biosensor Technique: Fabrication, Advancement, and Application. *Critical Reviews in Analytical Chemistry*, 46(3), 213-223.
- Liu, N., Hentschel, M., Weiss, T., Alivisatos, A. P., & Giessen, H. (2011). Three-Dimensional Plasmon Rulers. *Science*, 332(6036), 1407-1410. doi: 10.1126/science.1199958
- Liu, Q., Li, S.-G., Fan, Z.-K., Zhang, W., Li, H., Zi, J.-C., & An, G.-W. (2015). Numerical analysis of ultrabroadband polarization splitter based on gold-filled dual-core photonic crystal fiber. *Optics Communications*, 334, 46-50. doi: https://doi.org/10.1016/j.optcom.2014.08.019
- Liu, Q., Li, S., Gao, X., & Feng, X. (2017). Simulation of a short and broadband polarization splitter based on photonic crystal fiber filled with tellurite glass. *Optical and Quantum Electronics*, 49(2), 60. doi: 10.1007/s11082-017-0896-8
- Logvinenko, S. P., Mikhina, G. F., & Mende, G. T. (1984). Low temperature indium resistance thermometer. *Cryogenics*, 24(8), 421-422. doi: https://doi.org/10.1016/0011-2275(84)90016-X
- Lou, J., Cheng, T., & Li, S. (2018). Surface plasmon induced dual-wavelength photonic crystal fiber polarizing filter based on coupling between core mode and SPP mode. *Optics Communications*, 426, 267-272. doi: https://doi.org/10.1016/j.optcom.2018.05.054
- Lu, W., Lou, S., & Wang, X. (2013). Ultrabroadband polarization splitter based on a modified three-core photonic crystal fiber. *Applied Optics*, 52(35), 8494-8500. doi: 10.1364/AO.52.008494
- Luan, F., George, A. K., Hedley, T. D., Pearce, G. J., Bird, D. M., Knight, J. C., & Russell, P. S. J. (2004). All-solid photonic bandgap fiber. *Optics Letters*, 29(20), 2369-2371. doi: 10.1364/OL.29.002369

- Martin, C. R. (1994). Nanomaterials--a membrane-based synthetic approach: DTIC Document.
- Menke, E., Thompson, M., Xiang, C., Yang, L., & Penner, R. (2006). Lithographically patterned nanowire electrodeposition. *Nature Materials*, 5(11), 914-919.
- Miliou, A. N., Srivastava, R., & Ramaswamy, R. V. (1993). A 1.3 μm directional coupler polarization splitter by ion exchange. *Journal of Lightwave Technology*, 11(2), 220-225.
- Novotny, L., & van Hulst, N. (2011). Antennas for light. *Nature Photonics*, 5, 83. doi: 10.1038/nphoton.2010.237
- Ortigosa-Blanch, A., Knight, J. C., Wadsworth, W. J., Arriaga, J., Mangan, B. J., Birks, T. A., & Russell, P. S. J. (2000). Highly birefringent photonic crystal fibers. *Optics Letters*, 25(18), 1325-1327. doi: 10.1364/OL.25.001325
- Otto, A. (1968). Excitation of nonradiative surface plasma waves in silver by the method of frustrated total reflection. *Zeitschrift für Physik A Hadrons and nuclei*, 216(4), 398-410. doi: 10.1007/bf01391532
- Paul, A. K., Sarkar, A. K., Rahman, A. B. S., & Khaleque, A. (2018). Twin Core Photonic Crystal Fiber Plasmonic Refractive Index Sensor. *IEEE Sensors Journal*, 18(14), 5761-5769. doi: 10.1109/JSEN.2018.2841035
- Peng, G., Tjugiarto, T., & Chu, P. (1990). Polarisation beam splitting using twin-elliptic-core optical fibres. *Electronics Letters*, 26(10), 682-683.
- Percival, S. J., Vartanian, N. E., & Zhang, B. (2014). Laser-pulled ultralong platinum and gold nanowires. *RSC Advances*, 4(21), 10491-10498. doi: 10.1039/C3RA47207H
- Poletti, F. (2007). Direct and inverse design of microstructured optical fibres. University of Southampton.
- Polman, A., & Atwater, H. A. (2012). Photonic design principles for ultrahigh-efficiency photovoltaics. *Nature Materials*, 11, 174. doi: 10.1038/nmat3263

Reeves, W. H., Skryabin, D. V., Biancalana, F., Knight, J. C., Russell, P. S. J., Omenetto, F. G., . . . Taylor, A. J. (2003). Transformation and control of ultra-short pulses in dispersion-engineered photonic crystal fibres. *Nature*, *424*, 511. doi: 10.1038/nature01798

Russell, P. (2003). Photonic Crystal Fibers. *Science*, *299*(5605), 358-362. doi: 10.1126/science.1079280

Russell, P. (2007). Photonic Crystal Fiber: Finding the Holey Grail. *Optics and Photonics News*, *18*(7), 26-31. doi: 10.1364/OPN.18.7.000026

Russell, P. S. J. (2006). Photonic-Crystal Fibers. *Journal of Lightwave Technology*, *24*(12), 4729-4749.

Saitoh, K., Sato, Y., & Koshiba, M. (2003). Coupling characteristics of dual-core photonic crystal fiber couplers. *Optics Express*, *11*(24), 3188-3195. doi: 10.1364/OE.11.003188

Salomon, L., Bassou, G., Aourag, H., Dufour, J. P., de Fornel, F., Carcenac, F., & Zayats, A. V. (2002). Local excitation of surface plasmon polaritons at discontinuities of a metal film: Theoretical analysis and optical near-field measurements. *Physical Review B*, *65*(12), 125409. doi: 10.1103/PhysRevB.65.125409

Schmidt, M. A., Prill Sempere, L. N., Tyagi, H. K., Poulton, C. G., & Russell, P. S. J. (2008). Waveguiding and plasmon resonances in two-dimensional photonic lattices of gold and silver nanowires. *Physical Review B*, *77*(3), 033417. doi: 10.1103/PhysRevB.77.033417

Schmidt, M. A., Sempere, L. P., Tyagi, H. K., Poulton, C. G., & Russell, P. S. J. (2008). Waveguiding and plasmon resonances in two-dimensional photonic lattices of gold and silver nanowires. *Physical Review B*, *77*(3), 033417.

Shi, F., Zhou, G., Li, D., Peng, L., Hou, Z., & Xia, C. (2015). Surface Plasmon Mode Coupling in Photonic Crystal Fiber Symmetrically Filled with Ag/Au Alloy Wires. *Plasmonics*, *10*(2), 335-340. doi: 10.1007/s11468-014-9813-1

Skinner, K., Dwyer, C., & Washburn, S. (2006). Selective functionalization of arbitrary nanowires. *Nano Letters*, *6*(12), 2758-2762.

- Sun, B., Chen, M.-Y., Zhang, Y.-K., & Zhou, J. (2015). Polarization-dependent coupling characteristics of metal-wire filled dual-core photonic crystal fiber. *Optical and Quantum Electronics*, 47(2), 441-451. doi: 10.1007/s11082-014-9926-y
- Sun, B., Chen, M.-Y., Zhou, J., & Zhang, Y.-K. (2013). Surface Plasmon Induced Polarization Splitting Based on Dual-Core Photonic Crystal Fiber with Metal Wire. *Plasmonics*, 8(2), 1253-1258. doi: 10.1007/s11468-013-9542-x
- Tatian, B. (1984). Fitting refractive-index data with the Sellmeier dispersion formula. *Applied Optics*, 23(24), 4477-4485. doi: 10.1364/AO.23.004477
- Taylor, G. (1924). A method of drawing metallic filaments and a discussion of their properties and uses. *Physical Review*, 23(5), 655.
- Taylor, G. F. (1924). A Method of Drawing Metallic Filaments and a Discussion of their Properties and Uses. *Physical Review*, 23(5), 655-660.
- Tuniz, A., Lwin, R., Argyros, A., Fleming, S. C., Pogson, E. M., Constable, E., . . . Kuhlmeiy, B. T. (2011). Stacked-and-drawn metamaterials with magnetic resonances in the terahertz range. *Optics Express*, 19(17), 16480-16490.
- Tyagi, H., Lee, H., Uebel, P., Schmidt, M., Joly, N., Scharrer, M., & Russell, P. S. J. (2010). Plasmon resonances on gold nanowires directly drawn in a step-index fiber. *Optics Letters*, 35(15), 2573-2575.
- Wadsworth, W., Knight, J., & Birks, T. (2012). State-of-the-Art Photonic Crystal Fiber. *Optics and Photonics News*, 23(3), 24-31. doi: 10.1364/OPN.23.3.000024
- Wang, J., Pei, L., Weng, S., Wu, L., Huang, L., Ning, T., & Li, J. (2017). A Tunable Polarization Beam Splitter Based on Magnetic Fluids-Filled Dual-Core Photonic Crystal Fiber. *IEEE Photonics Journal*, 9(1), 1-10. doi: 10.1109/JPHOT.2017.2656248
- Wang, Y. Y., Wheeler, N. V., Couny, F., Roberts, P. J., & Benabid, F. (2011). Low loss broadband transmission in hypocycloid-core Kagome hollow-core photonic crystal fiber. *Optics Letters*, 36(5), 669-671. doi: 10.1364/OL.36.000669
- White, T. P., Kuhlmeiy, B. T., McPhedran, R. C., Maystre, D., Renversez, G., de Sterke, C. M., & Botten, L. C. (2002). Multipole method for microstructured optical

fibers. I. Formulation. *Journal of the Optical Society of America B*, 19(10), 2322-2330. doi: 10.1364/JOSAB.19.002322

Wiley, B. J., Wang, Z., Wei, J., Yin, Y., Cobden, D. H., & Xia, Y. (2006). Synthesis and electrical characterization of silver nanobeams. *Nano Letters*, 6(10), 2273-2278.

Wong, W. R., Krupin, O., Adikan, F. R. M., & Berini, P. (2015). Optimization of long-range surface plasmon waveguides for attenuation-based biosensing. *Journal of Lightwave Technology*, 33(15), 3234-3242.

Wong, W. R., Krupin, O., Sekaran, S. D., Mahamd Adikan, F. R., & Berini, P. (2014). Serological diagnosis of dengue infection in blood plasma using long-range surface plasmon waveguides. *Analytical Chemistry*, 86(3), 1735-1743.

Wong, W. R., Sekaran, S. D., Adikan, F. R. M., & Berini, P. (2016). Detection of dengue NS1 antigen using long-range surface plasmon waveguides. *Biosensors and Bioelectronics*, 78, 132-139.

Wu, C. W., Wu, T.-L., & Chang, H.-C. (1995). A novel fabrication method for all-fiber, weakly fused, polarization beamsplitters. *IEEE Photonics Technology Letters*, 7(7), 786-788.

Wu, J., Li, S., Dou, C., & Liu, Q. (2017). A high extinction and wide bandwidth polarization filter based on surface plasmon resonance. *Optical and Quantum Electronics*, 50(1), 16. doi: 10.1007/s11082-017-1271-5

Wu, J., Li, S., Jing, X., Dou, C., & Wang, Y. (2018). Elliptical Photonic Crystal Fiber Polarization Filter Combined with Surface Plasmon Resonance. *IEEE Photonics Technology Letters*, 30(15), 1368-1371. doi: 10.1109/LPT.2018.2845459

Xu, Q., Zhao, Y., Xia, H., Lin, S.-B., & Zhang, Y. (2018). Ultrashort polarization splitter based on dual-core photonic crystal fibers with gold wire.

Xu, Z., Shen, C., Sun, S., & Gao, H.-J. (2009). Growth of Au nanowires at the interface of air/water. *The Journal of Physical Chemistry C*, 113(34), 15196-15200.

Xue, J., Li, S., Xiao, Y., Qin, W., Xin, X., & Zhu, X. (2013). Polarization filter characters of the gold-coated and the liquid filled photonic crystal fiber based on surface plasmon resonance. *Optics Express*, 21(11), 13733-13740. doi: 10.1364/OE.21.013733

- Yablonovitch, E. (2001). PHOTONIC CRYSTALS: SEMICONDUCTORS OF LIGHT. *Scientific American*, 285(6), 46-55.
- Yan, R., Pausauskie, P., Huang, J., & Yang, P. (2009). Direct photonic–plasmonic coupling and routing in single nanowires. *Proceedings of the National Academy of Sciences*, 106(50), 21045-21050. doi: 10.1073/pnas.0902064106
- Zayats, A. V., Smolyaninov, I. I., & Maradudin, A. A. (2005). Nano-optics of surface plasmon polaritons. *Physics Reports*, 408(3), 131-314. doi: <https://doi.org/10.1016/j.physrep.2004.11.001>
- Zhang, S., Yu, X., Zhang, Y., Shum, P., Zhang, Y., Xia, L., & Liu, D. (2012). Theoretical study of dual-core photonic crystal fibers with metal wire. *IEEE Photonics Journal*, 4(4), 1178-1187.
- Zhang, W., Li, S.-g., An, G.-W., Fan, Z.-K., & Bao, Y.-J. (2014). Polarization filter characteristics of photonic crystal fibers with square lattice and selectively filled gold wires. *Applied Optics*, 53(11), 2441-2445. doi: 10.1364/AO.53.002441
- Zhang, W., Lou, S., & Wang, X. (2018). A polarization filter based on a novel photonic crystal fiber with a gold-coated air hole by using surface plasmon resonance. *Plasmonics*, 13(2), 365-371. doi: 10.1007/s11468-017-0520-6
- Zhang, X., Wang, R., Cox, F., Kuhlmeier, B., & Large, M. (2007). Selective coating of holes in microstructured optical fiber and its application to in-fiber absorptive polarizers. *Optics Express*, 15(24), 16270-16278.
- Zhang, Z., Shi, Y., Bian, B., & Lu, J. (2008). Dependence of leaky mode coupling on loss in photonic crystal fiber with hybrid cladding. *Optics Express*, 16(3), 1915-1922. doi: 10.1364/OE.16.001915
- Zhou, X., Li, S., Cheng, T., & An, G. (2018). Design of offset core photonic crystal fiber filter based on surface plasmon resonance. *Optical and Quantum Electronics*, 50(3), 157.

LIST OF PUBLICATIONS AND PAPERS PRESENTED

A. Publications

1. Mohd Fahmi Bin Azman, Rifat Ahmmed A, Poh Soo Yong, Wong Wei Ru, Ghafour Mahdiraji, Faisal Rafiq Mahamd Adikan, Polarization Beam Splitter Based on Dual-Core Spiral Photonic Crystal Fibers with Gold Microwire. *Journal of Modern Optics. Accepted*
2. Mohd Fahmi Azman, Ghafour Amouzad Mahdiraji, Wei Ru Wong, Rifat Ahmmed Aoni, and Faisal Rafiq Mahamd Adikan, "Design and fabrication of copper-filled photonic crystal fiber based polarization filters," *Appl. Opt.* 58, 2068-2075 (2019) – (Azman, Mahdiraji, Wong, Aoni, & Mahamd Adikan, 2019) Editor's Pick
3. Mohd Fahmi Bin Azman, Rifat Ahmmed A, Wong Wei Ru, Ghafour Mahdiraji, Faisal Rafiq Mahamd Adikan, Twin-Core Sunflower-Type Photonic Quasicrystal Fibers Incorporated Gold, Silver, and Copper Microwire: An Ultrashort and Broad bandwidth Polarization Splitter, *Optical Quantum and Electronics*, Springer. *Under Review*

B. Conference

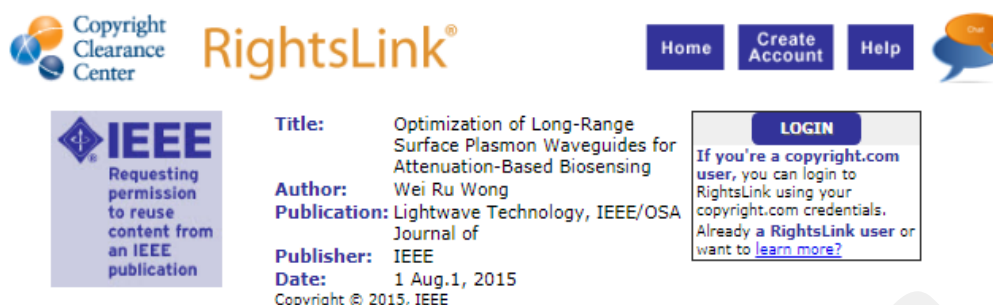
1. Mohd Fahmi Bin Azman, Ghafour Mahdiraji, Faisal Rafiq Mahamd Adikan, Fabrication of Metres-Length Continuous Copper-Core Optical Fibre via Top-Down Approach for Plasmon Based Application, CLEO/Europe-EQEC 2017, Poster Presentation.

C. Patent

1. Method of Forming A Microcapillary Structure From Capillary Tubes, Malaysia Patent Application Number PI 2018701699

LIST OF APPENDICES: COPYRIGHT AND PERMISSION FROM JOURNALS

A.1 Figure 1.1



The screenshot shows the Copyright Clearance Center RightsLink interface. On the left is the IEEE logo with the text "Requesting permission to reuse content from an IEEE publication". In the center, the following metadata is displayed:

- Title:** Optimization of Long-Range Surface Plasmon Waveguides for Attenuation-Based Biosensing
- Author:** Wei Ru Wong
- Publication:** Lightwave Technology, IEEE/OSA Journal of
- Publisher:** IEEE
- Date:** 1 Aug.1, 2015

Below the metadata is the text "Copyright © 2015, IEEE". On the right side of the interface, there are navigation buttons for "Home", "Create Account", and "Help". A "LOGIN" button is also present, with a text box below it that reads: "If you're a copyright.com user, you can login to RightsLink using your copyright.com credentials. Already a RightsLink user or want to [learn more?](#)".

Thesis / Dissertation Reuse

The IEEE does not require individuals working on a thesis to obtain a formal reuse license, however, you may print out this statement to be used as a permission grant:

Requirements to be followed when using any portion (e.g., figure, graph, table, or textual material) of an IEEE copyrighted paper in a thesis:

- 1) In the case of textual material (e.g., using short quotes or referring to the work within these papers) users must give full credit to the original source (author, paper, publication) followed by the IEEE copyright line © 2011 IEEE.
- 2) In the case of illustrations or tabular material, we require that the copyright line © [Year of original publication] IEEE appear prominently with each reprinted figure and/or table.
- 3) If a substantial portion of the original paper is to be used, and if you are not the senior author, also obtain the senior author's approval.

Requirements to be followed when using an entire IEEE copyrighted paper in a thesis:

- 1) The following IEEE copyright/ credit notice should be placed prominently in the references: © [year of original publication] IEEE. Reprinted, with permission, from [author names, paper title, IEEE publication title, and month/year of publication]
- 2) Only the accepted version of an IEEE copyrighted paper can be used when posting the paper or your thesis on-line.
- 3) In placing the thesis on the author's university website, please display the following message in a prominent place on the website: In reference to IEEE copyrighted material which is used with permission in this thesis, the IEEE does not endorse any of [university/educational entity's name goes here]'s products or services. Internal or personal use of this material is permitted. If interested in reprinting/republishing IEEE copyrighted material for advertising or promotional purposes or for creating new collective works for resale or redistribution, please go to http://www.ieee.org/publications_standards/publications/rights/rights_link.html to learn how to obtain a License from RightsLink.

If applicable, University Microfilms and/or ProQuest Library, or the Archives of Canada may supply single copies of the dissertation.

**AIP PUBLISHING LICENSE
TERMS AND CONDITIONS**

Jun 28, 2018

This Agreement between Universiti Malaya -- Mohd Fahmi Bin Azman ("You") and AIP Publishing ("AIP Publishing") consists of your license details and the terms and conditions provided by AIP Publishing and Copyright Clearance Center.

License Number	4376380707384
License date	Jun 26, 2018
Licensed Content Publisher	AIP Publishing
Licensed Content Publication	Applied Physics Letters
Licensed Content Title	Wavelength selection by dielectric-loaded plasmonic components
Licensed Content Author	Tobias Holmgaard, Zhuo Chen, Sergey I. Bozhevolnyi, et al
Licensed Content Date	Feb 2, 2009
Licensed Content Volume	94
Licensed Content Issue	5
Type of Use	Thesis/Dissertation
Requestor type	Student
Format	Electronic
Portion	Figure/Table
Number of figures/tables	1
Title of your thesis / dissertation	DESIGN AND FABRICATION OF COPPER-FILLED PHOTONIC CRYSTAL FIBER FOR PASSIVE OPTICAL DEVICES
Expected completion date	Sep 2018
Estimated size (number of pages)	130
Requestor Location	Universiti Malaya M-4-14, Faculty of Engineering Level 4, Electrical Engineering Faculty of Engineering Kuala Lumpur, Kuala Lumpur 50603 Malaysia Attn: Mohd fahmi Bin Azman
Billing Type	Invoice
Billing Address	Universiti Malaya M-4-14, Faculty of Engineering Level 4, Electrical Engineering Faculty of Engineering Kuala Lumpur, Malaysia 50603 Attn: Mohd fahmi Bin Azman
Total	0.00 USD
Terms and Conditions	

SPRINGER NATURE LICENSE
TERMS AND CONDITIONS

Jun 28, 2018

This Agreement between Universiti Malaya -- Mohd Fahmi Bin Azman ("You") and Springer Nature ("Springer Nature") consists of your license details and the terms and conditions provided by Springer Nature and Copyright Clearance Center.

License Number	4376440163401
License date	Jun 26, 2018
Licensed Content Publisher	Springer Nature
Licensed Content Publication	Nature Materials
Licensed Content Title	Plasmonics for improved photovoltaic devices
Licensed Content Author	Harry A. Atwater, Albert Polman
Licensed Content Date	Feb 19, 2010
Licensed Content Volume	9
Licensed Content Issue	3
Type of Use	Thesis/Dissertation
Requestor type	academic/university or research institute
Format	electronic
Portion	figures/tables/illustrations
Number of figures/tables/illustrations	1
High-res required	no
Will you be translating?	no
Circulation/distribution	<501
Author of this Springer Nature content	no
Title	DESIGN AND FABRICATION OF COPPER-FILLED PHOTONIC CRYSTAL FIBER FOR PASSIVE OPTICAL DEVICES
Instructor name	n/a
Institution name	n/a
Expected presentation date	Sep 2018
Portions	Figure 7 (c) and (d)
Requestor Location	Universiti Malaya M-4-14, Faculty of Engineering Level 4, Electrical Engineering Faculty of Engineering Kuala Lumpur, Kuala Lumpur 50603 Malaysia Attn: Mohd fahmi Bin Azman

A.2 Figure 2.3

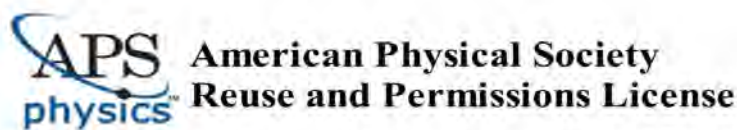
ELSEVIER LICENSE TERMS AND CONDITIONS

Jun 28, 2018

This Agreement between Universiti Malaya -- Mohd Fahmi Bin Azman ("You") and Elsevier ("Elsevier") consists of your license details and the terms and conditions provided by Elsevier and Copyright Clearance Center.

License Number	4376440375588
License date	Jun 26, 2018
Licensed Content Publisher	Elsevier
Licensed Content Publication	Physics Reports
Licensed Content Title	Nano-optics of surface plasmon polaritons
Licensed Content Author	Anatoly V. Zayats,Igor I. Smolyaninov,Alexei A. Maradudin
Licensed Content Date	Mar 1, 2005
Licensed Content Volume	408
Licensed Content Issue	3-4
Licensed Content Pages	184
Start Page	131
End Page	314
Type of Use	reuse in a thesis/dissertation
Intended publisher of new work	other
Portion	figures/tables/illustrations
Number of figures/tables/illustrations	1
Format	electronic
Are you the author of this Elsevier article?	No
Will you be translating?	No
Original figure numbers	Figure 5
Title of your thesis/dissertation	DESIGN AND FABRICATION OF COPPER-FILLED PHOTONIC CRYSTAL FIBER FOR PASSIVE OPTICAL DEVICES
Expected completion date	Sep 2018
Estimated size (number of pages)	130
Requestor Location	Universiti Malaya M-4-14, Faculty of Engineering Level 4, Electrical Engineering Faculty of Engineering Kuala Lumpur, Kuala Lumpur 50603 Malaysia Attn: Mohd fahmi Bin Azman

A.3 Figure 2.7



18-Jul-2018

This license agreement between the American Physical Society ("APS") and Mohd fahmi Azman ("You") consists of your license details and the terms and conditions provided by the American Physical Society and SciPris.

Licensed Content Information

License Number: RNP/18/JUL/006206
License date: 18-Jul-2018
DOI: 10.1103/PhysRev.23.655
Title: A Method of Drawing Metallic Filaments and a Discussion of their Properties and Uses
Author: G. F. Taylor
Publication: Physical Review
Publisher: American Physical Society
Cost: USD \$ 0.00

Request Details

Does your reuse require significant modifications: No
Specify intended distribution locations: Malaysia
Reuse Category: Reuse in a thesis/dissertation
Requestor Type: Student
Items for Reuse: Figures/Tables
Number of Figure/Tables: 1
Figure/Tables Details: Figure 1
Format for Reuse: Electronic

Information about New Publication:

University/Publisher: University of Malaya
Title of dissertation/thesis: DESIGN AND FABRICATION OF COPPER-FILLED PHOTONIC CRYSTAL FIBER FOR PASSIVE OPTICAL DEVICES
Author(s): Mohd Fahmi Bin Azman
Expected completion date: Jan. 2019

License Requestor Information

Name: Mohd fahmi Azman
Affiliation: Individual
Email Id: fahmibinazman@gmail.com
Country: Malaysia

**SPRINGER NATURE**

Title: Production, properties and applications of microwire and related products
Author: I. W. Donald
Publication: Journal of Materials Science (full set)
Publisher: Springer Nature
Date: Jan 1, 1987

Copyright © 1987, Chapman and Hall Ltd.

Logged in as:
Mohd Fahmi Bin Azman
Universiti Malaya
Account #:
3001302774

[LOGOUT](#)

Order Completed

Thank you for your order.

This Agreement between Universiti Malaya -- Mohd Fahmi Bin Azman ("You") and Springer Nature ("Springer Nature") consists of your license details and the terms and conditions provided by Springer Nature and Copyright Clearance Center.

Your confirmation email will contain your order number for future reference.

[printable details](#)

License Number	4392280056661
License date	Jul 18, 2018
Licensed Content Publisher	Springer Nature
Licensed Content Publication	Journal of Materials Science (full set)
Licensed Content Title	Production, properties and applications of microwire and related products
Licensed Content Author	I. W. Donald
Licensed Content Date	Jan 1, 1987
Licensed Content Volume	22
Licensed Content Issue	8
Type of Use	Thesis/Dissertation
Requestor type	academic/university or research institute